UNIVERSIDADE FEDERAL DO CEARÁ
CENTRO DE CIÊNCIAS
DEPARTAMENTO DE FÍSICA
PROGRAMA DE PÓS-GRADUAÇÃO EM FÍSICA

GRUPO DE TEORIA DA MATÉRIA CONDENSADA

MARIA LÚCIA ALVARES PAZ

# ELECTROSTATICALLY CONFINED QUANTUM DOTS IN BILAYER PHOSPHORENE

FORTALEZA

2025

MARIA LÚCIA ALVARES PAZ

# ELECTROSTATICALLY CONFINED QUANTUM DOTS IN BILAYER PHOSPHORENE

Tese de Doutorado apresentada ao Programa de Pós-Graduação em Física da Universidade Federal do Ceará, como requisito parcial para a obtenção do Título de Doutor em Física. Área de Concentração: Física da Matéria Condensada.

Orientador: Prof. Dr. Gil de Aquino Farias.

Coorientador: Prof. Dr. Diego Rabelo da Costa.

FORTALEZA
2025

Dados Internacionais de Catalogação na Publicação
Universidade Federal do Ceará
Sistema de Bibliotecas
Gerada automaticamente pelo módulo Catalog, mediante os dados fornecidos pelo(a) autor(a)

---

P368e Paz, Maria Lucia Alvares.
Electrostatically Confined Quantum Dots in Bilayer Phosphorene / Maria Lucia Alvares Paz. – 2025.
84 f. : il. color.

Tese (doutorado) – Universidade Federal do Ceará, Centro de Ciências, Programa de Pós-Graduação em Física , Fortaleza, 2025.
Orientação: Prof. Dr. Gil de Aquino Farias.

1. Materiais bidimensionais. 2. Semicondutores anisotrópicos. 3. Propriedades eletrônicas. 4. Fosforeno. 5. Pontos quânticos. I. Título.
CDD 530

MARIA LÚCIA ALVARES PAZ

# ELECTROSTATICALLY CONFINED QUANTUM DOTS IN BILAYER PHOSPHORENE

Tese de Doutorado apresentada ao Programa de Pós-Graduação em Física da Universidade Federal do Ceará, como requisito parcial para a obtenção do Título de Doutor em Física. Área de Concentração: Física da Matéria Condensada.

Aprovada em 29/08/2025.

BANCA EXAMINADORA

Gil de Aquino Farias
Universidade Federal do Ceará (UFC)

Prof. Dr. Diego Rabelo da Costa
Universidade Federal do Ceará

Prof. Dr. João Milton Pereira Júnior
Universidade Federal do Ceará (UFC)

Prof. Dr. Teldo Anderson Da Silva Pereira
Universidade Federal do Mato Grosso (UFMT)

Prof. Dr. Mauricio Godoy
Universidade Federal do Mato Grosso (UFMT)

Aos meus pais, que, mesmo na simplicidade da vida, sempre sonharam grande comigo.

## Acknowledgments

First of all, I thank God for giving me strength and perseverance, even in the most challenging times.

I am deeply grateful to my advisor, Gil de Aquino, for welcoming me into the group and for his invaluable guidance throughout this journey. I also thank my co-advisor, Diego Rabelo, for his trust and support in developing this work. I am also grateful to all the teachers and mentors who have guided me so far.

I sincerely thank my parents Antônia and Matias, and my siblings, Matias, Luana, and Josilene, for believing in my goals and supporting my decisions unconditionally.

I am profoundly grateful to my partner, Daniel, for his love, companionship, and unwavering support throughout these years. This journey would have been incredibly difficult without you.

I also thank all my friends, especially Crislane and Renata, who at different stages held my hand and offered their support when I needed it the most.

Finally, I thank the Physics Department at UFC, together with the GTMC, for their academic guidance and support. This study was financed in part by the Coordenação de Aperfeiçoamento de Pessoal de Nível Superior - Brasil (CAPES) - Finance Code 001.

# RESUMO

Desde o isolamento do grafeno em poucas camadas em 2004 por Geim e Novoselov, materiais em suas versões lamelares têm recebido grande destaque na comunidade científica e tecnológica devido às propriedades eletrônicas, ópticas e de transporte peculiares que não estão presentes em suas versões *bulk*. Entre esses materiais bidimensionais, o *fósforo negro*, um alótropo do fósforo, apresenta alta mobilidade eletrônica e, ao contrário do grafeno, é um semicondutor cujo *gap* de energia depende fortemente do número de camadas. O amplo intervalo de frequências coberto pelo *gap* variável ($\sim$ 2.0 eV para monocamada até $\sim$ 0.3 eV no *bulk*), aliado a propriedades anisotrópicas em sua estrutura eletrônica, torna esse material promissor para diversas aplicações, especialmente em optoeletrônica. Neste trabalho, investigamos as propriedades eletrônicas de portadores de carga confinados em pontos quânticos definidos exclusivamente por meio de um potencial eletrostático dependente da posição, sem necessidade de recorte físico do material. Esse potencial quebra a simetria de inversão da bicamada de fosforeno, modulando localmente o *gap* e permitindo o confinamento dos portadores de carga. Utilizamos o método *tight-binding* para investigar numericamente os estados eletrônicos e suas funções de onda em potenciais de simetria circular, na ausência e presença de um campo magnético perpendicular. Como resultados principais, identificamos o fechamento do *gap* para um valor crítico do potencial, a consequente emergência de cones de Dirac e que o gap de energia dos pontos quânticos segue uma lei de potência com o raio, $E_g(R) \propto 1/R^{1.38}$, evidenciando o papel combinado do confinamento eletrostático e da anisotropia do material.

**Palavras-chave**: materiais bidimensionais; semicondutores anisotrópicos; propriedades eletrônicas; fosforeno; pontos quânticos.

# ABSTRACT

Since the isolation of few-layer graphene in 2004 by Geim and Novoselov, materials in their lamellar versions have received great attention from the scientific and technological community due to their peculiar electronic, optical, and transport properties that are not present in their bulk forms. Among these two-dimensional materials, black phosphorus, an allotrope of phosphorus, exhibits high electron mobility and, unlike graphene, is a semiconductor whose energy gap strongly depends on the number of layers. The wide frequency range covered by the tunable gap ($\sim 2.0$ eV for the monolayer down to $\sim 0.3$ eV in the bulk), combined with the anisotropic properties of its electronic structure, makes this material promising for various applications, especially in optoelectronics. In this work, we investigate the electronic properties of charge carriers confined in quantum dots defined exclusively through a position-dependent electrostatic potential, without the need for physical patterning of the material. This potential breaks the inversion symmetry of bilayer phosphorene, locally modulating the gap and allowing for charge carrier confinement. We employ the tight-binding method to numerically investigate the electronic states and their wave functions under circularly symmetric potentials, both in the absence and presence of a perpendicular magnetic field. As the main results, we identify the closing of the gap at a critical value of the applied potential, the consequent emergence of Dirac cones, and that the quantum dot energy gap follows a power-law dependence on the dot radius, $E_g(R) \propto 1/R^{1.38}$, highlighting the combined role of electrostatic confinement and material anisotropy.

**Keywords**: two-dimensional materials; anisotropic semiconductors; electronic properties; phosphorene; quantum dots.

# LIST OF FIGURES

# LIST OF TABLES

## TABLE OF CONTENTS

# 1 INTRODUCTION

In this thesis, we investigate the electronic properties of quantum dots electrostatically confined in bilayer phosphorene. Given the unique electronic and structural properties of phosphorene — in particular, its finite and layer-dependent bandgap as well as its strong in-plane anisotropy — it becomes possible to propose the confinement of charge carriers in a bilayer solely by means of an external gate potential, without the need for any lithographic patterning. These characteristics make phosphorene a particularly appealing platform for realizing such nanostructures, in contrast to graphene, which has a vanishing energy gap and lacks intrinsic anisotropy. The following sections discuss the key concepts and terminology necessary for the development of this work.

## 1.1 Beyond Graphene: a Zoo of New 2D Materials

Since its first isolation in 2004 by Geim and Novoselov [1], graphene has been a topic of intense research due to its peculiar and interesting properties, such as high electronic mobility at room temperature [2], high thermal conductivity [3], high flexibility that supports large deformations [4] and impermeability to gases [5] to quote a few. Therefore, this one-atom-thick two-dimensional (2D) allotrope of carbon has become a great topic of interest in technology and science, with potential applications in areas related to composites, energy, electronics, environment, and thin films [6]. The intensive research on graphene has not only sparked academic interest in exploring other low-dimensional atomic-layer materials, such as hexagonal boron nitride (h-BN) [7], the huge family of transitional-metal dichalcogenides (TMDs) [8] and phosphorene [9], but also highlighted their potential for future optoelectronic applications, owing to their unique physical and chemical properties.

h-BN consists of a 2D crystalline structure with alternating boron and nitrogen atoms, forming a honeycomb lattice closely matching the lattice space of graphene [10]. It is an excellent dielectric material, with a wide bandgap of approximately 6 $eV$. Owing to its high chemical stability and insulating properties, h-BN is commonly integrated into some heterostructures, where it serves as an effective dielectric spacer or substrate in field-effect devices.

Transition metal dichalcogenides (TMDs) are a family of layered materials with the general formula $MX_2$, where M is a transition metal from groups 4 to 10 of the periodic table, and X is a chalcogen atom, such as sulfur (S), selenium (Se), or tellurium (Te). Approximately 40 different 2D TMDs have either been studied experimentally or predicted to be stable through theoretical calculations [11], some of them are metallic (e.g., $VS_2$ and $NbS_2$) and others are semiconducting (e.g., the group with metallic atoms of molybdenum (Mo) and tungsten (W), as depicted in Figure 1(a) for $MoS_2$ and $WSe_2$) or insulating (e.g., $HfS_2$). TMDs exhibit a unique combination of atomic-scale thickness, favorable electronic and mechanical properties, and tunable bandgaps [12], which span a wide range depending on their chemical composition, as illustrated in Figure 1(c). The interplay of such desired properties makes 2D TMDs some of the promising materials for the development of future applications in nanoelectronics, nanophotonics, and sensing technologies [13]. In particular, monolayer TMDs, such as $MoS_2$, $MoSe_2$, $MoTe_2$, $WS_2$, and $WSe_2$, possess a direct bandgap and can be employed in electronics as field-effect transistors (FETs) and in optoelectronics as light emitters and photodetectors [14]. In addition, some TMD materials such as $ReS_2$ and $ReSe_2$ exhibit strongly anisotropic in-plane properties and a distorted lattice structure as shown in Figure 1(b).

Among the diverse range of two-dimensional materials, phosphorene has attracted significant attention due to its finite and tunable bandgap, high carrier mobility, and large on–off current ratios [15].

Figure 1 – Sketches of a typical (a) isotropic and (b) anisotropic X–M–X sandwich structure of TMDs. (c) A comparison of the optical bandgap for TMDs composed of different constituents and different numbers of layers. It is also shown on the right side of panel (c) the gap for other 2D materials: graphene (Gr), black phosphorus (BP), $SnS_2$, and h-BN.

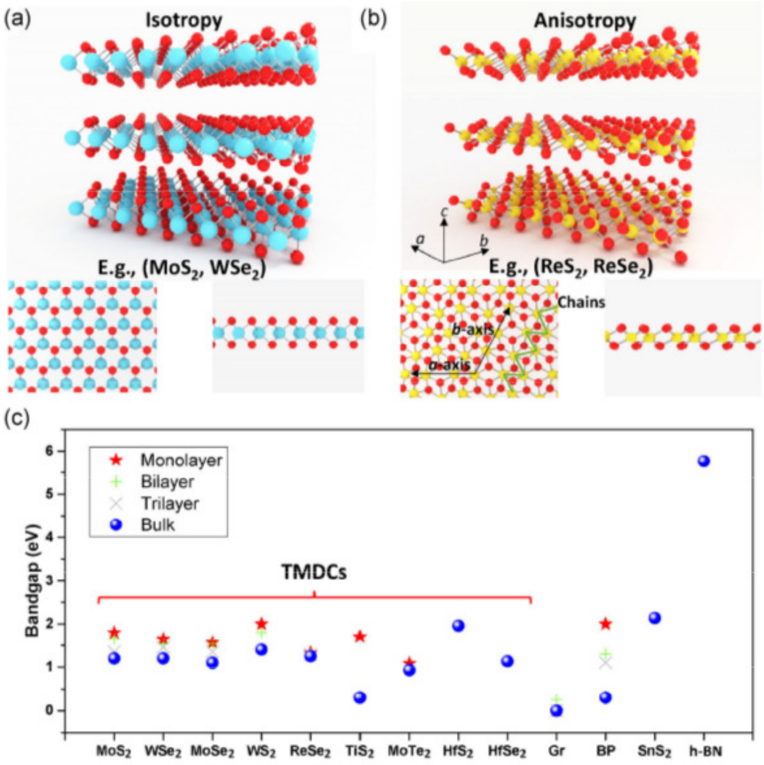

Source: TIAN, H. *et al.*, 2016 [16].

## 1.2 Phosphorene: An interesting anisotropic semiconductor

Black phosphorus (BP), the most stable allotrope among the phosphorus family, was first synthesized by Bridgman in 1914 [17]. Although known to science for decades, this material has regained enormous interest over the last few years due to its unique physical and electronic properties. Unlike TMDs, BP is composed of a single chemical element, phosphorus. Similar to graphite, its structure consists of stacked layers held together by Van der Waals forces [18], which allow mechanical exfoliation down to a monolayer of two-atom thickness, the so-called phosphorene. In addition to BP, several other phosphorus allotropes have been theoretically predicted, including the three $\beta$, $\gamma$, and $\delta$ forms, shown in Figures 2(a), 2(b), and 2(c), respectively, which displays distinct electronic properties. For instance, blue phosphorus features an in-plane hexagonal lattice with an AB layer stacking [19] and presents a larger bandgap compared to that of BP [20].

Figure 2 – Top and side views of the monolayer structures of (a) BP ($\alpha$-P), (b) blue phosphorus ($\beta$-P), (c) $\gamma$-phosphorus ($\gamma$-P), and (d) $\delta$-phosphorus ($\delta$-P). Different color tones indicate the atoms in two adjacent planes.

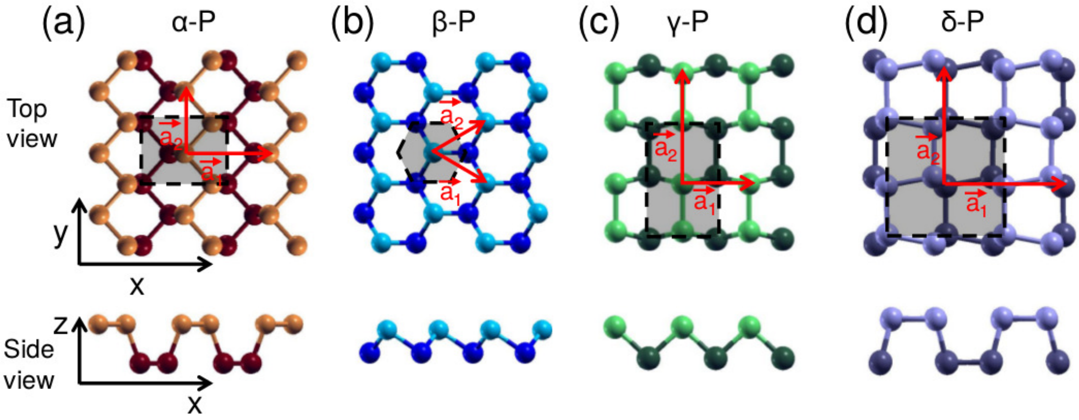

Source: GUAN, J. *et al.*, 2014 [21].

Figure 3 presents the puckered crystal structure of monolayer BP, in which each phosphorus atom forms covalent bonds with three neighboring atoms [18] through $sp^3$-like hybridization. In the top view, the lattice may visually resemble the honeycomb structure of graphene; however, the atomic arrangement in BP is orthorhombic and consists of two vertically offset sublayers, forming a puckered configuration. This structural anisotropy, together with the orbital hybridization, is a key factor underlying the direction-dependent (anisotropic) electronic and optical properties of phosphorene.

Figures 4(a) and 4(b) show experimental ADF-STEM (Annular Dark Field-Scanning Transmission Electron Microscopy) images of an exfoliated BP flake along the [001]

Figure 3 – Crystal structure of BP, emphasizing the lattice vectors $a_1$ and $a_2$, the unit cell (red dashed rectangle), and the two most investigated crystallographic directions: armchair and zigzag.

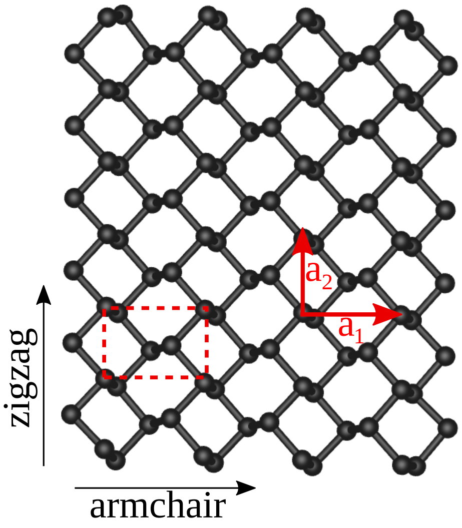

Source: Elaborada pelo Autor.

and [101] crystallographic directions, respectively, confirming that the theoretical model used to describe the atomic structure of phosphorene is accurate. These ADF-STEM images, captured along the [001] and [101] zone axes, allow the direct determination of the bulk BP lattice parameters, which have been measured to be $3.313\,\text{Å}$ for the interlayer distance and $4.374\,\text{Å}$ for the distance between two atomic sites A-D or B-C within the same layer but in different sublayers. Figures 4(c) and 4(d) show low- and high-magnification ADF-STEM images taken at the edge of the BP flake, which was aligned along the [100] crystallographic direction.

The 2D counterpart of BP possesses interesting and unique properties; for example, unlike graphene, it is a semiconductor with a direct bandgap. Many of its features exhibit anisotropic behavior due to its structural anisotropy, which is reflected in an anisotropic band structure, anisotropic Fermi velocities, and anisotropic effective masses [23]. The following subsections are devoted to a detailed discussion of the electronic and optical properties of phosphorene, as well as to briefly presenting the experimental techniques used to fabricate phosphorene.

### *1.2.1 Electronic properties*

As mentioned before, phosphorene is a semiconductor with a direct bandgap, which can also be tunable [24]. According to some studies, its bandgap shows a strong dependence on the number of layers, ranging from approximately $\sim 0.3$ eV in bulk BP to approximately $\sim 2$ eV in the single layer phosphorene [18], filling the interval not covered by graphene (0.0-0.2

Figure 4 – (a) ADF-STEM image of BP viewed along the [001] crystallographic direction, or equivalently, a top-down view, and compared to the modeled theoretical lattice structure. (b) ADF-STEM image viewed along the [101] direction, or equivalently, 17 degrees tilted off the [001] zone axis. (c) ADF-STEM image captured at an edge of the BP flake, showing multiple layers stacked together, or equivalently, along the [100] direction. (d) Magnified image of the region highlighted in (c).

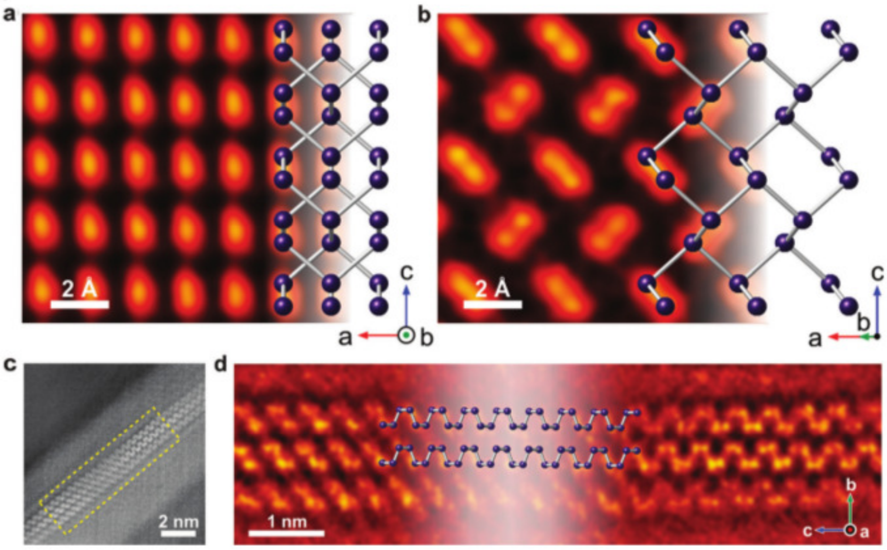

Source: WU, R. J. *et al.*, 2015 [22].

eV) and TMDs (1.0-2.0 eV) [25]. The systematic decrease in the energy gap as the number of layers increases is an expected behavior due to the interlayer coupling, which modifies the overlap of wave functions and reduces the separation between conduction and valence bands [26, 27].

In Figure 5, we can verify how the bandgap value of multilayer and doped BP samples spans a wide energy range not covered by any other 2D materials isolated to date. Several applications demand semiconductor materials with bandgap values in this energy range, such as thermal imaging, thermoelectric, telecom, and photovoltaic applications [24]. The bandgap of BP remains direct regardless of the number of layers, unlike $MoS_2$, for example, which shows a direct bandgap only in its monolayer form [28]. Besides being a narrow-gap semiconductor, phosphorene also displays a high carrier mobility of up to 1000 $cm^2$ $V^2$ $s^{-1}$ [29, 30].

Unlike other extensively studied 2D materials, such as graphene, silicene, and TMDs, the electronic band structure of phosphorene is highly anisotropic [24, 31, 27], meaning that the effective masses present different values in different directions. Figure 6(a) shows the electronic band structures for monolayer, bilayer, and trilayer BP obtained via *ab initio* calculations. Regardless of the number of layers, the bandgap is direct and located at the $\Gamma$ point of the Brillouin zone. Figure 6(b) synthesizes this thickness dependence of the calculated and

Figure 5 – Comparison of the bandgap values for different 2D semiconductor materials and for conventional semiconductors.

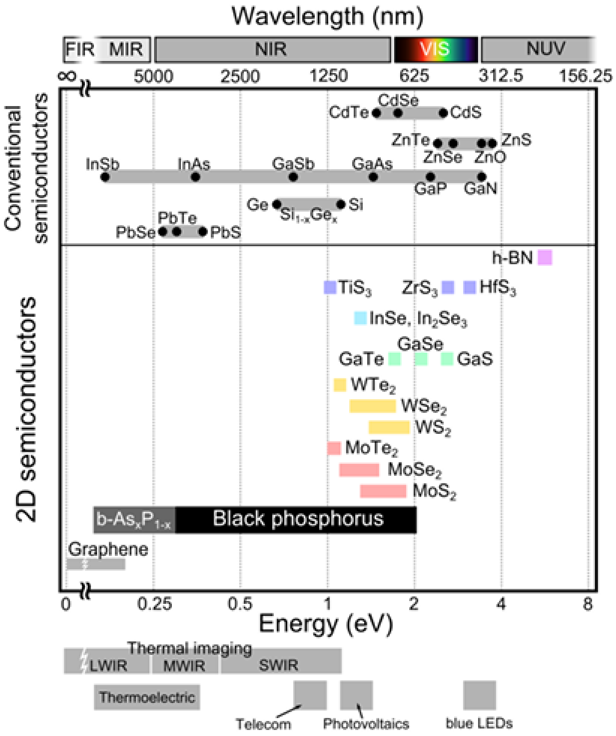

Source: Adapted from CASTELLANOS-GOMEZ, A. *et al.*, 2015 [24].

measured bandgap.

Figure 6 – (a) Calculated band structure of monolayer, bilayer, and trilayer of BP. (b) Thickness dependence of the BP bandgap calculated with different approaches.

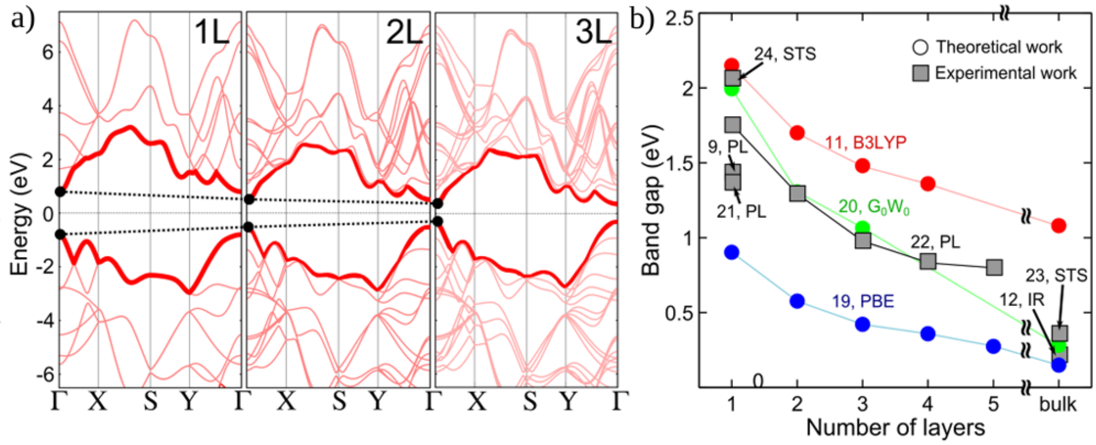

Source: Adapted from CASTELLANOS-GOMEZ, A. *et al.*, 2015 [24].

### *1.2.2 Optical properties*

Similarly to the electronic band structure of phosphorene, its optical response has a strong dependence on the number of layers [32, 33] and shows an anisotropic profile originating from its puckered structure. That is, in the zigzag direction, it is transparent to polarized light, while in the armchair direction, it absorbs polarized light [33, 26].

Figure 7 – (a) Polar representation of the absorption coefficient $A(\alpha)$ for a 40-nm intrinsic BP film for normal incident light with excitation energies at the bandgap, and larger. $A(\alpha)$ is plotted for two values of interband coupling strengths. (b) Polar representation of the experimental extinction spectra $Z$ obtained from Fourier-transform infrared spectroscopy, for a $\sim$40-nm BP film on a $SiO_2$ substrate.

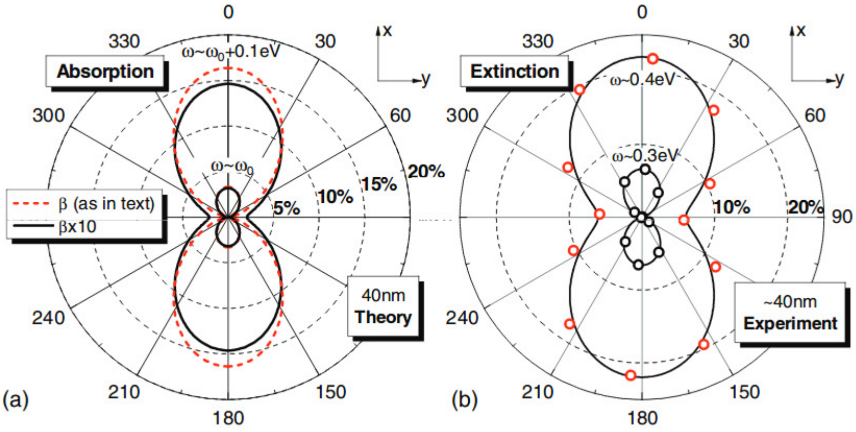

Source: LOW, T. *et al.*, 2014 [34].

Figure 7(a) exhibits the strong dependence of the absorption coefficient, $A(\alpha)$, on the polarization angle $\alpha$ for a 40-nm BP film. In Figure 7(b), the extinction factor, $Z = 1 - T/T_0$ is presented, which describes the transmission through samples with $(T)$ and without $(T_0)$ BP.

In comparison with some other 2D materials, such as graphene and $MoS_2$, phosphorene has a great advantage regarding balanced photo-response and response time. While graphene exhibits a weak photo response with lower response time, $MoS_2$ presents a strong photo-response but a higher response time [24]. Hence, the optical properties, as well as other features of this material, fill the gap between graphene and many other 2D materials, such as TMDs.

As shown in Figure 8, phosphorene displays remarkable photoluminescence, which has also been observed to be layer-dependent. When comparing bilayer and five-layer phosphorene, it has been shown that in the former the photoluminescence phenomenon is approximately an order of magnitude higher than in the latter, highlighting its pronounced layer-dependent optical properties [35].

Figure 8 – (a) Atomic Force microscopy (AFM) image of 2-layer (2L) phosphorene. (b) Photoluminescence spectra of 2L, 3L, 4L, and 5L.

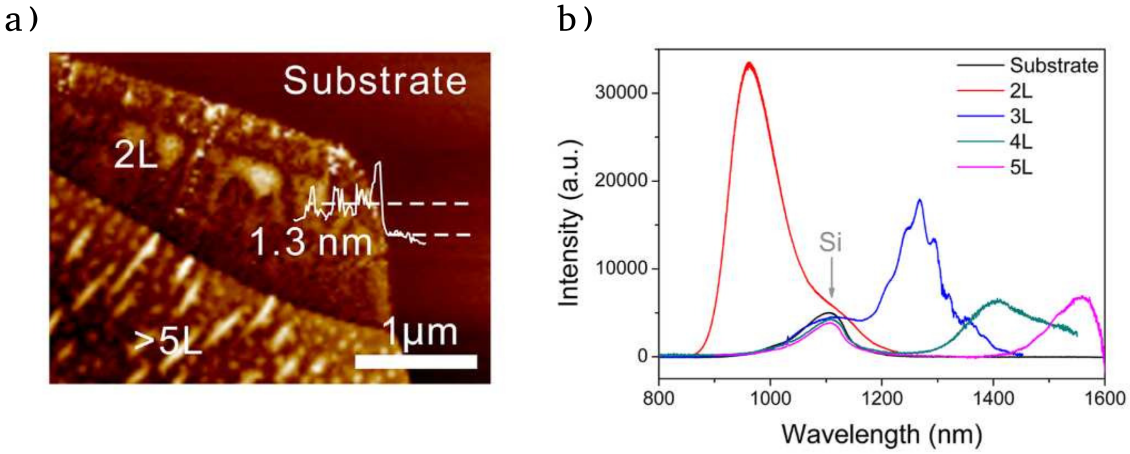

Source: Adapted from ZHANG, S. *et al.*, 2014 [35].

### *1.2.3 Fabrication techniques*

In order to convert the outstanding physical and chemical properties of phosphorene into actual device applications, efficient production methods for uniform, layered, and thin phosphorene are needed. Despite having unique structure-dependent properties, the stability of phosphorene has been one of the biggest issues for its development and applications [36]. Therefore, current research has investigated the interactions between this material and environmental entities such as water and air. Some strategies that have been employed to enhance the stability of this material and enable its long-term use include, for instance, the encapsulation of phosphorene between two layers of different 2D materials, such as graphene and h-BN [37], the formation of protective layers over phosphorene [38], and organic liquid exfoliation tecniques. The routes to synthesize few-layer BP present similarities to those used to isolate graphene from graphite, as both bulk BP and graphite consist of stacked layers coupled together by Van der Waals forces. In this section, current methods for phosphorene synthesis are examined from two perspectives: top-down and bottom-up approaches, with a discussion of their features and applicability.

**Top-down methods**:

In the top-down scenario, one starts from a large bulk sample in order to obtain a smaller one. The advantage of using top-down methods is the high level of control over the location and placement of the produced material. However, there is no control over the edges of the systems, and the layers can also be damaged during the entire process. In this context, we next briefly discuss some of the most commonly used top-down methods, *mechanical exfoliation,* *plasma-assisted mechanical exfoliation, and liquid-phase exfoliation*, as routes to synthesize phosphorene, highlighting their merits and limitations for this purpose.

*Mechanical exfoliation* is a technique performed by successive cleaving of the bulk system. One of the most popular exfoliation techniques uses Scotch tape in the isolation of monolayers (Figure 9). In 2004, Geim and Novoselov isolated graphene in its few-layer form from graphite using this method [1, 39]. Since in BP, as well as in graphite, the layers interact via van der Waals forces, mechanical exfoliation can also be used to produce BP in its few-layer or single-layer form. Even though it has been widely employed to obtain few-layer and flakes from bulk systems, which is suitable for the production of individual devices on a laboratory scale, this strategy is not scalable yet [25]. Usually, the exfoliation process must be followed by additional steps to remove adhesive impurities on the substrate surface, where the monolayers are transferred after being peeled off. Studies regarding reproducibility, cleaning, characterization steps, and large-scale production have been carried out [40].

Figure 9 – Cleaving the bulk graphite using the Scotch tape.

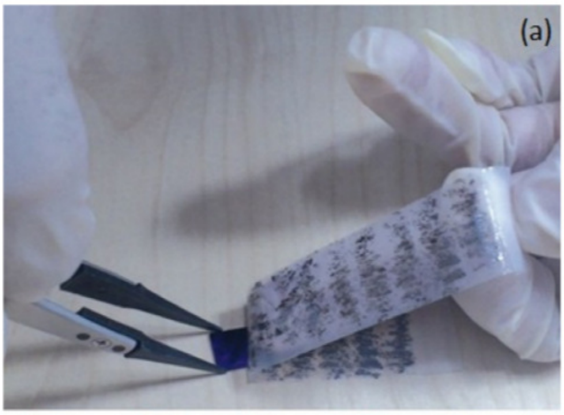

Source: Adapted from NOORDEN, R. V., 2012 [41].

*Liquid phase exfoliation* is another method employed to obtain phosphorene from large samples of BP, and it has been reported as a promising technique [42, 43]. In this process, a sample of BP is placed into distinct solvents to enable the intercalation of ionic species into the bulk, thereby increasing the distance between the layers and making possible the exfoliation of the material in liquid. The quality of the structures produced using liquid-phase exfoliation has been reported to be comparable to that obtained by mechanical exfoliation [44]. A remaining challenge in this method is, for instance, the chemical reaction between the exfoliated layers and water and/or oxygen, which can be mitigated by selecting an efficient and non-toxic solvent for phosphorene processing. Other 2D materials, such as graphene, h-BN, and TMDs synthesized by this procedure, have exhibited a satisfactory performance in electronic devices [43]. Figure 10 shows an example of samples obtained by this technique.

Figure 10 – Basic characterization from the bulk BP to the exfoliated phosphorene by Liquid phase exfoliation technique in N-cyclohexyl-2-pyrrolidone (CHP). (a) Structure of BP representing a layered analogy. (b) Scanning electron microscopy (SEM) image of a layered BP crystal (scale bar, 100 mm). (c) Photograph of a dispersion of exfoliated few-layer BP in CHP; (d-f) Representative low-resolution transmission electron microscopy (TEM) images of exfoliated FL-BP in CHP (scale bars in d–f: 500 nm, 100 nm, and 500 nm).

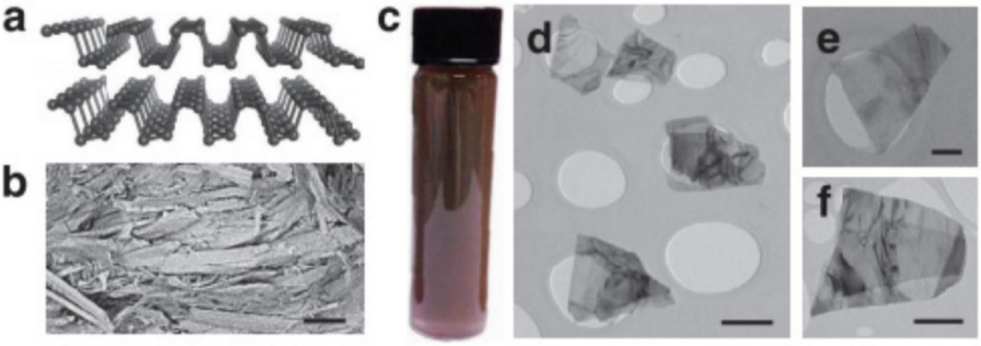

Source: HANLON, D. *et al.*, 2015 [45].

*Plasma-assisted mechanical exfoliation* has also been applied to isolate single-layer BP as well. Typically, this method consists of mechanical cleavage on a substrate followed by a plasma thinning process to reduce the thickness of the sample. Since this technique enables control over the thickness of the BP sample, it opens the way for the fabrication of more precise devices [25]. Figure 11 shows the optical image of multilayer phosphorene (11(a)) and the same after a thinning process with $Ar^{+}$((11(b)). As one can notice, after the plasma treatment, the thickness of the pristine sample was significantly reduced.

Figure 11 – (a) Optical image of multilayer pristine phosphorene. (b) Similar image after $Ar^{+}$ thinning, where nL stands for the number of layers ($n$ = integer). Scale bars in (a) and (b) are 5 mm.

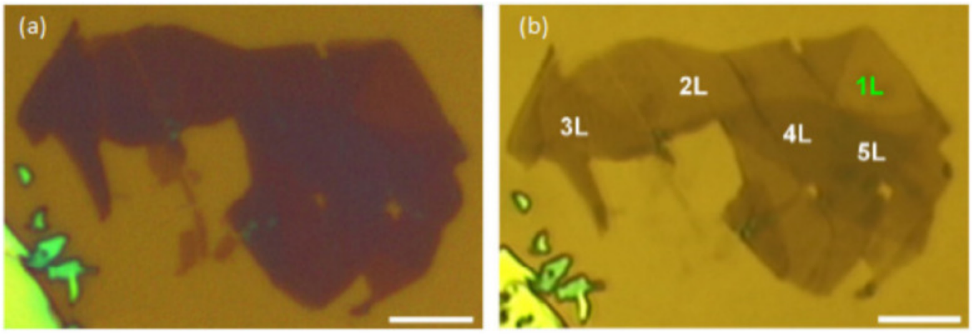

Source: Adapted from WU, L. *et al.*, 2014 [46].

**Bottom-up methods**:

On the other hand, regarding bottom-up approaches, the basic idea is to initiate the process from fundamental building blocks, such as atoms and molecules, in order to obtain larger systems. From this perspective, it is possible to achieve resolution control, thus providing very high precision at the atomic level [47]. The chemical vapor deposition (CVD) approach is the most typical bottom-up preparation technique and is widely used in the synthesis of various 2D materials [48, 49]. Regarding the deposition of 2D phosphorene films on a specific surface, three main steps are generally considered: (i) nucleation of the smallest unit, (ii) expansion of the smallest unit to larger deposition sites, and (iii) subsequent formation of the phosphorene layer on the surface [40].

To synthesize phosphorene, several types of CVD processes have been employed [50]. One way to obtain BP in this scenario, for example, is to take the red phosphorus as the precursor, as shown in Ref. [51], where it is reported the use of chemical-vapor-transport process (variant of CVD) for converting red phosphorus into BP. Furthermore, different CVD protocols have been used to deposit BP obtained from red phosphorus onto specific substrates, as reported in Refs. [52, 53].

The choice of substrate plays a crucial role in the bottom-up growth of 2D phosphorene. Gao et al., for example, reported that weak interactions between the substrate and the phosphorus sheet led to an unstable 2D layer, while strong interactions caused the rupture of the phosphorus sheet [54]. Therefore, the intermediate interaction strength is considered optimal for the 2D growth of this material. In summary, direct bottom-up chemical synthesis techniques show broad application potential in the preparation of controllable, large-scale, and high-quality phosphorene. However, further investigation is still required to optimize preparation conditions, scalability, and cost-effectiveness [55].

Although both top-down and bottom-up approaches have been widely investigated and improved to obtain clean and large BP samples, the former has gained greater popularity, as it has been shown to offer simpler synthesis processes compared to the latter [40].

After discussing some of the electronic and optical properties of multilayer BP in the context of 2D materials, comparing its features with those of other 2D systems, we now turn to fundamental concepts of solid-state physics that underpin the theoretical approaches adopted in the work developed.

## 1.3 Band theory of crystals

The electronic band structure, which refers to the arrangement of energy levels in a material, is one of its most fundamental characteristics, as it determines many of the material's electronic properties. There are several theoretical models used to calculate the band structure of a system. Some of them are *ab initio* methods, such as Density Functional Theory (DFT), while others are approximate approaches with lower accuracy at low energies compared to DFT, such as the tight-binding method. The suitability of each approach largely depends on the specific system under investigation. Before discussing two of these models (Subsecs. 1.3.2 and 1.3.3), it is necessary first to describe how these bands are formed.

### *1.3.1 Basic aspects*

To discuss and understand the formation of energy bands, let us consider the following reasoning. An isolated electron occupies stationary quantum states characterized by discrete energy levels, corresponding to atomic orbitals such as 1s, 2s, 2p, 3s, 3p, and so on. In the case of an atom with many electrons, the ground state is obtained by distributing the electrons among the lowest available energy levels, following the Pauli exclusion principle.

In a crystal, which consists of a large number of atoms, we must consider how the electronic states are modified when atoms are brought close together. When two atoms are near each other, their individual energy levels experience a slight perturbation due to the mutual interaction, causing the levels to split. When many atoms are arranged periodically, as in a crystal, the number of such perturbed levels becomes very large; these closely spaced levels form what is known as an energy band, which appears nearly continuous. For instance, when two atoms are far apart, their energy levels are degenerate (identical in energy). As they are brought closer together, this degeneracy is lifted, and each level splits into two. Extending this to many atoms, the splitting leads to the formation of a full energy band.

Figure 12 – Schematic representation of the evolution from discrete atomic energy levels to energy bands as the distance between $N$ identical atoms decreases. For large separations, each orbital forms a degenerate level with $N$ atoms, such as $2N$ states for $s$ orbitals and $6N$ states for $p$ orbitals. As atoms come closer, the degeneracy is lifted due to the overlap of atomic orbitals, resulting in energy bands.

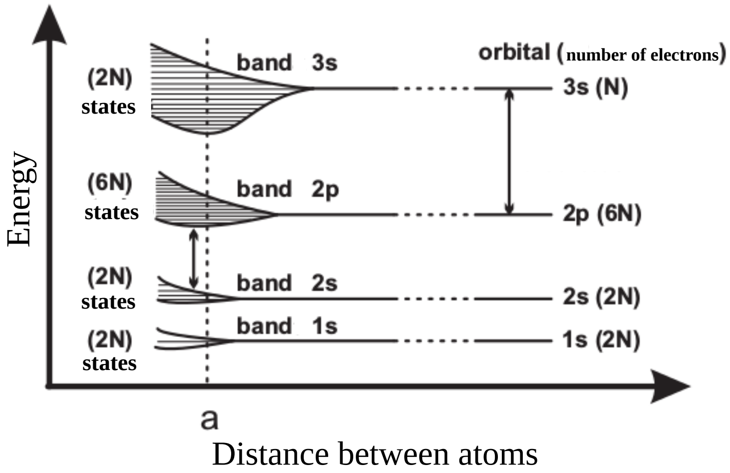

Source: Adapted from REZENDE, S. M., 2004, p. 93 [56].

The phenomenon occurs due to the superposition of the eigenfunctions of each atom. Similarly, when $N$ atoms of the same kind are far apart, each atomic energy level gives rise to a level in the $N$-fold degenerate system. As the distance between the atoms decreases, this degeneracy is lifted, and each original level splits into $N$ closely spaced levels. Figure 12 illustrates this process, showing how degeneracy depends on the interatomic spacing for a system of $N$ atoms.

### *1.3.2 Tight-binding model*

One of the most widely adopted approaches for calculating the electronic band structure of nanostructured systems is the tight-binding method. Originally proposed by Bloch, this method is based on the Linear Combination of Atomic Orbitals (LCAO) over the atoms in the crystal. It is particularly suitable when the overlap between atomic wave functions is small yet significant enough to require corrections to the picture of isolated atoms [57]. In this formulation, the Hamiltonian and overlap matrix elements can be assumed without explicitly specifying the orbitals, except for their symmetry properties. The values of these matrix elements may be approximately estimated, fitted to experimental data, or extracted from first-principles calculations [58]. Thus, the tight-binding model enables the description of the electronic structure and total energy of a system throughout the entire Brillouin zone at a low computational cost, often providing both qualitative and quantitative accuracy for practical cases.

In the context of bilayer phosphorene, the tight-binding method is particularly advantageous because it naturally incorporates the material's highly anisotropic electronic structure and its layer-dependent bandgap, both of which are crucial to accurately describe the confined states in electrostatically defined quantum dots. Alternative approaches, such as the effective mass approximation, may fail to capture the strong directionality of the hopping parameters and the resulting anisotropy in the band dispersion. Therefore, the tight-binding model provides a reliable and computationally efficient framework for investigating the electronic properties of the systems studied in this thesis.

To develop the tight-binding approximation, one can assume that

$$H_{\text{at}}\psi_n = E_n\psi_n, \tag{1.1}$$

where $H_{\text{at}}$ represents the full periodic crystal Hamiltonian, which, in this context, can be approximated as the Hamiltonian of a single atom at a lattice point. The unit cell exhibits translational symmetry along the lattice vector $\vec{a}_i$ of the crystal. Therefore, any wave function of the lattice satisfies the Bloch theorem:

$$T_{\vec{a}_i}\Psi = e^{i\vec{k}\cdot\vec{a}_i}\Psi, \tag{1.2}$$

where $T_{\vec{a}_i}$ is the translational operation along $\vec{a}_i$, and $\vec{k}$ is the wave vector. The wave function can be expressed in various ways, but the most common approach is to represent $\Psi$ as a linear combination of atomic orbitals. Thus, we define the wave function $\Phi_j(\vec{k},\vec{r})$ as the sum over the atomic wave function $\varphi(\vec{r}-\vec{R}_j)$ at the $j$-th site, where $\vec{R}_j$ is the position of the atom:

$$\Phi_j(\vec{k},\vec{r}) = \frac{1}{\sqrt{N}}\sum_{\vec{R}_j} e^{i\vec{k}\cdot\vec{R}_j}\varphi(\vec{r}-\vec{R}_j), \quad j = 1,\ldots,N, \tag{1.3}$$

where $\varphi_j$ represents the atomic wave function in state $j$, and $N$ is the number of wave functions. The advantages of using atomic orbitals include the small number of basis functions, $n$, compared to the number of plane waves, as well as the ease of adapting the formulation to various physical properties [59]. Equation (1.3) satisfies the Bloch condition:

$$\begin{aligned}\Phi_j(\vec{k},\vec{r}+\vec{a}) &= \frac{1}{\sqrt{N}}\sum_{\vec{R}_j} e^{i\vec{k}\cdot\vec{R}_j}\varphi(\vec{r}+\vec{a}-\vec{R}_j),\\ &= e^{i\vec{k}\cdot\vec{a}}\frac{1}{\sqrt{N}}\sum_{\vec{R}_j-\vec{a}} e^{i\vec{k}\cdot(\vec{R}_j-\vec{a})}\varphi[\vec{r}-(\vec{R}_j-\vec{a})],\\ &= e^{i\vec{k}\cdot\vec{a}}\Phi_j(\vec{k},\vec{r}).\end{aligned} \tag{1.4}$$

In the solid, the eigenfunctions $\Psi_j(\vec{k},\vec{r})$ are defined as a linear combination of the Bloch functions:

$$\Psi_j(\vec{k},\vec{r}) = \sum_{j'=1}^{N} C_{jj'}(\vec{k})\Phi_{j'}(\vec{k},\vec{r}), \tag{1.5}$$

where $C_{jj'}$ are coefficients to be determined. The summation in Eq. (1.5) is over the Bloch orbitals $\Phi_{j'}(\vec{k},\vec{r})$, ensuring that $\Psi_j(\vec{k},\vec{r})$ satisfies the Bloch theorem. In this context, the $j$-th eigenvalue can be written as:

$$E_j(\vec{k}) = \frac{\langle\Psi_j|H|\Psi_j\rangle}{\langle\Psi_j|\Psi_j\rangle} = \frac{\int \Psi_j^* H \Psi_j \, d\vec{r}}{\int \Psi_j^* \Psi_j \, d\vec{r}}, \tag{1.6}$$

where $H$ is the Hamiltonian of the system. Substituting Eq. (1.5) into Eq. (1.6) yields:

$$E_i(\vec{k}) = \frac{\sum_{j,j'=1}^{N} C_{ij}^* C_{ij'}\langle\Phi_j|H|\Phi_{j'}\rangle}{\sum_{j,j'=1}^{N} C_{ij}^* C_{ij'}\langle\Phi_j|\Phi_{j'}\rangle} \equiv \frac{\sum_{j,j'=1}^{N} H_{jj'}(\vec{k}) C_{ij}^* C_{ij'}}{\sum_{j,j'=1}^{N} S_{jj'}(\vec{k}) C_{ij}^* C_{ij'}}, \tag{1.7}$$

where the Hamiltonian matrix elements $H_{jj'}(\vec{k}) = \langle\Phi_j|H|\Phi_{j'}\rangle$ represent the interaction energies between electrons localized at different sites. Substituting the Bloch functions from

Eq. (1.3) into the Hamiltonian matrix elements gives:

$$\begin{aligned}\langle\Phi_j|\mathcal{H}|\Phi_{j'}\rangle &= \left\langle \frac{1}{\sqrt{N}}\sum_{\vec{R}} e^{-i\vec{k}\cdot\vec{R}}\varphi_j(\vec{r}-\vec{R})\middle|\mathcal{H}\middle|\frac{1}{\sqrt{N}}\sum_{\vec{R}'} e^{i\vec{k}\cdot\vec{R}'}\varphi_{j'}(\vec{r}-\vec{R}')\right\rangle,\\ &= \frac{1}{N}\sum_{\vec{R},\vec{R}'} e^{i\vec{k}\cdot(\vec{R}'-\vec{R})}\langle\varphi_j(\vec{r}-\vec{R})|\mathcal{H}|\varphi_{j'}(\vec{r}-\vec{R}')\rangle,\\ &= \frac{1}{N}\sum_{\vec{R},\vec{R}'} e^{i\vec{k}\cdot(\vec{R}'-\vec{R})}t_{jj'}^{\vec{R}\vec{R}'},\end{aligned}\tag{1.8}$$

where we define

$$t_{jj'}^{\vec{R}\vec{R}'} \equiv \langle\varphi_j(\vec{r}-\vec{R})|\mathcal{H}|\varphi_{j'}(\vec{r}-\vec{R}')\rangle,\tag{1.9}$$

as the transfer integral or hopping parameter, typically obtained by parametrizing first-principles results for each crystal. These parameters represent the interaction energies between electrons localized at different lattice sites. They can be associated with the energy required to annihilate an electron at site $\vec{R}'$ and create it at site $\vec{R}$, or vice versa, depending on the distance between these sites. Note that hopping parameters can be positive or negative, depending on the crystal structure and the number of atoms and orbitals considered in the tight-binding approximation, and they do not represent actual probabilities.

On the other hand, the overlap matrix elements $S_{jj'}(\vec{k}) = \langle\Phi_j|\Phi_{j'}\rangle$ represent the overlap between the atomic orbitals considered in the approximation $\Phi_j(\vec{k},\vec{r})$. In general, the overlap matrix is the identity matrix when one assumes zero overlap between orbitals localized at different lattice sites. Substituting the Bloch functions from Eq. (1.3) into the overlap matrix elements yields:

$$\begin{aligned}\langle\Phi_j|\Phi_{j'}\rangle &= \left\langle \frac{1}{\sqrt{N}}\sum_{\vec{R}} e^{i\vec{k}\cdot\vec{R}}\varphi_j(\vec{r}-\vec{R})\middle|\frac{1}{\sqrt{N}}\sum_{\vec{R}'} e^{i\vec{k}\cdot\vec{R}'}\varphi_{j'}(\vec{r}-\vec{R}')\right\rangle,\\ &= \frac{1}{N}\sum_{\vec{R},\vec{R}'} e^{i\vec{k}\cdot(\vec{R}-\vec{R}')}\langle\varphi_j(\vec{r}-\vec{R})|\varphi_{j'}(\vec{r}-\vec{R}')\rangle,\\ &= \frac{1}{N}\sum_{\vec{R},\vec{R}'} e^{i\vec{k}\cdot(\vec{R}-\vec{R}')}s_{jj'}^{\vec{R}\vec{R}'},\end{aligned}\tag{1.10}$$

where we define

$$s_{jj'}^{\vec{R}\vec{R}'} \equiv \langle\varphi_j(\vec{r}-\vec{R})|\varphi_{j'}(\vec{r}-\vec{R}')\rangle,\tag{1.11}$$

as the overlap integral or overlap parameter, representing the superposition of the atomic orbitals corresponding to the sites located at $\vec{R}$ and $\vec{R}'$.

Electrons seek states of minimum energy, so the coefficients $C_{jj'}$ are optimized to minimize $E_i(\vec{k})$. This leads to the condition:

$$\frac{\partial E_i(\vec{k})}{\partial C^*_{ij}} = \frac{\sum_{j'=1}^{N} H_{jj'}(\vec{k}) C_{ij'}}{\sum_{j,j'=1}^{N} S_{jj'}(\vec{k}) C^*_{ij} C_{ij'}} - \frac{\sum_{j,j'=1}^{N} H_{jj'}(\vec{k}) C^*_{ij} C_{ij'}}{\left(\sum_{j,j'=1}^{N} S_{jj'}(\vec{k}) C^*_{ij} C_{ij'}\right)^2} \sum_{j'=1}^{N} S_{jj'}(\vec{k}) C_{ij'} = 0. \quad (1.12)$$

Multiplying both sides by $\sum_{j,j'=1}^{N} S_{jj'}(\vec{k}) C^*_{ij} C_{ij'}$ and substituting into Eq. (1.7) yields:

$$\sum_{j'=1}^{N} H_{jj'}(\vec{k}) C_{ij'} = E_i(\vec{k}) \sum_{j'=1}^{N} S_{jj'}(\vec{k}) C_{ij'}. \quad (1.13)$$

Defining a column vector

$$C_i = \begin{bmatrix} C_{i1} \\ C_{i2} \\ \vdots \\ C_{iN} \end{bmatrix}, \quad (1.14)$$

Eq. (1.13) can be expressed as:

$$HC_i = E_i(\vec{k}) S C_i. \quad (1.15)$$

A non-trivial solution is obtained when

$$\det[H - E_i(\vec{k}) S] = 0, \quad (1.16)$$

known as the secular equation, which provides all $n$ eigenvalues $E_i(\vec{k})$ for a given $\vec{k}$. When the overlap of the orbitals is neglected, the overlap integral is identified with the identity matrix, simplifying Eq. (1.16) to the conventional eigenvalue equation:

$$\det[H - E_i(\vec{k}) I] = 0. \quad (1.17)$$

#### 1.3.2.1 Tight-Binding Hamiltonian in Second Quantization

While the tight-binding method is traditionally developed within the framework of first quantization, its reformulation in *second quantization* is essential for describing systems with variable particle numbers and for incorporating many-body effects such as electron-electron interactions. This formalism uses *creation* ($\hat{c}^\dagger$) and *annihilation* ($\hat{c}$) operators acting on Fock space (the Hilbert space of variable particle number), providing a more natural and flexible language for quantum systems involving indistinguishable particles.

Before applying the tight-binding approximation, the general many-body Hamiltonian in first quantization can be written as

$$H = \sum_{k=1}^{N} T(\hat{x}_k) + \frac{1}{2} \sum_{k \neq l = 1}^{N} V(\hat{x}_k, \hat{x}_l), \quad (1.18)$$

where $T(\hat{x}_k)$ denotes the kinetic energy of the $k$-th particle, and $V(\hat{x}_k, \hat{x}_l)$ represents the pairwise interaction potential. Here, $\hat{x}_k$ denotes the coordinates of the $k$-th particle. The transition to second quantization involves rewriting this Hamiltonian using field operators defined over a chosen single-particle basis.

The corresponding Hamiltonian in second quantization reads

$$\hat{H} = \sum_{i,j} \hat{c}_i^\dagger [T]_{ij} \hat{c}_j + \frac{1}{2} \sum_{i,j,k,l} \hat{c}_i^\dagger \hat{c}_j^\dagger [V]_{ijkl} \hat{c}_k \hat{c}_l, \tag{1.19}$$

where $[T]_{ij}$ and $[V]_{ijkl}$ are the matrix elements of the kinetic and interaction terms, respectively, in a given single-particle basis. The operators $\hat{c}_i^\dagger$ and $\hat{c}_j$ create and annihilate electrons in states $i$ and $j$, and they satisfy fermionic anti-commutation relations.

In general, for any one-body operator $\hat{J}$ written in first quantization as

$$\hat{J} = \sum_{k=1}^{N} J(\hat{x}_k), \tag{1.20}$$

its second-quantized counterpart reads

$$\hat{J} = \sum_{r,s} \langle r | \hat{J} | s \rangle \hat{c}_r^\dagger \hat{c}_s, \tag{1.21}$$

where $\langle r | \hat{J} | s \rangle$ are the matrix elements of $\hat{J}$ in a chosen single-particle basis $\{|r\rangle\}$.

Applying this framework to the tight-binding Hamiltonian, we recall from Section 1.3.2 that the energy contributions originate from *hopping interactions* between localized atomic orbitals on different sites. The Hamiltonian, originally formulated using transfer integrals $t_{Rj,R'j'}$ in first quantization, is recast in second quantization as

$$\hat{H} = \sum_{R,R'} \sum_{j,j'} t_{Rj,R'j'} \hat{c}_{Rj}^\dagger \hat{c}_{R'j'}, \tag{1.22}$$

where $\hat{c}_{Rj}^\dagger$ creates an electron in orbital $j$ at site $R$, and $t_{Rj,R'j'}$ encodes the amplitude for hopping between orbital $j'$ at site $R'$ and orbital $j$ at site $R$. These matrix elements are obtained from first-principles calculations or empirical fitting and reflect the underlying crystal geometry and orbital overlaps.

This operator form of the tight-binding Hamiltonian captures the essence of electron mobility through a discrete lattice. It forms the foundation for analyzing band structures, electron transport, and interactions within many-body models such as the Hubbard model and beyond.

### *1.3.3 Effective mass approximation*

To understand the behavior of electrons in metals or semiconductors, it is important to study how the charge carriers respond to an applied electric field [56]. Initially, we can model the electron as a wave packet propagating through space with the group velocity given by

$$v_g = \frac{\partial \omega}{\partial k}. \tag{1.23}$$

Since $E = \hbar\omega$ is the electron energy, we have

$$\frac{\partial E}{\partial k} = \hbar v_g. \tag{1.24}$$

When an electric field exerts a force $F$ on an electron, the corresponding change in energy over a displacement $dx$ is given by

$$dE = F dx, \tag{1.25}$$

which, by using Eq. (1.24), can be expressed as

$$F dx = \hbar v_g dk. \tag{1.26}$$

It is well known that $dx = v_g dt$, thus

$$F = \hbar \frac{dk}{dt}, \tag{1.27}$$

which corresponds to the expected form of Newton's second law. From this result, we observe that the lattice potential does not alter the rate of change of momentum; however, it modifies the relationship between energy and momentum, effectively *changing* the electron's effective mass. To express the electron mass under these considerations, the electron acceleration as a function of $E$ and $k$ can be derived from Eq. (1.24) as follows

$$a = \frac{dv_g}{dt} = \hbar^{-1}\frac{\partial^2 E}{\partial k \partial t} = \hbar^{-1}\frac{\partial^2 E}{\partial k^2}\frac{dk}{dt}. \tag{1.28}$$

Replacing $dk/dt$ into Eq. (1.27), it leads to

$$F = \frac{\hbar^2}{\partial^2 E/\partial k^2} a. \tag{1.29}$$

Therefore, under the action of an external force, the electron in a crystal behaves as a free electron, but with an *effective mass* given by

$$m^* = \frac{\hbar^2}{\partial^2 E/\partial k^2}. \tag{1.30}$$

A more general expression for the effective mass must take into account the direction of the wave vector $\vec{k}$. Thus, in this context, the effective mass $m^*$ is a tensor quantity rather than a scalar, given by

$$m^*_{\alpha\beta} = \frac{\hbar^2}{\partial^2/\partial k_\alpha \partial k_\beta}, \tag{1.31}$$

where the indices $\alpha$ and $\beta$ denote the Cartesian components of the tensor. This tensorial effective mass is applicable to both electrons and holes in metals and semiconductors.

## 1.4 Low-dimensional nanostructures

Nanostructured materials have attracted considerable attention because they bridge the gap between bulk materials and molecular systems, leading to entirely new opportunities for applications, particularly in electronics, optoelectronics, and biology. When a crystal exhibits significant variation in its optical and electronic properties as a function of particle size, it is classified as a nanostructure [60]. Chemical and physical properties are strongly modified when the size of the system is reduced to the nanoscale (1–100 nm) in at least one dimension, as illustrated in Figure 13. These changes arise from quantum confinement effects caused by the dimensional reduction.

Generally, quantization effects in nanostructures can be categorized into three groups depending on whether the charge carriers are confined in one, two, or three dimensions. Confinement in one dimension creates two-dimensional (2D) structures known as quantum wells or quantum films. Carrier confinement in two dimensions results in one-dimensional (1D) quantum wires, while confinement in three dimensions produces quantum dots (QDs) [1] or quantum boxes, where electrons are strongly localized. These structures are considered zero-dimensional (0D) [61].

Figure 13 – Dimensions of materials exhibiting nanometer-scale size.

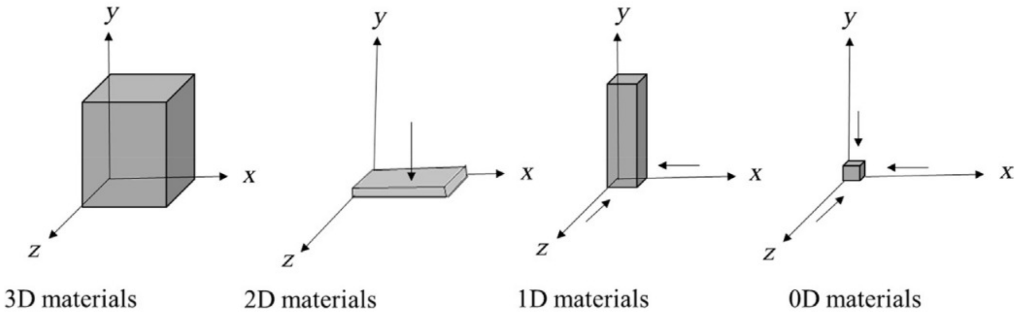

Source: KEBEDE, M. A, 2019, p. 3-16 [62].

---

[1] QDs are also referred to as artificial atoms

### *1.4.1 Quantum dots*

QDs are nanocrystals in which charge carriers are confined in all three spatial dimensions. This confinement is typically achieved by fabricating the semiconductor with a very small size, usually consisting of several hundred to thousands of atoms per particle [63, 64]. Due to quantum confinement effects, QDs behave like artificial atoms, exhibiting controllable and discrete energy levels.

The main differences between QDs and atoms lie essentially in their size (approximately 0.1 nm for atoms versus around 100 nm for QDs), as well as in the shape and strength of the confining potential. In atoms, electrons are held together by the attractive Coulomb force exerted by the nucleus, whereas in QDs, the confinement arises from an effective electric field generated by background charges and gate voltages. The number of electrons in an atom can be changed by ionization, which typically requires applying a strong electric field. In contrast, the electron number in QDs is usually controlled by tuning the confinement potential [65].

These 0D confinement structures were first fabricated in the 1980s by Louis E. Brus [66]. The unique properties of these nanostructures, resulting from quantum confinement and edge effects, have attracted significant interest across multiple fields. Typical QDs range in size from about 2 nm to 10 nm [67, 68], although their dimensions primarily depend on the material used for fabrication. Generally, a system is classified as a QD when the nanoparticle radius $a$ is smaller than one of the characteristic length scales: $a_e$, $a_h$, or $a_{exc}$, which correspond to the Bohr radii of the electron, hole, and exciton, respectively. Quantum dots can be made from metallic materials (such as Ni, Co, Pt, Au) or semiconductors.

QDs derived from 2D materials, including graphene [69], $MoS_2$ [70], and phosphorene [71], exhibit several advantages such as photostability and low toxicity, comparable to conventional organic fluorophores and semiconductor QDs [72]. Owing to their novel optical and electronic properties, 2D material-derived QDs hold widespread potential for applications in bioimaging [73], photodynamic therapy [74], photodetection [75], among others. Among various types of QDs, BP QDs have attracted considerable interest due to their excellent properties, making them suitable for applications such as vapor sensors [76, 77], electronic devices [71], and cancer therapy [78], to name a few.

BP QDs were first synthesized by Zhang *et al.* [71], who employed a top-down solution-phase approach to obtain BP QDs with a lateral size of $4.9 \pm 1.6$ nm and thickness of $1.9 \pm 0.9$ nm (see Figure 14). However, these nanostructures have been produced using various techniques. Sofer *et al.* synthesized few-layer BP QDs with an average size of 15 nm and large bandgaps via centrifugation of colloidal BP nanoparticles [76]. In contrast, Xu *et al.* produced BP QDs with an average size of $2.1 \pm 0.9$ nm on a large scale using solvothermal synthesis [79].

Figure 14 – Morphology characterization of BP QDs. (a) TEM image of BP QDs. (b) Enlarged TEM image of BP QDs. (c, d) High-resolution TEM (HRTEM) images of BP QDs with different lattice fringes.

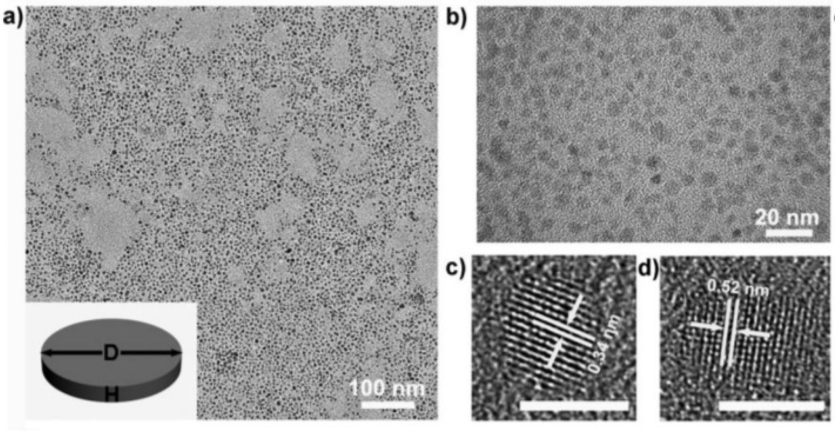

Source: GATENSBY, R. *et al.*, 2014 [71].

QDs derived from phosphorene are not perfectly circular and exhibit mixed edge configurations. As a consequence, the bandwidth varies with changes in the size of these QDs. It has been shown that the electronic properties of BP QDs depend not only on their size but also on their thickness. By tuning these parameters, both the structure and the band energy levels can be modified [80]. The optical properties of BP QDs have also been extensively investigated. For example, Niu *et al.* [81] studied the size-dependent optical behavior of BP QDs and concluded that the absorption gap is inversely proportional to the QD diameter. Similar to their electronic properties, the optical features of BP QDs have been demonstrated to be tunable. Abdelsalam *et al.*, for instance, found that in hexagonal armchair phosphorene QDs, absorption peaks in the low-energy region can be increased, decreased, or completely suppressed depending on the orientation of the applied electric field [82].

### *1.4.2 Quantum rings*

Nanostructures known as quantum rings (QRs) can be described as quantum flakes with a central antidot. This unique topology gives rise to an intriguing energy structure, particularly when a magnetic field is applied such that a flux penetrates the ring's interior. This class of low-dimensional systems has attracted significant interest, mainly because, in addition to quantum confinement, they enable the observation of quantum phase coherence effects on carrier transport, such as the Aharonov-Bohm [83] and Aharonov-Casher [84] effects.

Semiconductor-based QRs have been investigated both theoretically and experimentally [85]. Advances in the investigation and development of nanostructured devices with ring-like geometries, driven by experimental and theoretical physics, have enabled progress in fabricating QRs by various techniques, including lithography [86, 87] and etching [88]. QRs, like QDs, confine carriers in all three spatial directions and therefore exhibit a discrete density of states. However, QRs have attracted significant interest primarily because, as established by Aharonov and Bohm, their quantum mechanical properties are periodic with respect to the magnetic flux penetrating the ring [83].

Nanoscale QRs have been fabricated and proposed from various 2D materials, where the phase coherence length at low temperatures is larger than or comparable to their circumferences, making the Aharonov-Bohm effect observable. The first experimental realization of a QR structure was reported by Russo *et al.* [89], who investigated physical properties such as resistance and magnetoconductance under a magnetic field and reported the first systematic observation of Aharonov-Bohm conductance oscillations in a graphene QR (see Figure 15).

Figure 15 – (a) The main panel shows the two-probe measurement of the ring resistance *versus* back gate voltage at $T = 150$ mK. The charge neutrality point is at +4 V. Left inset: temperature dependence of the conductance measured for different values of gate voltage. Right inset: SEM image of a ring-shaped device etched in graphene similar to the one used in our measurements. (b) Magnetoconductance of the graphene ring measured at $T = 150$ mK and $V_G = +30$ V. On top of the non-periodic conductance fluctuations, periodic oscillations are clearly visible as also highlighted in the inset.

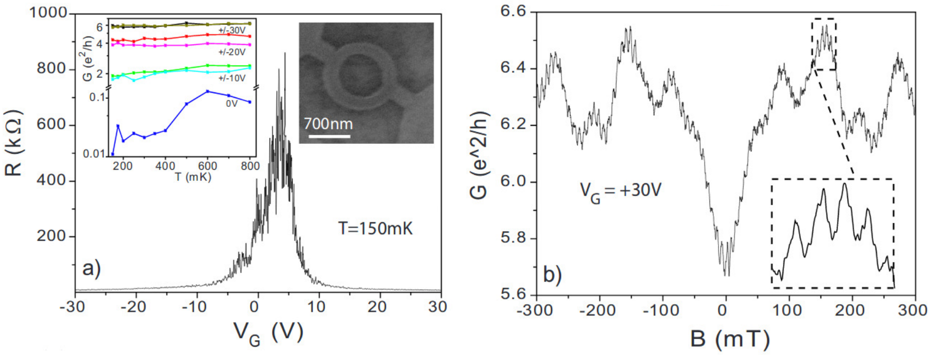

Source: RUSSO, R. *et al.*, 2008.

Numerous studies have since explored these quantum confinement systems. For instance, Costa *et al.* examined graphene QRs with varying geometries under magnetic fields and found that the energy spectrum and Aharonov-Bohm oscillations strongly depend on the geometry and edge structures of the nanorings [90]. Zhang *et al.* investigated the Aharonov-Bohm effect in monolayer phosphorene nanorings, revealing anisotropic and giant magnetoresistance in zigzag phosphorene nanorings [91].

## 1.5 Scope and original contribution of the thesis

This thesis investigates the electronic properties of quantum dots electrostatically confined in bilayer phosphorene. Chapter 1 provides the theoretical background necessary for the study of these systems, as well as the motivation for probing their physical properties. In Chapter 2, the theoretical framework underlying the investigation of these structures is developed, with a comprehensive description of the model adopted in this work. Chapter 3 is dedicated to the analysis and discussion of the results obtained for quantum dots. Finally, Chapter 4 presents the main conclusions and highlights potential perspectives emerging from the investigated systems and the results obtained throughout this thesis.

The method proposed to confine charge carriers in bilayer phosphorene not only avoids the complexities of lithographic fabrication but also leverages the material's anisotropy and layer-dependent bandgap to offer a flexible platform for systematically probing quantum states and their response to external fields, highlighting both the novelty and practical relevance of this work.

# 2 THEORETICAL MODEL: MULTILAYER PHOSPHORENE

In the previous Chapter 1, the fundamental physical concepts related to band theory (Sec. 1.3) in solid-state physics were introduced. Additionally, two approaches for determining the band structures of crystals were briefly discussed: the tight-binding model (Subsec. 1.3.2) and the effective mass approximation (Subsec. 1.3.3). In the present Chapter 2, these two methods are applied to the case of monolayer and bilayer phosphorene.

It is important to note that the effective mass approximation is not intended as an alternative to the tight-binding model, but rather as a complementary approach. While the tight-binding model provides detailed numerical descriptions of the electronic structure, the effective mass approximation offers physical intuition and analytical insight, allowing us to interpret the results more transparently. In particular, it facilitates the understanding of low-energy electronic excitations and the anisotropic behavior of carriers in phosphorene, which would be less obvious from tight-binding calculations alone.

The subsequent calculations are based on a proposed tight-binding Hamiltonian comprising 14 hopping parameters, whose values (lattice constants and hopping energies) were obtained through GW-DFT calculations, as discussed in Ref. [92], and adopted in the derivation of the multilayer BP model presented in Ref. [93].

## 2.1 Tight-binding model

### 2.1.1 *Monolayer phosphorene*

In terms of a BP sheet, at least four atoms (A, B, C, and D) are required to form the atomic structure of phosphorene. Let the tight-binding Hamiltonian in the second quantization be

$$H = \sum_i \epsilon_i a_i^\dagger b_j + \sum_{ij} t_{ij} d_i^\dagger c_j, \tag{2.1}$$

where $\epsilon_i$ are the on-site energy at sites $i$, $t_{ij}$ are the hopping parameter between sites $i$ and $j$, $a^\dagger(d^\dagger)$ and $b(c)$ are the creation and annihilation operators, respectively. Performing the Fourier transform of the field operators leads to

$$a_i^\dagger = \frac{1}{\sqrt{N}} \sum_k e^{-ik\cdot r_i} a_k^\dagger, \tag{2.2}$$

and

$$b_j = \frac{1}{\sqrt{N}} \sum_k e^{ik\cdot r_i} b_k. \tag{2.3}$$

By performing a similar procedure with $d^\dagger$ and $c$, the tight-binding Hamiltonian can be rewritten as follows.

$$H = \frac{1}{N}\sum_{i}\sum_{k,k'}\epsilon_i e^{ik\cdot r_i}e^{-ik'\cdot r_i}a^\dagger_{k'}b_k + \frac{1}{N}\sum_{i,j}\sum_{k,k'}t_{ij}e^{ik\cdot r_i}e^{-ik'\cdot r_j}d^\dagger_{k'}c_k. \tag{2.4}$$

In order to derive the tight-binding model for monolayer phosphorene, we use the Hamiltonian within the 10-hopping approach expressed by [93]

$$H_{mono} = \begin{pmatrix} H_0 & H_2 \\ H_2 & H_0 \end{pmatrix}, \tag{2.5}$$

where

$$H_0 = \begin{pmatrix} t_{AA}(k) & t_{AB}(k) \\ t^*_{AB}(k) & t_{AA}(k) \end{pmatrix}, \tag{2.6a}$$

$$H_2 = \begin{pmatrix} t_{AD}(k) & t_{AC}(k) \\ t^*_{AC}(k) & t_{AD}(k) \end{pmatrix}. \tag{2.6b}$$

The indices $ij$ of the structure factors refer to the connections between the four sublattices of phosphorene (A, B, C, and D) and involve the hopping parameters of the crystalline structure of BP.

Aiming to express the structure factors representing the matrix elements of the tight-binding Hamiltonian adopted in our work, we consider Figure 16, which shows the lattice distances, bond angles, and the 10 intralayer hopping parameters used in our model, where $a_1 = 2.22$Å ($a_2 = 2.24$Å) is the distance between nearest-neighbor sites in sublattices $A$ and $B$ or $C$ and $D$ ($A$ and $C$ or $B$ and $D$), $\alpha_1 = 96.5°$, $\alpha_2 = 101.9°$, and $\beta = 72°$.

Figure 16 – Side view of a monolayer BP, indicating the four sublattices: A and B at the bottom sublayer, and C and D at the top sublayer.

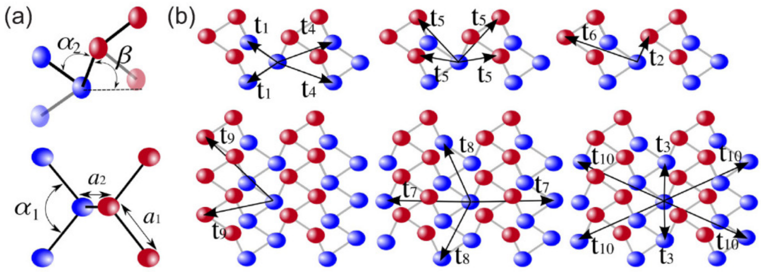

Source: DE SOUSA, J. P. D. *et al.*, 2017 [93].

Let us first compute the expression for $t_{AB}$, which corresponds to all the terms associated with the coupling energies between $A - B$. Therefore, by analyzing Figure 16(b) and using the second quantization formalism introduced earlier, we have the following:

$$\mathcal{H}_{AB} = \sum_{i,j} t_{ij}(a_i^\dagger b_j + d_i^\dagger c_j) + h.c. = t_1 \sum_{i,j}(a_i^\dagger b_j + d_i^\dagger c_j) \\ + t_4 \sum_{i,j}(a_i^\dagger b_j + d_i^\dagger c_j) + t_8 \sum_{i,j}(a_i^\dagger b_j + d_i^\dagger c_j) + h.c. \tag{2.7}$$

Changing $t_1$, $t_4$ and $t_8$ by $t_n$, one has

$$\begin{aligned} t_n \sum_{i,j}(a_i^\dagger b_j + d_i^\dagger c_j) &= \frac{t_n}{N} \sum_{i,j,k,k'} (a_k^\dagger b_{k'} + d_k^\dagger c_{k'}) e^{-i\vec{k}\cdot\vec{r_i}} e^{i\vec{k'}\cdot\vec{r_j}} \\ &= \frac{t_n}{N} \sum_{i,j,k,k'} (a_k^\dagger b_{k'} + d_k^\dagger c_{k'}) e^{i\vec{k}\cdot(\vec{r_i}-\vec{r_j})} e^{i(\vec{k'}-\vec{k})\cdot\vec{r_j}} \\ &= \sum_k \left( t_n \sum_{m_n} e^{i\vec{k}\cdot\vec{\delta}_m} \right) (a_k^\dagger b_k + d_k^\dagger c_k), \end{aligned} \tag{2.8}$$

where $\sum_{m_n}$ is a summation over all $\vec{r_j}$ neighbors of $\vec{r_i}$ linked by the hopping $t_n$ and $\vec{\delta_i} = \vec{r_i} - \vec{r_j}$ corresponds to the distance vector between the atomic site $i$ and $j$. Therefore, we get the following expression:

$$\mathcal{H}_{AB} = \sum_k \left( t_1 \sum_{m_1} e^{i\vec{k}\cdot\vec{\delta}_{m_1}} + t_4 \sum_{m_4} e^{i\vec{k}\cdot\vec{\delta}_{m_4}} + t_8 \sum_{m_8} e^{i\vec{k}\cdot\vec{\delta}_{m_8}} \right) \\ \times (a_k^\dagger b_k + d_k^\dagger c_k) + h.c. = \sum_k t_{AB}(k)(a_k^\dagger b_k + d_k^\dagger c_k) + h.c. \tag{2.9}$$

Note that we used $t_1$, $t_4$, and $t_8$ in this case because if we consider an electron at sublattice A, it can hop to sublattice B via these parameters. The $t_{AB}$ term can be better explained if we consider Figure 17, where the hopping vectors related to $t_1$, $t_4$, and $t_8$ are shown.

Figure 17 – Hopping vectors from an origin site at lattice A to a site at lattice B.

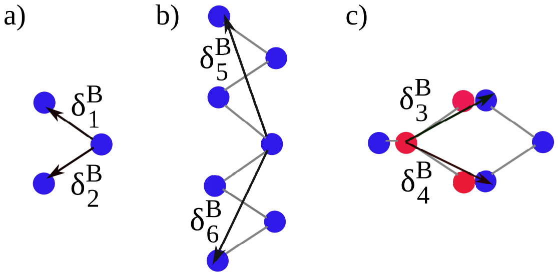

Source: Prepared by the author.

Therefore, considering the atom distances and the bond angles, the hopping vectors associated with $t_1$ are written as follows

$$\delta_1^B = -a_1 sin(\alpha_1/2)\hat{x} - a_1 cos(\alpha_1/2)\hat{y}, \tag{2.10a}$$

$$\delta_2^B = a_1 sin(\alpha_1/2)\hat{x} - a_1 cos(\alpha_1/2)\hat{y}. \tag{2.10b}$$

Regarding the terms associated to $t_4$, we have

$$\delta_3^B = -a_1 sin(\alpha_1/2)\hat{x} + [a_1 cos(\alpha_1/2) + 2a_2 cos\beta]\hat{y}, \tag{2.11a}$$

$$\delta_4^B = a_1 sin(\alpha_1/2)\hat{x} + [a_1 cos(\alpha_1/2) + 2a_2 cos\beta]\hat{y}. \tag{2.11b}$$

Finally, the ones related to $t_8$

$$\delta_5^B = -3a_1 sin(\alpha_1/2)\hat{x} + -a_1 cos(\alpha_1/2)\hat{y}, \tag{2.12a}$$

$$\delta_6^B = 3a_1 sin(\alpha_1/2)\hat{x} + -a_1 cos(\alpha_1/2)\hat{y}. \tag{2.12b}$$

Thus, after some manipulations, we can express the structure factor $t_{AB}$ by

$$\begin{aligned} t_{AB}(k) = {} & 2t_1 \cos\left[a_1 \sin(\alpha_1/2)k_x\right] e^{-ia_1 \cos(\alpha_1/2)k_y} \\ & + 2t_4 \cos\left[a_1 \sin(\alpha_1/2)k_x\right] e^{i[2a_2 \cos\beta + a_1 \cos(\alpha_1/2)]k_y} \\ & + 2t_8 \cos\left[3a_1 \sin(\alpha_1/2)k_x\right] e^{-ia_1 \cos(\alpha_1/2)k_y}. \end{aligned} \tag{2.13}$$

By performing a similar procedure, we can obtain the ($t_{AA}$, $t_{AC}$, and $t_{AD}$) coupling contributions

$$\begin{aligned} t_{AA}(k) = {} & 2t_3 \cos\left[2a_1 \sin(\alpha_1/2)k_x\right] \\ & + 2t_7 \cos\{\left[2a_1 \cos(\alpha_1/2) + 2a_2 \cos\beta\right] k_y\} \\ & + 4t_{10} \cos\left[2a_1 \sin(\alpha_1/2)k_x\right] \\ & \times \cos\{\left[2a_1 \cos(\alpha_1/2) + 2a_2 \cos\beta\right] k_y\}. \end{aligned} \tag{2.14a}$$

$$\begin{aligned} t_{AC}(k) = {} & t_2 e^{ia_2 \cos(\beta)k_y} + t_6 e^{-i[a_2 \cos\beta + 2a_1 \cos(\alpha_1/2)]k_y} \\ & + 2t_9 \cos\left[2a_1 \sin(\alpha_1/2)k_x\right] e^{-i[a_2 \cos\beta + 2a_1 \cos(\alpha_1/2)]k_y}. \end{aligned} \tag{2.14b}$$

$$\begin{aligned} t_{AD}(k) = {} & 4t_5 \cos\left[a_1 \sin(\alpha_1/2)k_x\right] \\ & \times \cos\{\left[a_1 \cos(\alpha_1/2) + a_2 \cos\beta\right] k_y\}. \end{aligned} \tag{2.14c}$$

After defining each element of the Hamiltonian, the eigenstates can be represented as four-component spinors, $\Phi = [\phi_A \quad \phi_B \quad \phi_D \quad \phi_C]^T$. With the complete monolayer Hamiltonian established, it can be conveniently rewritten in block form by applying the following unitary transformation

$$U = \frac{1}{\sqrt{2}} \begin{pmatrix} 1 & 0 & 1 & 0 \\ 0 & 1 & 0 & 1 \\ 1 & 0 & -1 & 0 \\ 0 & 1 & 0 & -1 \end{pmatrix}. \tag{2.15}$$

Thus, the new Hamiltonian and eigenvectors are obtained by doing $H'_k = U \dagger H_k U$ and $\Psi'_k = U\Psi_k$, where

$$H'_k = \begin{pmatrix} t_{AA} + t_{AD} & t_{AB} + t_{AC} & 0 & 0 \\ t^*_{AC} + t_{AB} & t_{AA} + t_{AD} & 0 & 0 \\ 0 & 0 & t_{AA} - t_{AD} & t_{AB} - t_{AC} \\ 0 & 0 & t^*_{AB} - t^*_{AC} & t_{AA} - t_{AD} \end{pmatrix}, \tag{2.16}$$

and

$$\Psi_k = \begin{pmatrix} \phi_A + \phi_D \\ \phi_B + \phi_C \\ \phi_A - \phi_D \\ \phi_B - \phi_C \end{pmatrix}. \tag{2.17}$$

The above Hamiltonian and eigenstates can be written as follows:

$$H'_k = \begin{pmatrix} H^+_k & 0 \\ 0 & H^-_k \end{pmatrix}, \quad \text{and} \quad \psi'_k = \begin{pmatrix} \Psi^+_k \\ \Psi^-_k \end{pmatrix}, \tag{2.18}$$

where

$$H^\pm_k = H_0 \pm H_2, \quad \text{and} \quad \Psi^\pm_k = \begin{pmatrix} \phi_A \pm \phi_D \\ \phi_B \pm \phi_C \end{pmatrix}. \tag{2.19}$$

By diagonalizing the Hamiltonian (2.19), we obtain the following expression for the energy bands

$$E^\pm_s(k) = t_{AA}(k) \pm t_{AD}(k) + s|t_{AB}(k) \pm t_{AC}(k)|, \tag{2.20}$$

where s = ± denotes the valence (+) and conduction (-) bands, respectively. The 10-intralayer parameter values for the tight-binding model are depicted in Table 1 [92].

### 2.1.2 *Bilayer phosphorene*

The procedure for obtaining the energy bands of bilayer phosphorene closely follows that of the monolayer, with the inclusion of five additional interlayer hopping parameters, as summarized in Table 2. In this case, the unit cell comprises eight atoms, as depicted in Figure 18, which also illustrates the five types of interlayer hopping.

Figure 18 – Bilayer phosphorene lattice and the five types of interlayer hopping. The solid and semitransparent meshes represent the upper and lower phosphorene layers, respectively. The rectangle indicates the unit cell.

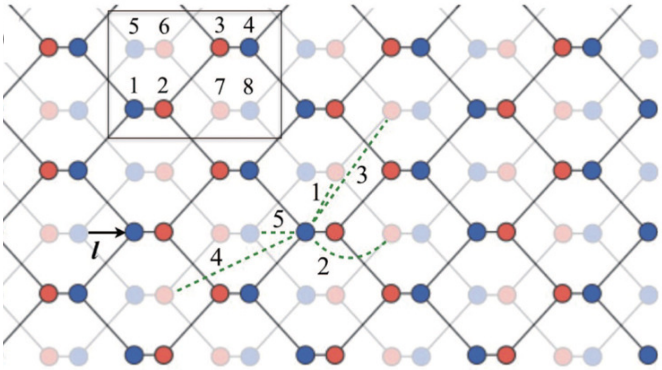

Source: SHI, H. *et al.*, 2018 [94].

The 8 × 8 Hamiltonian can be expressed as

$$H_{bilayer} = \begin{pmatrix} H_0 & H_2 & 0 & 0 \\ H_2 & H_0 & H_3 & 0 \\ 0 & H_3 & H_0 & H_2 \\ 0 & 0 & H_2 & H_0 \end{pmatrix}, \quad \text{and} \quad \Psi_{bi} = \begin{pmatrix} \Phi_1 \\ \Phi_2 \end{pmatrix}, \tag{2.21}$$

with $\Phi_i = [\phi_{A,i} \quad \phi_{B,i} \quad \phi_{D,i} \quad \phi_{C,i}]^T$, where $i = 1, 2$ is the layer index. $H_3$ contains the

Table 1 – Intralayer ($t_i$) hopping parameters.

| Parameter | Value (eV) | Parameter | Value (eV) |
|---|---|---|---|
| $t_1$ | $-1.486$ | $t_2$ | $3.729$ |
| $t_3$ | $-0.252$ | $t_4$ | $-0.071$ |
| $t_5$ | $-0.019$ | $t_6$ | $0.186$ |
| $t_7$ | $-0.063$ | $t_8$ | $0.101$ |
| $t_9$ | $-0.042$ | $t_{10}$ | $0.073$ |

Source: RUDENKO, M. *et al.*, 2015 [92].

contribution of the couplings between atomic sites located in adjacent layers, which is given by

$$H_3 = \begin{pmatrix} t_{AD'}(k) & t_{AC'}(k) \\ t^*_{AC'}(k) & t_{AD'}(k) \end{pmatrix}. \tag{2.22}$$

The Hamiltonian for bilayer phosphorene can be concisely written as

$$H_{bilayer} = \begin{pmatrix} H & H_c \\ H_c^\dagger & H \end{pmatrix}, \tag{2.23}$$

where

$$H = \begin{pmatrix} H_0 & H_2 \\ H_2 & H_0 \end{pmatrix}, \text{ and } H_c = \begin{pmatrix} 0 & H_3 \\ 0 & 0 \end{pmatrix}. \tag{2.24}$$

As in the case of monolayer BP, we can apply a unitary transformation, shown below, to rewrite the bilayer Hamiltonian and avoid dealing with eight coupled equations

$$U = \frac{1}{2}\begin{pmatrix} \mathbb{1} & \mathbb{1} & \mathbb{1} & \mathbb{1} \\ \mathbb{1} & \mathbb{1} & -\mathbb{1} & -\mathbb{1} \\ -i\mathbb{1} & i\mathbb{1} & -i\mathbb{1} & i\mathbb{1} \\ -i\mathbb{1} & i\mathbb{1} & i\mathbb{1} & -i\mathbb{1} \end{pmatrix}, \tag{2.25}$$

where $\mathbb{1}$ denotes the $2 \times 2$ unit matrix. Therefore, leading to

$$UH_{bilayer}U^\dagger = \begin{pmatrix} H_0 + H_2 + H_3/2 & \Delta/2 & 0 & iH_3/2 \\ \Delta & H_0 + H_2 - H_3/2 & -iH_3/2 & 0 \\ 0 & iH_3/2 & H_0 - H_2 - H_3/2 & \Delta/2 \\ -iH_3/2 & 0 & \Delta/2 & H_0 - H_2 + H_3/2 \end{pmatrix}. \tag{2.26}$$

The secondary diagonal terms can be discarded without significant loss of precision.

Table 2 – Interlayer ($t_i^\perp$) hopping parameters.

| Parameter | Value (eV) |
|---|---|
| $t_1^\perp$ | $0.524$ |
| $t_2^\perp$ | $0.180$ |
| $t_3^\perp$ | $-0.123$ |
| $t_4^\perp$ | $-0.168$ |
| $t_5^\perp$ | $0.000$ |

Source: RUDENKO, M. *et al.*, 2015 [92].

Thus, the final bilayer Hamiltonian is

$$H_k^{\pm} = \begin{pmatrix} H_0 \pm H_2 + H_3/2 & \Delta/2 \\ \Delta/2 & H_0 \pm H_2 - H_3/2 \end{pmatrix}, \tag{2.27}$$

where the Hamiltonian $H_k^+$ ($H_k^-$) describes the low (high) energy bands. The eigenstates of $H_k^{\pm}$ are

$$\Psi_k^{\pm} = \frac{e^{i\theta_\pm}}{2} \begin{pmatrix} (\phi_{A,1} \pm \phi_{D,1}) + (\phi_{A,2} \pm \phi_{D,2}) \\ (\phi_{B,1} \pm \phi_{C,1}) + (\phi_{B,2} \pm \phi_{C,2}) \\ (\phi_{A,1} \pm \phi_{D,1}) - (\phi_{A,2} \pm \phi_{D,2}) \\ (\phi_{B,1} \pm \phi_{C,1}) - (\phi_{B,2} \pm \phi_{C,2}) \end{pmatrix}, \tag{2.28}$$

with $\theta_+ = 0$ and $\theta_- = -\pi/2$. Therefore, by diagonalizing the Hamiltonian (2.27), we can write the energy bands close to the Fermi levels as follows

$$E_c = \frac{\epsilon_1^+ + \epsilon_2^+ + \epsilon_1^- + \epsilon_2^-}{2} \pm \sqrt{\left[\frac{\epsilon_1^+ + \epsilon_2^+ - \epsilon_1^- - \epsilon_2^-}{2}\right]^2 + \left(\frac{\Delta}{2}\right)^2}, \tag{2.29a}$$

$$E_v = \frac{\epsilon_1^+ - \epsilon_2^+ + \epsilon_1^- - \epsilon_2^-}{2} \pm \sqrt{\left[\frac{\epsilon_1^+ - \epsilon_2^+ - \epsilon_1^- + \epsilon_2^-}{2}\right]^2 + \left(\frac{\Delta}{2}\right)^2}, \tag{2.29b}$$

where ($E_c$) and ($E_v$) are the conduction and the valence bands, respectively. The functions of the wavevector $\epsilon_i^{\pm}$, with $i = 1, 2$, are defined by

$$\epsilon_1^{\pm} = t_{AA}(k) + t_{AD}(k) \pm t_{AD'}(k)/2, \tag{2.30a}$$

$$\epsilon_2^{\pm} = |t_{AB}(k) + t_{AC}(k) \pm t_{AC'}(k)/2|. \tag{2.30b}$$

## 2.2 Continuum model

The tight-binding model derived in the previous section is considered a suitable and straightforward approach to obtain the electronic properties of different materials. However, the hopping parameters are not analytically tractable when investigating the electronic properties away from the $\Gamma$ point in the Brillouin zone [93]. Therefore, in order to obtain an even simpler model that enables analytical calculations, the long-wavelength approximation is proposed. In this approach, also known as the continuum approximation, the structure factors $t_{AA}(k)$, $t_{AB}(k)$, $t_{AC}(k)$, $t_{AD}(k)$, $t_{AC'}(k)$, and $t_{AD'}(k)$, obtained previously, are expanded around the $\Gamma$ point. The applicability of this model is not restricted to the monolayer case, and, when compared to other models such as tight-binding, it is less computationally demanding. Thus, by expanding

Table 3 – Structure factor coefficients for ten-hopping continuum approximation.

| | 10-hopping | units |
|---|---|---|
| $\delta_{AA}$ | -0.338 | eV |
| $\delta_{AB}$ | -2.912 | eV |
| $\delta_{AC}$ | 3.831 | eV |
| $\delta_{AD}$ | -0.076 | eV |
| $\delta_{AC'}$ | 0.712 | eV |
| $\delta_{AD'}$ | -0.132 | eV |
| $\eta_{AA}$ | 1.161 | eV·Å$^2$ |
| $\eta_{AB}$ | 2.05 | eV·Å$^2$ |
| $\eta_{AC}$ | 0.460 | eV·Å$^2$ |
| $\eta_{AD}$ | 0.104 | eV·Å$^2$ |
| $\eta_{AC'}$ | -0.9765 | eV·Å$^2$ |
| $\eta_{AD'}$ | 2.699 | eV·Å$^2$ |
| $\gamma_{AA}$ | -1.563 | eV·Å$^2$ |
| $\gamma_{AB}$ | 3.607 | eV·Å$^2$ |
| $\gamma_{AC}$ | -1.572 | eV·Å$^2$ |
| $\gamma_{AD}$ | 0.179 | eV·Å$^2$ |
| $\gamma_{AC'}$ | 2.443 | eV·Å$^2$ |
| $\gamma_{AD'}$ | 0.364 | eV·Å$^2$ |
| $\chi_{AB}$ | 3.688 | eV·Å |
| $\chi_{AC}$ | 2.208 | eV·Å |
| $\chi_{AC'}$ | 2.071 | eV·Å |

Source: SOUSA, J. P. D. *et al.*, 2017 [93].

the structure factors up to second order in $k$, one obtains the following expressions:

$$t_{AA} = \delta_{AA} + \eta_{AA}k_x^2 + \gamma_{AA}k_y^2, \tag{2.31a}$$

$$t_{AB} = \delta_{AB} + \eta_{AB}k_x^2 + \gamma_{AB}k_y^2 + i\chi_{AB}k_y, \tag{2.31b}$$

$$t_{AC} = \delta_{AC} + \eta_{AC}k_x^2 + \gamma_{AC}k_y^2 + i\chi_{AC}k_y, \tag{2.31c}$$

$$t_{AD} = \delta_{AD} + \eta_{AD}k_x^2 + \gamma_{AD}k_y^2, \tag{2.31d}$$

regarding the intralayer terms and

$$t_{AC'} = \delta_{AC'} + \eta_{AC'}k_x^2 + \gamma_{AC'}k_y^2 + i\chi_{AC}k_y, \tag{2.32a}$$

$$t_{AD'} = \delta_{AD'} + \eta_{AD'}k_x^2 + \gamma_{AD'}k_y^2, \tag{2.32b}$$

for the interlayer contributions. The coefficient values of the expanded structure factors for the ten-hopping model are presented in Table 3.

### *2.2.1 Monolayer phosphorene*

The Hamiltonian in the long-wavelength context for the monolayer BP, considering the ten-hopping description for $H_k^+$, is expressed by

$$H_k^+ = \begin{pmatrix} u_0+\eta_x k_x^2+\eta_y k_y^2 & \delta+\gamma_x k_x^2+\gamma_y k_y^2+i\chi k_y \\ \delta+\gamma_x k_x^2+\gamma_y k_y^2-i\chi k_y & u_0+\eta_x k_x^2+\eta_y k_y^2 \end{pmatrix}. \tag{2.33}$$

The values of the coefficients in Eq. (2.33) are given by $u_0 = \delta_{AA} + \delta_{AD}$, $\eta_x = \eta_{AA} + \eta_{AD}$, $\eta_y = \gamma_{AA} + \gamma_{AD}$, $\delta = \delta_{AB} + \delta_{AC}$, $\gamma_x = \eta_{AB} + \eta_{AC}$, $\gamma_y = \gamma_{AB} + \gamma_{AC}$, and $\chi = \chi_{AB} + \chi_{AC}$. The dispersion relations for electrons and holes are obtained by diagonalizing the Hamiltonian (2.33), thus

$$E_k^+ = u_0 + \eta_x k_x^2 + \eta_y k_y^2 \pm \sqrt{(\delta + \gamma_x k_x^2 + \gamma_y k_y^2)^2 + \chi^2 k_y^2}, \tag{2.34}$$

where the plus (minus) sign generates the conduction (valence) band.

### *2.2.2 Bilayer phosphorene*

Similarly to the monolayer case, we can derive for bilayer BP a long-wavelength Hamiltonian describing the lowest energy bands close to the Fermi level as follows

$$H_0 + H_2 \pm H_3/2 = \begin{pmatrix} u_0^\pm+\eta_x^\pm k_x^2+\eta_y^\pm k_y^2 & \delta^\pm+\gamma_x^\pm k_x^2+\gamma_y^\pm k_y^2+i\chi^\pm k_y \\ \delta^\pm+\gamma_x^\pm k_x^2+\gamma_y^\pm k_y^2-i\chi^\pm k_y & u_0^\pm+\eta_x^\pm k_x^2+\eta_y^\pm k_y^2 \end{pmatrix}, \tag{2.35}$$

where $u_0^\pm = u_0 \pm \delta_{AD'}/2$, $\eta_x^\pm = \eta_x \pm \eta_{AD'}/2$, $\eta_y^\pm = \eta_y \pm \gamma_{AD'}/2$, $\delta^\pm = \delta \pm \delta_{AC'}/2$, $\gamma_x^\pm = \gamma_x \pm \eta_{AC'}/2$, $\gamma_y^\pm = \gamma_y \pm \gamma_{AC'}/2$, and $\chi^\pm = \chi \pm \chi_{AC'}/2$. Note that the low-energy Hamiltonian for bilayer BP (2.35) has the same structure as the monolayer Hamiltonian (2.33) for a zero bias situation ($\Delta = 0$) in the long-wavelength limit. The low-energy bands obtained from Eq. (2.35) at the $\Gamma$ point are given by Eqs. (2.29a) and (2.29b) with

$$\epsilon_1^\pm = u_0^\pm + \eta_x^\pm k_x^2 + \eta_y^\pm k_y^2, \tag{2.36a}$$

$$\epsilon_2^\pm = \sqrt{(\delta^\pm + \gamma_x^\pm k_x^2 + \gamma_y^\pm k_y^2)^2 + (\chi^+ k_y)^2}. \tag{2.36b}$$

Considering a zero bias case ($\Delta = 0$), the energy levels are given by $\epsilon_1^\pm + s\epsilon_2^\pm$, *i.e.*

$$E_s^\pm = u_0^\pm + \eta_x^\pm k_x^2 + \eta_y^\pm k_y^2 + s\sqrt{(\delta^\pm + \gamma_x^\pm k_x^2 + \gamma_y^\pm k_y^2)^2 + (\chi^\pm k_y)^2}, \tag{2.37}$$

with $s = \pm 1$, where the positive (negative) sign denotes the conduction (valence) bands. One can notice that Eq. (2.37) has exactly the same structure as the energy bands of the monolayer case Eq. (2.34), as already expected.

## 2.3 Effective mass approximation

Considering Eq. (2.37), which represents the dispersion relation for the conduction and the valence bands, one can estimate the effective masses of electrons and holes in BP from the following equation

$$\frac{\hbar^2}{m_i^j} = \frac{\partial^2 E_k^j}{\partial k_i^2}, \tag{2.38}$$

where $j = \pm$ represents electrons and holes, respectively, and $i = \{x, y\}$ describes the in-plane directions. By doing that, we get the following expressions

$$m_x^e = \frac{\hbar^2}{2(\eta_x + \gamma_x)}, \text{ and } m_y^e = \frac{\hbar^2}{2(\eta_y + \gamma_y + \chi^2/(2\delta))}, \tag{2.39}$$

for electrons in the $x$ and $y$ directions, and

$$m_x^h = \frac{\hbar^2}{2(\eta_x - \gamma_x)}, \text{ and } m_y^h = \frac{\hbar^2}{2(\eta_y - \gamma_y - \chi^2/(2\delta))}, \tag{2.40}$$

for holes in the $x$ and $y$ directions. Finally, we replace these effective masses in Eq. (2.37) to express the dispersion relations for electrons and holes as follows

$$E_k^e = u_0 + \delta + \frac{\hbar^2}{2m_x^e}k_x^2 + \frac{\hbar^2}{2m_y^e}k_y^2, \tag{2.41}$$

and

$$E_k^h = u_0 - \delta + \frac{\hbar^2}{2m_x^h}k_x^2 + \frac{\hbar^2}{2m_y^h}k_y^2. \tag{2.42}$$

Even though it is a simple approach to describe the properties of phosphorene, interesting results can be extracted from this model, such as in Ref. [95].

Considering the approaches discussed here, Figure 19 shows the behavior of the effective masses in units of $m_0$ for electrons and holes along the x-y directions as a function of the number of layers. A salient feature of phosphorene is its pronounced electronic anisotropy, which is directly reflected in the effective mass parameters. We can see that the effective masses for electrons and holes along the x direction tend to be more sensitive to variations in the number of layers than along the y direction. Specifically, carriers experience lighter effective masses along the armchair direction and heavier ones along the zigzag direction, a behavior captured naturally by the effective mass model. This directional dependence is crucial for understanding transport properties and device performance, highlighting the relevance of the effective mass approximation in complementing the tight-binding results.

In Figure 20, we present the comparison between the dispersion relations obtained using the tight-binding model, the continuum approximation, and the effective mass approach for different numbers of phosphorene layers ($N = 1$ to $N = 4$). The black solid curves

Figure 19 – Effective (a) electron and (b) hole masses of multilayer phosphorene in units of free electron mass ($m_0$). Blue solid and red dashed curves correspond to masses along the x (zigzag) and y (armchair) directions, respectively.

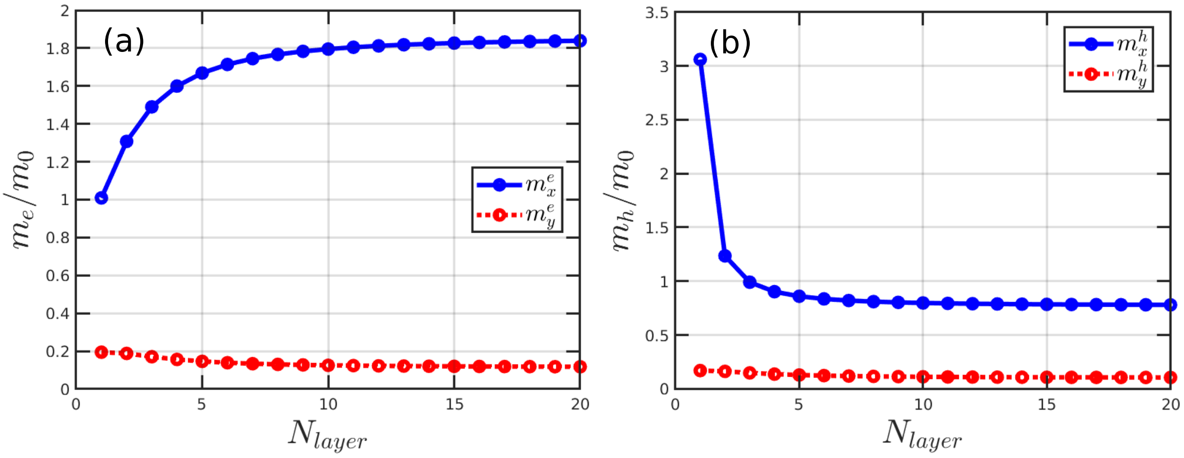

Source: SOUSA, J. P. D. *et al.*, 2017 [93].

correspond to the tight-binding model, the red dashed curves to the continuum approximation, and the blue dotted curves to the effective mass approach. It can be observed that, for small wave vector $k$ values near the $\Gamma$ point, both the continuum approximation and the effective mass model show excellent agreement with the tight-binding results. This indicates that, in the low-energy region where the band curvature is small, simplified models can accurately describe the electronic dispersion.

Figure 20 – Multilayer phosphorene band structures for (a) $N = 1$, (b) $N = 2$, (c) $N = 3$, and (d) $N = 4$ layers. Black solid, red dashed, and blue dotted curves correspond to levels obtained via the tight-binding model, continuum approximation, and effective mass approach, respectively.

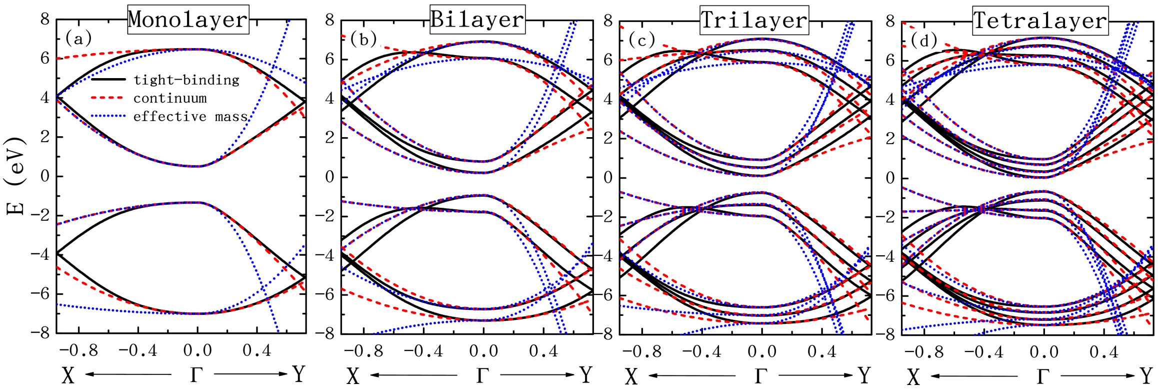

Source: Prepared by the author.

In summary, both the tight-binding and effective mass models provide valuable insights into the electronic properties of phosphorene. The tight-binding approach offers a detailed numerical description of the band structure, while the effective mass approximation allows for analytical treatment and a clearer physical understanding, especially regarding anisotropic carrier behavior. Together, these complementary methods furnish a comprehensive and robust framework for investigating the low-energy electronic properties of monolayer and bilayer phosphorene.

# 3 ELECTROSTATICALLY CONFINED QUANTUM DOTS IN BILAYER PHOSPHORENE

It is known that breaking the inversion symmetry in bilayer graphene opens a gap. On the other hand, in the case of bilayer phosphorene, the opposite effect occurs. By applying a position-dependent bias potential in bilayer phosphorene that breaks the inversion symmetry, we demonstrate theoretically that nanostructures, such as quantum dots, can be realized. Using the tight-binding model, we investigate the electron- and hole-confined states for a circularly symmetric potential, where the charge carriers are confined in the non-zero bias region. The energy spectrum and wave functions of bilayer phosphorene quantum dots are explored in the absence and the presence of a perpendicular magnetic field, emphasizing the spatial localization preference of the bound states for different energy regimes, namely, above and below the critical bias value associated with the gap closing and the emergence of two Dirac-like cones in bilayer phosphorene spectrum.

## 3.1 Introduction

The confinement of charge carriers in semiconductor nanostructures has been intensively studied over the last three decades [96, 97]. Electrons and holes can be confined in a wide variety of nanostructures designed with different shapes and symmetries, such as QDs [98, 99, 100, 101]. Soon after the discovery of graphene [1], a considerable number of studies proposed confinement of charge carriers into finite regions, either by induced electrostatic gates [102, 103, 104, 105, 106] or by cutting out a finite region from the infinite 2D sheet [90, 107, 108, 109, 110, 111, 112, 113, 114, 115]. These studies on graphene have also boosted the search for other 2D materials with semiconductor features, in contrast to graphene that exhibits a semimetallic dispersion relation [1], and their use in novel high-performance devices based on nanostructures with optoelectronic advantages. [116, 117, 118, 119]

Among the promising new 2D materials, few-layer BP[120] has evoked great interest, mainly because of its highly anisotropic gapped band structure, which leads to large anisotropic effective masses, group velocities, and ambipolar mobilities for the carriers along zigzag and armchair directions [121, 122, 9, 30, 23, 29, 123, 31, 26], and consequently large on-off current ratio [15, 124]. Such features are due to the $sp^3$ hybridization of the phosphorus atoms that leads to a puckered crystallographic structure for BP [120, 29, 123]. Similar to graphene, each BP monolayer, named phosphorene, has three nearest-neighbors covalently bonded, and van der Waals interactions hold the BP layers together. Because of this weak interaction between the stacked layers, monolayer and bilayer (BL) BP can be experimentally obtained by mechanical exfoliation [9, 125, 123, 15, 126, 127, 128]. An additional key ingredient of BP that differentiates it from graphene is its sizable and tunable direct bandgap [33, 129, 130] at the $\Gamma$ point, which is an important feature for practical applications [24, 34, 131], with bandgap ranging from $\sim$2 eV in monolayer case to $\sim$0.3 eV in bulk case.

In addition to the dependence on the number of BP layers, it was experimentally [132, 133] demonstrated and theoretically [134, 135, 136, 137] discussed the tunability of the BL BP bandgap under the presence of a perpendicular electric field. In contrast to the BL graphene case[138, 139], in which the application of gate voltages opens the energy gap, for the BL BP case, the bias-induced breaking of the inversion symmetry leads to a bandgap closing, *i.e.*, a semiconductor-to-semimetal transition induced in biased BL BP with the appearance of two Dirac-like cones for high gate voltages due to the conduction-valence band inversion.

A natural research path to follow, analogously to the beginning era of graphene and its optoelectronic nanostructures-based proposals, [102, 103, 104, 105, 106, 90, 107, 108, 109, 110, 111, 112, 113, 114, 115] is to explore multilayer phosphorene quantum confinement nanostructures. BP QDs [140, 141, 142, 143, 124, 71, 144, 145, 146, 147, 148, 81, 149, 150, 151] are zero-dimensional examples of BP nanostructures that have been a topic of research in the last few years. BP QDs were first synthesized in 2015 by Zang *et al.*, who used liquid-phase ultrasonic exfoliation [71]. Besides that synthesis method, other approaches have been employed for the preparation of BP QDs, such as electrochemical exfoliation, solvothermal treatment, blender breaking, and pulsed laser irradiation [124, 71]. Very recently, it has been reported that BP QDs were obtained via shock-induced phase transformation using ball-milled red phosphorus nanopowder as a precursor [140, 141]. Studies on BP QDs focus not only on their fabrication but also on the characterization and manipulation of their physical properties aiming to explore the effects of their anisotropic properties, owing to potential technological applications, such as in bioimaging, cancer therapy, intelligent devices, optoelectronic, gas sensing, and solar cells. [124, 149, 152, 150]

From the theoretical point of view, Zhang *et al.* [143] in 2015 reported one of the first tight-binding results (Landau levels and optical absorption spectra) for rectangular, hexagonal, and triangular monolayer phosphorene QDs. In 2016, Jiang *et al.* [153] presented numerical results for the energy spectra of triangular zigzag BP QDs. In the following years, several other theoretical works [144, 148, 147, 145, 81, 154, 155, 156, 152, 91, 151, 146] showed the effects of different structural crystallographic features, such as the shape, size, and edge types, on the electronic, magneto-optical and transport properties of monolayer BP dotlike nanostructures, similar to the monolayer graphene QD [112] cases. The influence of the layer population's degree of freedom in the physical properties for the confined charge carriers in BL [157, 158, 159, 160, 161] and multilayer [82, 162] BP nanostructures was also reported. For instance, Li *et al.*[157] and Zare *et al.*[158] investigated the electronic properties of rectangular BL BP QDs in the presence of perpendicular electric and magnetic fields, and Jiang *et al.* [159] and Liang *et al.* [162] studied similar systems with triangular geometries for BL BP QDs. In all these studies, the nanostructures were assumed to exhibit regular edges, which demand high-quality samples with well-controlled edge-type preparation.

In contrast to the previously investigated BL BP nanostructures, [82, 157, 158, 159, 160, 161, 162] in this work, we propose BL BP QDs based on the use of electrostatic gate potentials, which do not require any complicated tailoring of the phosphorene lattice, in a similar way as in bias-defined BL graphene QDs [103]. However, unlike the BL graphene case in which the charge carriers are confined in the finite BL graphene region with zero bias due to the gap opening in the presence of electrostatic gates, for the BL BP case, we show that confined states are localized in the region with a finite electric field. For that, we study, by means of a tight-binding model, the behavior of the energy levels and wave functions for different system parameters, as well as the influence of a magnetic field on their electronic features.

This chapter is organized as follows. In Sec. 3.2, we present the theoretical framework used to describe the confined charge carriers in BL BP based on the tight-binding model. The results in the presence and absence of a perpendicular magnetic field are discussed in Sec. 3.3. Finally, in Sec. 3.4, we report the concluding remarks.

### 3.2 Theoretical model

The BL phosphorene is an orthorhombic crystal structure of two coupled BP layers separated by a distance of $\approx 3.214$ Å. Its crystalline structure is composed of eight sublattices in the unit cell, with four of them in each BP layer, labeled here by $A_i$, $B_i$, $C_i$, and $D_i$, with $i = 1, 2$ as layer index. Each layer can be seen as a combination of two linked sublayers, which are formed by the sublattices $A$ and $B$ ($C$ and $D$) at the bottom (top) sublayer, as represented in Figure 21(a). In this paper, we consider AB-stacked (Bernal) BL BP since this is the most energetically stable stacking configuration for multilayer BP according to first-principle calculations.[163]

Charge carriers in BL BP can be described by the tight-binding approach with Hamiltonian written[92] as

$$H = \sum_{m,i} U_i e^{\dagger}_{m,i} e_{m,i} + \sum_{m,i\neq j} t^{||}_{ij} \left( e^{\dagger}_{m,i} e_{m,j} + h.c. \right) + \sum_{i\neq j} t^{\perp}_{ij} \left( e^{\dagger}_{1,i} e_{2,i} + h.c. \right), \tag{3.1}$$

where $e^{\dagger}_{m,i}$ ($e_{m,i}$) with $e_{m,i} = \{a_{m,i}, b_{m,i}, c_{m,i}, d_{m,i}\}$ creates (annihilates) an electron in site $i$ of sublattice $\{A_{m,i}, B_{m,i}, C_{m,i}, D_{m,i}\}$, being $m = \{1, 2\}$ the layer index. $t^{||}_{ij}$ and $t^{\perp}_{ij}$ in the second and third terms of Eq. (3.1) correspond to the intralayer and interlayer hopping energies

Figure 21 – (a) Schematic representation of a BL phosphorene, indicating the hopping parameters assumed in this work and the sublattices: A and B at the bottom sublayer, and C and D at the top sublayer of each component layer of the BL. Intralayer (interlayer) hoppings are denoted by a $||$ ($\perp$) superscript index. (b) Illustration of the investigated gate-induced quantum confinement nanostructure defined in BL phosphorene. Panel (c) displays the cross-sections of the potential profile of the applied gated voltages to the upper ($U_{II}$) and lower ($U_I$) layers and the corresponding low-level band structures for pristine BL BP in the absence and in the presence of a perpendicularly applied electric field.

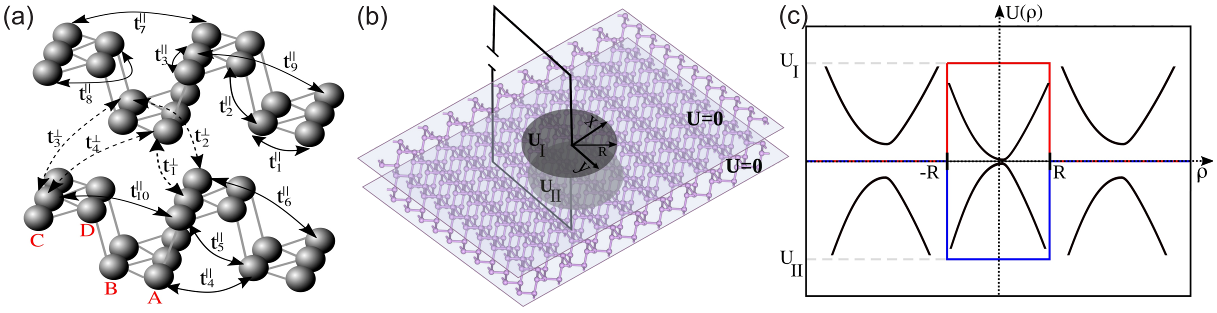

Source: Prepared by the author.

Table 4 – Intralayer ($t^{||}$) and interlayer ($t^{\perp}$) hopping parameters for BL BP.

| $t^{\vert\vert}$ | Value (eV) | $t^{\vert\vert}$ | Value (eV) | $t^{\perp}$ | Value (eV) |
|---|---|---|---|---|---|
| 1 | $-1.486$ | 6 | $0.186$ | 1 | $0.524$ |
| 2 | $3.729$ | 7 | $-0.063$ | 2 | $0.180$ |
| 3 | $-0.252$ | 8 | $0.101$ | 3 | $-0.123$ |
| 4 | $-0.071$ | 9 | $-0.042$ | 4 | $-0.168$ |
| 5 | $-0.019$ | 10 | $0.073$ | 5 | $0.000$ |

Source: RUDENKO, M. *et al.*, 2015 [92].

between sites $i$ and $j$ in the same or different layers, respectively. These summations run over $10$ intralayer and $5$ interlayer hoppings (see Figure 21), with hopping parameters given in Table 4 [92]. The first term on the right-hand side of Eq. (3.1) corresponds to the on-site potential energy. In order to incorporate the effect of a perpendicularly applied electric field to define the investigated quantum confinement BP structures, we take $U_i = U_I$ for the atoms in the bottom layer ($A_1$, $B_1$, $C_1$, $D_1$) and $U_i = U_{II}$ for the atoms in the upper layer ($A_2$, $B_2$, $C_2$, $D_2$). Thus, the electric field equally affects the on-site energies of all atoms in the two sublayers that form a certain layer $i$ by $U_i$. This assumption is based on the fact that the inter-sublayer distance is smaller than the interlayer one, expecting to have approximately the same (different) bias voltage for all four sublattices in the same (different) layer.

We consider the presence of a circularly symmetric and position-dependent potential, $U_{I,II} \equiv U_{I,II}(\mathbf{r})$, in order to investigate the behavior of the energy levels of the charge carriers that are electrostatically confined in a circular dot area of radius $R$, defining a QD in BL phosphorene, as sketched in Figures 21(b) and 21(c), with a sharp-edged circular potential such as rectangular profile

$$U_I(r) = -U_{II}(r) = \begin{cases} U, & \text{for } r < R \\ 0, & \text{for } r \geq R \end{cases} . \tag{3.2}$$

In such a low-dimensional quantum structure, finite potential values are assumed inside the dot region, *i.e.* electrons and holes are expected to be confined by a tunable potential barrier $U$, as illustrated by the cross-sections of the potential profile in Figure 21(c). Our circular choice for the shape of the BL BP QDs is motivated by the samples experimentally produced using a scanning tunneling microscope (STM) tip that creates exposed circular p-n junctions in 2D systems, such as reported in Refs. [105, 164] for BL graphene/hBN heterostructure and in Refs. [106, 104] for quasi-localized states in circular p-n junctions in monolayer graphene/hBN heterostructures. In both cases, QD states were imaged by employing this tip voltage pulsing technique. Moreover, the proposed quantum nanostructure here is feasible to be fabricated, as motivated by the state-of-the-art heterostructures based on black phosphorus with dual-gate applications reported in Ref. [165].

The effect of an external magnetic field is incorporated into the tight-binding Hamiltonian [Eq. (3.1)] by including a phase in the hopping parameters according to the Peierls substitution [166, 167], such as $t_{ij}^{||,\perp} \to t_{ij}^{||,\perp} \exp i\frac{2\pi}{\phi_0}\int_i^j \vec{A}\cdot d\vec{l}$, where $\vec{A}$ is the vector potential, and $\phi_0 = h/e$ is the magnetic quantum flux with $h$ being the Planck constant. In the presence of a perpendicularly applied magnetic field to the BL BP sample, $\vec{B} = B\hat{z}$, we conveniently choose the Landau gauge $\vec{A} = (0, Bx, 0)$, with $B$ being the magnetic-field amplitude.

The energy levels and the corresponding wave functions of the electrostatic defined BL BP QDs, discussed in the following sections, were obtained by diagonalizing the Hamiltonian (3.1) taking the electrostatic potential (3.2) for a large circular BL BP sample, assuming the flake with a radius given by the QD radius ($R$) plus an extra cutting off radius ($R_c$), *i.e.* $R + R_c$. Numerical tests taking different sample widths showed us that the value used here of $R_c \approx 10$ nm was more than appropriate.

## 3.3 Results

In order to understand how the proposed system works as a quantum confinement nanostructure defined in a BL phosphorene, let us first discuss the energetic band structure of an infinite BL phosphorene sheet in the presence of a perpendicularly applied electric field. For that, we show in Figure 22 the lowest-energy bands along the path $\vec{X} - \vec{\Gamma} - \vec{Y}$ obtained by diagonalizing the BL BP Hamiltonian (3.1) for three different values of a perpendicularly applied bias voltage $U$. The $x$ and $y$ directions correspond to the armchair and zigzag crystallographic lattice directions, respectively. Note that for the unbiased case [$U = 0$ - black solid curves in Figure 22(a)], pristine BL BP has an anisotropic band structure with a finite direct bandgap at $\vec{\Gamma}$–point, *i.e.*, it is characterized as a direct bandgap semiconductor. By analyzing the lowest four bands, one notices that the bandgap decreases when $U \neq 0$. This statement can be verified in Figure 22(b), which displays how the energy bands at the $\vec{\Gamma}$–point behave in the presence of a non-null bias. Red dashed curves in Figure 22(a) show the energy bands for the critical value $U_c$, *i.e.*, when the valence and conduction bands touch each other, and consequently, the gap is closed. The energetic position of the critical bias value can be found at the conduction-valence band crossing point in Figure 22(b), given by $U_c \approx 1.737$ eV. For gate voltage higher than the critical value ($U > U_c$), the electronic BP bands exhibit an inversion and, consequently, intersect at two points along the $\vec{X}$–direction, leading to the formation of Dirac-like cones away from the $\vec{\Gamma}$–point, such that the system's isoenergy at this bias stage for an electron doping at the conduction band around $E = 0$, *i.e.* energetically cutting the bands, shall resemble a ring-Dirac-like isoenergy in the $k_x$–$k_y$ plane [134, 135, 136, 137]. For even higher bias values, one observes a degeneracy breaking for one of two minicones, such that the isoenergy for $U > U_c$ looks like two peanuts along the $\vec{X}$–direction in the Brillouin zone, as demonstrated in Figure 3(c) in Ref. [135]. Such a situation corresponds to the blue dotted curves for $U = 3$ eV in Figure 22(a) for a 2D energetic plot of the bands. These effects of gap closing and band crossing have been reported experimentally [132, 133] and discussed theoretically [134, 135, 136, 137] in the literature, and as we shall demonstrate, they are the key ingredients for the proposed electrostatically defined quantum nanostructure here in BL BP.

Before analyzing the BL BP charge carrier energy levels for different system parameters of the investigated nanostructure, it is worth noting that according to Figure 22 and based on previous knowledge about other BL 2D semiconductors [119] and BL graphene [138, 139], the gap closing in BL BP under applied bias is very counterintuitive. It was to be expected that breaking the inversion symmetry in BL systems due to a perpendicular electric field would lead to the opening of a gap. However, the BL BP band structure exhibits the opposite and unexpected behavior with a gap closing. Such a feature enables us to confine charge carriers in the regions where the bias voltage is non-zero in BL BP systems, corresponding to regions with a lack of inversion symmetry. Thus, as follows, by applying the position-dependent bias potential, given by Eq. (3.2), we shall theoretically demonstrate that nanostructured QDs can be realized and also characterize the behavior of their lowest energy states. A schematic illustration of the proposed BL phosphorene quantum confinement nanostructure induced by external perpendicular electric fields is shown in Figure 21(b), and the corresponding potential profile is sketched in Figure 21(c).

Figure 22 – (a) Band structures for the lowest four energies of infinite BL BP subjected to different bias potential $U$ applied in the out-of-plane direction, where the atoms in the bottom (top) layer have on-site energies $-U/2$ $(U/2)$. Different gate potential values were taken: $U = 0$ (black solid curves), $U = 1.737$ eV (red dashed curves), and $U = 3$ eV (blue dotted curves). (b) The bias voltage effect on the BL BP band structure at the $\vec{\Gamma}$–point, depicting a critical value $U_c \approx 1.737$ eV associated with the bias-induced conduction-valence band crossing.

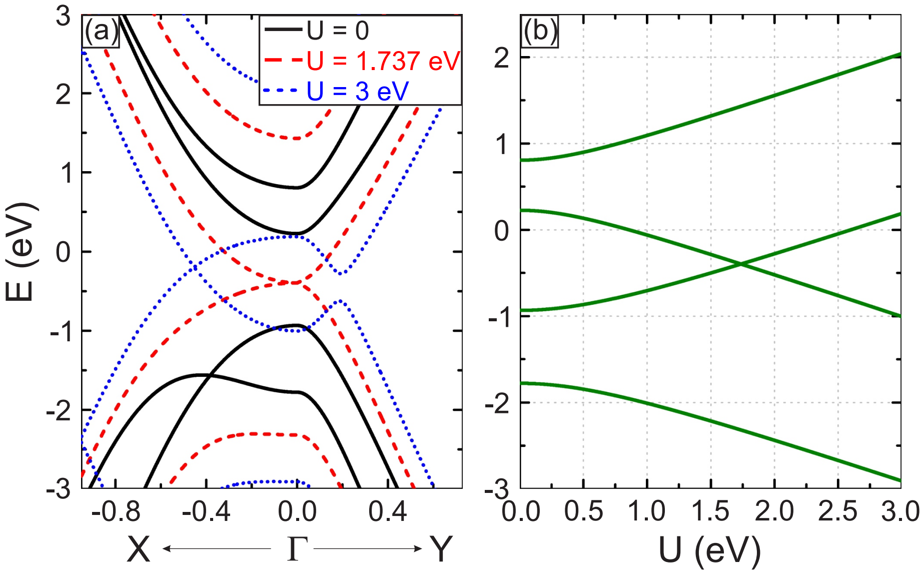

Source: Prepared by the author.

### 3.3.1 *In the absence of a magnetic field*

Figure 23(a) shows the energy levels of BL phosphorene QDs as a function of the QD radius $R$, for a fixed bias $U = U_c$ in Eq. (3.2). Before discussing the electrostatic-induced confined states in the BL BP QDs, it is worth highlighting the energetic range of continuous modes and the energy interval in which confined states are expected to exist. From the cross-section of the potential profile sketched in Figure 21(c) with the illustration of the corresponding lowest-level band structures for pristine BL BP in the absence (region for $r > R$) and the presence (region for $r \leq R$) of a perpendicularly applied electric field, and the depicted band structures in Figure 22 for $U = 0$ (black solid curves) and $U = U_c$ (red dashed curves), one expects to obtain discretized energy levels originating from the confined states in the BL BP QD system within the interval given by $-0.94$ eV $\gtrapprox E \lessapprox 0.24$ eV. This can be checked by the alignments of the bottoms (tops) of the conduction (valence) bands in the semiconductor (region for $r > R$) and metallic regions (region for $r \leq R$), whose band alignment cross-section can be viewed as a finite quantum well for electron (hole) particles. On the other hand, for $E \gtrapprox 0.24$ eV and $E \lessapprox -0.94$ eV, any energy value is allowed, forming, therefore, a continuum of states since there is no energetic restriction to the charge carriers' mobility, as can be con-

Figure 23 – Energy levels of BL phosphorene QDs as a function of (a) the QD radius $R$ for a fixed bias $U = U_c$. Red dashed lines at $E = -0.24$ eV and $E = 0.94$ eV delimitate the confinement and continuum energetic regions for the nanostructured 2D system. (b) Energy gap $E_g(R) = E_{e_1}(R) - E_{h_1}(R)$ as a function of the QR radius. Panel (c) shows a zoom-in of the region denoted by a yellow shaded rectangle in panel (a), emphasizing the trend of the first seven electron ($e_i$) and first seven hole ($h_i$) energy levels ($i = \{1, 2, \ldots, 6, 7\}$). Symbols correspond to the tight-binding data like those in panel (a), and solid curves are the fitting curves for each energy level. The colormap is associated with the slope $\alpha$ of the fitting power-law curves, given by $\propto 1/R^{\alpha}$.

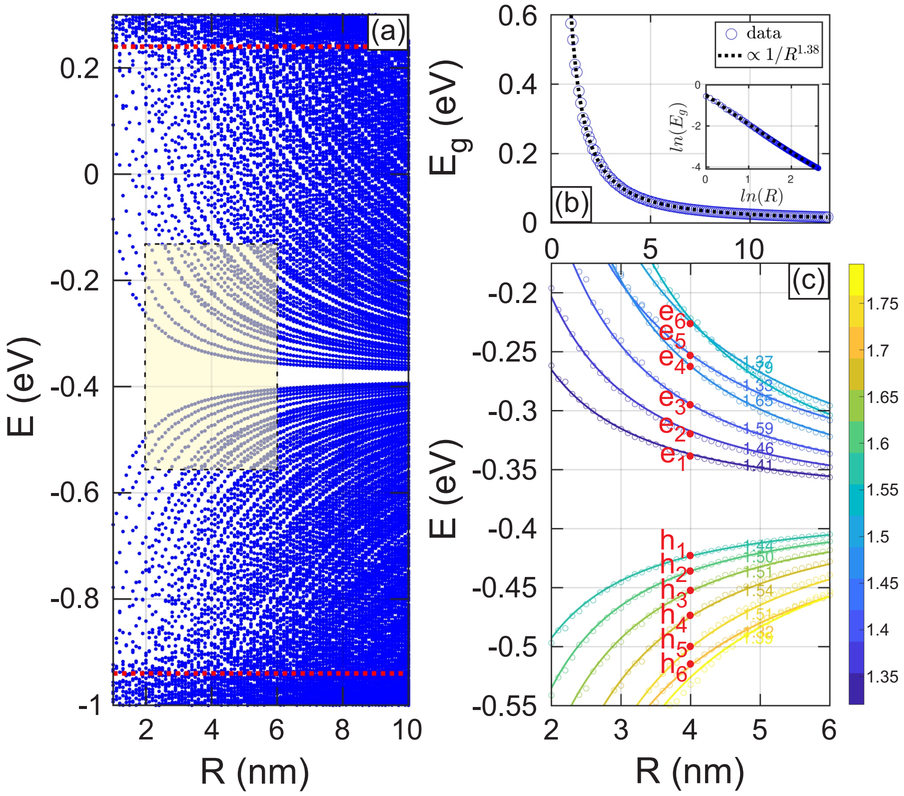

Source: Prepared by the author.

firmed by the region delimited by the red dashed lines in Figure 23(a), presenting a continuum of states beyond the red dashed lines.

From the semiconductor physics of quantum confinement systems, it is well-known that as one increases the confinement system size, the energy levels exhibit a decay tendency, bringing the energy states increasingly closer to each other, which in turn leads to a larger number of allowed states for a fixed energy range [96, 97, 98, 99, 100, 101]. Similarly, this is exactly what is observed in Figure 23(a) for energy levels as a function of $R$ for electrostatic-defined BL BP QDs in the $-0.94$ eV $\lessapprox E \lessapprox 0.24$ eV range. Concerning the size-dependent energy gap of BP QDs, we show in Figure 23(b), in blue symbols, the energy gap calculated by the energetic difference between the first electron [$E_{e_1}(R)$] and the first hole [$E_{h_1}(R)$] states at each $R$ value computed from the tight-binding spectrum of Figure 23(a), *i.e.*, $E_g(R) = E_{e_1}(R) - E_{h_1}(R)$. The black dashed curve corresponds to the fitting power-law curve, such as $E_g(R) \propto 1/R^{1.38}$. The log-log-scale plot shown in the inset of Figure 23(b) for the $ln(E_g) \times ln(R)$ tendency emphasizes such negative slope of the linear log-log-curve, with a magnitude of the slope clearly not being $1$ and also less than $2$. Reference [145] also demonstrated a result that deviates from the traditional trend of $\sim 1/R^2$ for standard semiconductors with isotropic parabolic band structure, such as QD defined in isotropic 2D electron gas systems. J. S. de Sousa *et al.* [145] showed that the single-particle band gap of isolated circular cut-out BP QDs can be fitted with the following power-law $E_g(R) = E_g^{\text{bulk}} + c/R^{\alpha}$, with $c$ being a fitting constant and $\alpha = 1.41$. Note that the power-law $\alpha = 1.41$ obtained in Ref. [145] for cut-out BP QDs deviates solely slightly from that obtained here, *i.e.* $\alpha = 1.38$, for the electrostatically defined BP QDs, showing that both circular cut-out BP QDs and electrostatically defined BP QDs exhibit a similar qualitative trend for the energy gap as a function of the BP QDs radius, which reflects the anisotropic character of the system regardless of the boundary condition assumed to define the quantum confinement nanostructure in BP.

In addition to that, owing to the highly anisotropic nature of the multilayer phosphorene band structures, exhibiting anisotropic effective masses for electrons and holes as well as along $x$ and $y$ directions [27, 92, 93, 95], one also obtains here, as shown in Figure 23(a), slightly different size-dependent single-particle energy trends for the lowest-energetic electron and hole states as the QD radius increases. In order to verify this, we show in Figure 23(c) the fitting curves for the first seven electron ($e_i$) and first seven hole ($h_i$) states ($i = \{1, 2, \ldots, 6, 7\}$), in which the color scale of each curve is associated with the slope $\alpha$ of the fitting power-law dependencies $E_{e_i,h_i} \sim 1/R^{\alpha}$. The fitting slopes for the first seven electron states are: $E_{e_1} \sim 1/R^{1.41}$, $E_{e_2} \sim 1/R^{1.46}$, $E_{e_3} \sim 1/R^{1.59}$, $E_{e_4} \sim 1/R^{1.65}$, $E_{e_5} \sim 1/R^{1.33}$, $E_{e_6} \sim 1/R^{1.79}$, and $E_{e_7} \sim 1/R^{1.37}$, whereas the ones for hole states are: $E_{h_1} \sim 1/R^{1.44}$, $E_{h_2} \sim 1/R^{1.50}$, $E_{h_3} \sim 1/R^{1.51}$, $E_{h_4} \sim 1/R^{1.54}$, $E_{h_5} \sim 1/R^{1.51}$, $E_{h_6} \sim 1/R^{1.32}$, and $E_{h_7} \sim 1/R^{1.39}$. Note that it demonstrates an intermediate character of the $\alpha$ value, being between 1 and 2 as should be expected for isotropic systems with linear and parabolic dispersion relations in reciprocal space, respectively. This is also in contrast with the results obtained for BL graphene QDs in the absence of the trigonal warping effect, in which the lowest-energy states present an $\sim 1/R^2$ dependency due to the BL graphene quadratic dispersion relation, as demonstrated in Refs. [168, 107, 108, 109, 110, 114] for different geometries of QDs defined in BL graphene. Beyond the lack of electron-hole symmetry demonstrated here by the different electron-hole size-dependent tendencies of the lowest-energy levels, one clearly observes in Figures 23(a) and 23(c) that the electron or hole energy levels are not equally spaced because they do not have the same slopes. For instance, note that the seventh ($e_7$) electron energy state crosses the sixth ($e_6$) electron energy state around $R \approx 4.2$ nm, as well as the fifth ($e_5$) electron energy state crosses the fourth ($e_4$) electron energy state around $R \approx 3.3$ nm. This is a consequence of the different $\alpha$ values for the $1/R^{\alpha}$ tendencies for each confined QD state in the anisotropic BP sample. Otherwise, the energy states would never intersect. Further on, we shall discuss the cause/consequence of such a fact of the different slopes for the energy levels on the wave function distribution.

Aiming to confirm that the energy levels in the energetic region $-0.94$ eV $\lessapprox E \lessapprox$ $0.24$ eV correspond to confined states, we show in Figure 24 the first six lowest-energy electrons ($e_i$) and holes ($h_i$) probability densities for a BL BP QD with a fixed radius of $R = 4$ nm, as marked by red symbols in Figure 23(c). Note that the spatial distributions of these probability densities are mainly localized at the central part of QD, *i.e.*, inside the black circle that limits the non-zero circularly defined bias region; thus, confirming the confined character of these states. This spatial distribution's behavior of the probability densities is similar to the ones observed for electrostatically defined monolayer BP QDs [151] and bulk states in circular [145, 146], rectangular [157, 158, 160], and triangular [159, 162] cut-out defined multilayer BP QD nanostructures. Here, one does not observe edge states, conversely to what is observed in well-defined BP QD structures with zigzag edges [157, 158, 160, 159, 162, 153] or even for the case of not perfectly circular cut-out BP QDs [145, 146] that have mixed zigzag and armchair edges, being such states mainly distributed along the zigzag boundaries. This is due to the origin of the confinement not being structural here but rather electrostatic, such that the type of atomic boundary contour of the electrostatic potential edges does not significantly affect the quantum confinement electronic spectrum, resembling those confined states in 2D systems in which the infinite-mass boundary condition was imposed to prevent edge states, as reported in Refs. [169, 90, 112] for monolayer and in Refs. [169, 168, 109, 114] for bilayer graphene QDs and QRs.

Analyzing the probability densities in Figure 24, one notices that the confined states exhibit an increasing number of nodes, which is compatible with 2D quantum confinement nanostructures. [99, 101, 100, 98, 96, 97] However, contrary to what is observed for isotropic semiconductors with a monotonic increase in the number of nodes in their wave functions for higher energetic states, here due to the anisotropic effective masses in both conduction and valence bands, one observes a discontinuity in the monotonic increasing number of nodes when taking more energetic states. This fact is evident for the $5$th electron state ($e_5$) and the $6$th hole state ($h_6$) in Figure 24, in which it would be expected to exhibit five peaks for the $e_5$ state and six peaks for the $h_6$ state, but on the other hand, it has only two and four peaks oriented along the horizontal ($x$) axis, respectively. As a consequence of the fact that the effective masses of electrons and holes in the zigzag ($y$) direction are larger than the ones in the armchair ($x$)

Figure 24 – The total probability densities for the twelve electronic states marked by the red symbols in Figure 23(c), corresponding to the first six ($i = \{1, 2, ..., 6\}$) electron-states ($e_i$) and hole-states ($h_i$) of a BL BP QD with radius $R = 4$ nm. The black circle indicates the limit of non-null bias potential $U = U_c$ for $r \leq R$, as illustrated in Figure 22(b). Low and high intensities for the probability densities are denoted by white and dark blue colors, respectively. The large gray area corresponds to the BL BP sample.

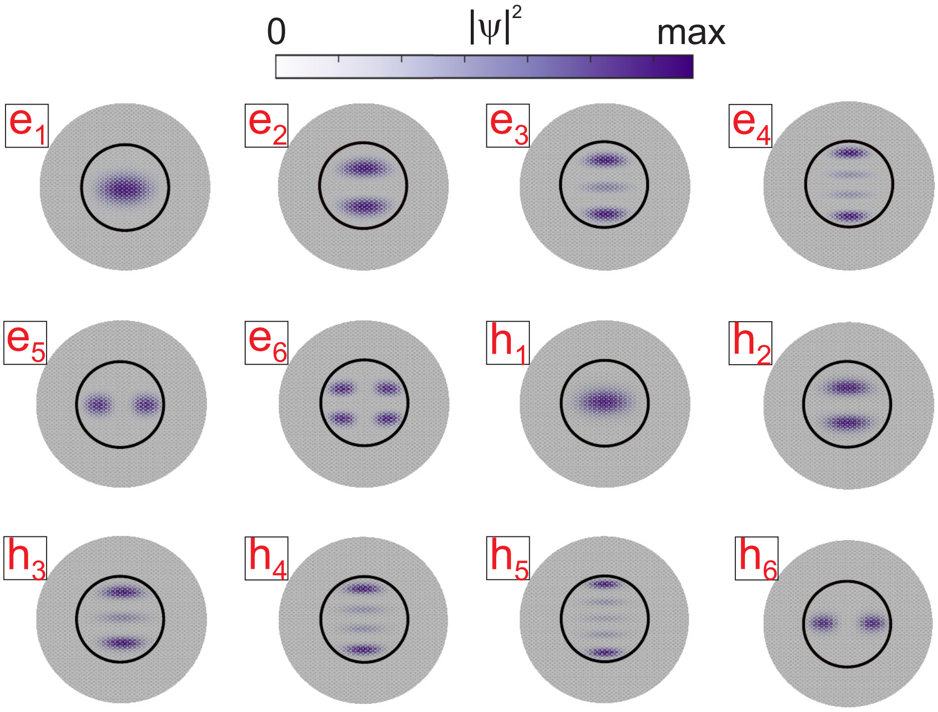

Source: Prepared by the author.

direction and, therefore, the lowest kinetic energy contribution of the confined particle, which is inversely proportional to their effective masses, are along $y$ direction, one has the preferential localization of the wave functions are vertically aligned ($y$ direction), as observed for the vast majority of states in Figure 24. Therefore, for the $e_5$ and $h_6$ states, the spatial distribution of the squared wave function is more favorable to be aligned horizontally with a smaller number of peaks than vertically with the expected five and six peaks for $e_5$ and $h_6$, respectively. A similar result was reported in Ref. [145] for a 10 nm monolayer BP QD in which the electronic state $e_4$ exhibited two peaks aligned along the lower effective masses direction instead of the expected four peaks nodal profile for the spatial distribution of the wave function aligned along the higher effective masses direction.

A more careful analysis of the energy levels for the first five electronic states ($e_1$ to $e_5$) in Figures 23(a) and 23(c) reveals that the slope of the fifth electron state ($e_5$) differs pronouncedly from the other four lowest electron states ($e_1, e_2, e_3, e_4$). By fitting the 5th electron state, one obtains a tendency that decays with approximately $E_{e_5} \propto R^{-1.33}$, *i.e.* with an exponent that is closer to $1$ than to $2$, whereas the other ones $E_{e_1,e_2,e_3,e_4}$ follow an approximately trend in which the slope is greater than the one for $E_{e_5}$. Such $\sim 1/R^{\alpha}$ size-dependent behavior of the energy levels is consistent with the expected confinement tendency of Schrödinger-like and Dirac-like particles when $\alpha$ is closer to $\sim 2$ and $\sim 1$, respectively, due to parabolic and linear shapes of the material dispersion relations. For phosphorene-based systems, it is observed that both dispersions, as can be seen from the band structure of the BL BP along $\vec{\Gamma}$–$\vec{Y}$ and $\vec{\Gamma}$–$\vec{X}$ directions in Figure 22(a), in which one observes a linear ($\sim k$) and a quadratic ($\sim k^2$) energy-momentum shape, respectively. Therefore, the preferential localization of the wave functions of the confined states for BL BP is in agreement with their expected nature based on the band structure of anisotropic materials that present both linear and quadratic energy-momentum formats, their effective masses and kinetic energy contributions, and consequently, their behaviors as Schrödinger-like or Dirac-like particles. Therefore, roughly speaking, one can state that the first four electron states ($e_1, e_2, e_3, e_4$) behave as Dirac-like electrons, due to the confinement direction of their squared wave function's distribution along the $y$-direction, the slopes of their power-law tendencies that have an exponent closer to $1$, and their origin being associated with the linear dispersion relation from the bulk BP case; in contrast, the fifth electron state ($e_5$) behaves as a Schrödinger-like electron, exhibiting confinement along the $x$-direction which posses a quadratic energy-momentum dispersion relation in the bulk BP case, as well its power-law tendency that has an exponent much greater than $1.4$. Other energy crossings in Figures 23(a) and 23(c) reveal similar behavior for these other higher energy states for electrons and holes, exhibiting preferential exchanges along the directions with lower and higher effective masses of the system, as for instance, the $e_6$ and $e_7$ states at $R \approx 4.2$ nm and $h_7$ and $h_8$ states at $R \approx 3$ nm [see Figure 23(c)].

Keeping in mind that the charge carrier confinement is induced here by an externally applied gate voltage perpendicular to the BL phosphorene sample [Figures 21(b) and 21(c)], it is relevant to investigate the role played by the bias amplitude $U$ to the energy spectrum of the nanostructured system, such as the number of discretized energy levels and the energetic range in which such confined states emerges when one tunes $U$, and what happens in the energy spectrum when $U > U_c$. For that, we show in Figure 25(a) the energy levels as a function of the bias voltage $U$ for a fixed BL BP QD radius with $R = 4$ nm. To guide the eyes by delimiting the allowed energetic region where confined states arise, *i.e.*, which results in states with localized wave functions inside the QD, we also show in Figure 25(a) two red dashed curves at $E = -0.94$ eV and $E = 0.24$ eV, separating the confined states from the region with a continuum of allowed states, and two green dashed curves ($E_c$ and $E_v$), corresponding to the two-lowest energy bands at the $\vec{\Gamma}$–point for the BL BP with uniform bias $U$, *i.e.* the two energy levels closest to the Fermi energy similarly the two energetic lowest green ones

Figure 25 – (a) Energy levels of BL phosphorene QDs as a function of the bias voltage $U$ for a fixed QD radius $R = 4$ nm. Dashed red lines indicate the limit of the energetic continuum region delimited by the $-0.94$ eV $\lessapprox E \lessapprox 0.24$ eV range. The green dashed curves correspond to the two lowest pristine BL BP energy bands as depicted in Figure 22(b), labeled as $E_c$ and $E_v$ and analytically given in Eqs. (A.1a) and (A.1b), respectively. Four different regions are labeled in the energy spectrum: (I) $E_v \leq E \leq E_c$ and $U \leq U_c$, (II) $E_c \leq E \leq 0.24$ eV for $U \leq U_c$ and $E_v \leq E \leq 0.24$ eV for $U > U_c$, (III) $E_c \leq E \leq E_v$ and $U > U_c$, and (IV) $-0.94$ eV $\leq E \leq E_v$ for $U \leq U_c$ and $-0.94$ eV $\leq E \leq E_c$ for $U > U_c$. The yellow shaded area in (a) is zoomed in Figure 26(a). (b) Energy gap as a function of the bias voltage $U$ for a fixed QR radius $R = 4$ nm, computed as $E_g(U) = E_{e_1}(U) - E_{h_1}(U)$. The yellow shaded region in (b) represents the $U$ region in which no confined states in the energetically allowed region were obtained in the BL BP QD with $R = 4$ nm.

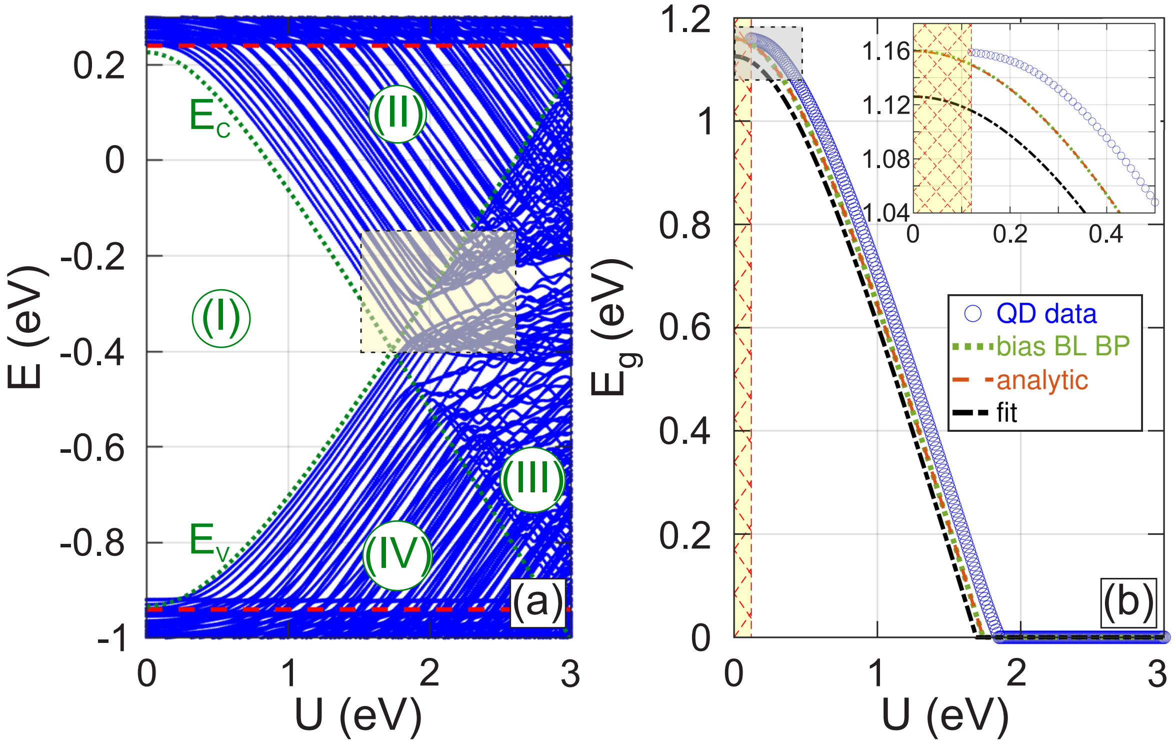

Source: Prepared by the author.

depicted in Figure 22(b). The analytical expressions for such conduction [$E_c \equiv E_c(\Gamma, U)$] and valence [$E_v \equiv E_v(\Gamma, U)$] energy states are given in the Appendix, presenting a square-root bias-dependence, as depicted in Eqs. (A.1a) and (A.1b). These states split the energy spectrum of Figure 25(a) into four different regions, indicated by:

(I) $E_v(\Gamma, U) \leq E \leq E_c(\Gamma, U)$ and $U \leq U_c$: No energy state is found in this region since this energetic range corresponds to the band gap region of biased pristine BL BP.

(II) $E_c(\Gamma, U) \leq E \leq 0.24$ eV for $U \leq U_c$ and $E_v(\Gamma, U) \leq E \leq 0.24$ eV for $U > U_c$: Confined states emerge from the continuum when a non-null bias is induced in the sample.

Figure 26 – (a) Zoom-in of the energy spectrum denoted by the yellow region in Figure 25(a) for a $R = 4$ nm BL BP QD as a function of the bias voltage $U$. (b) The total probability densities for the twelve states marked by the red circles are shown. Low and high intensities for the probability densities are denoted by white and dark blue colors, respectively. The large gray area corresponds to the BL BP sample.

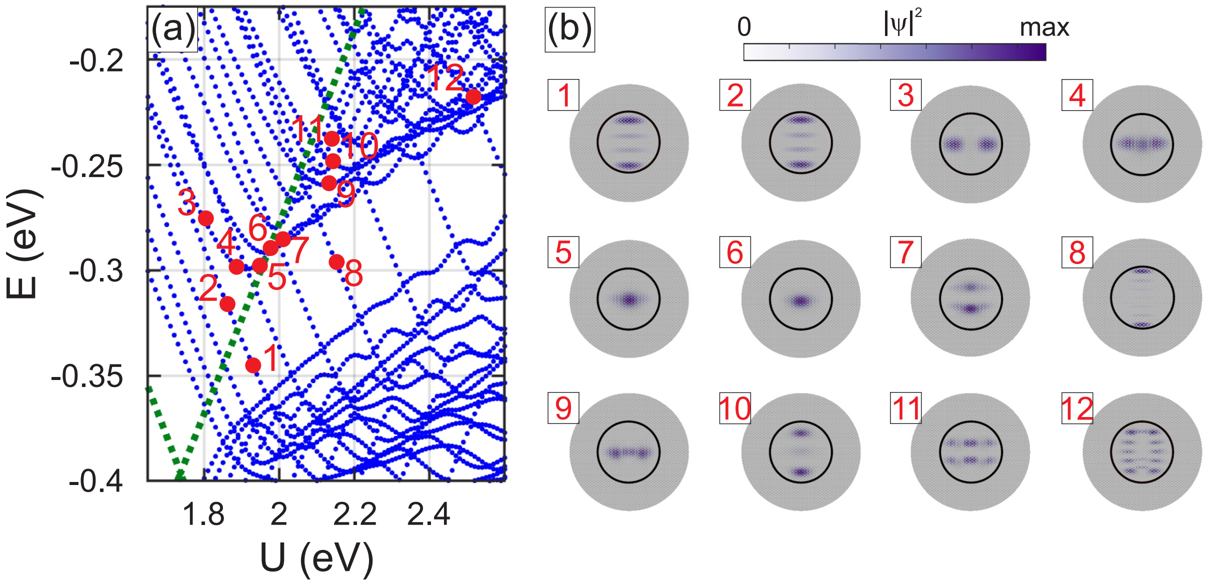

Source: Prepared by the author.

By increasing $U$ and consequently reducing the energy gap of the system in the region $r < R$, which leads to the emergence of a circularly symmetric potential well caused by the band alignment between the $r < R$ and $r \leq R$ regions, allowed energy states are raised up, as discussed in Figure 23(a) for the states delimited between the two red dashed lines in the range $-0.94$ eV $\lessapprox E \lessapprox 0.24$ eV. One notices that the energy levels in Region II in Figure 25(a) roughly square-root decay as a function of the bias gate $U$. This trend is in full agreement with the analytically expected expression [see Eq. (A.1a) in the Appendix] for electron states that dictate the behavior of the bulk $E_c$ biased BL BP bands, which, as noted by the green curve, also exhibits such behavior. Moreover, the $E \times U$ square-root behavior can be intuitively justified by making an analogy between the biased BL BP system and an anisotropic coupled double-layer 2D electron gas system. [170] Within an effective mass approximation, one can write down a coupled biased double-layer system composed of two identical anisotropic semiconductors by the following $2 \times 2$ matrix

$$H_m = \begin{pmatrix} H_{\text{mono}}(k_x, k_y) + U_1 & \Delta \\ \Delta & H_{\text{mono}}(k_x, k_y) + U_2 \end{pmatrix}, \tag{3.3}$$

where it was assumed a constant interlayer coupling $\Delta$ and $H_{\text{mono}}$ being associated with the electron dynamics in each BP layer. By diagonalizing Eq. (3.3), one obtains $E_\pm = \hbar^2 k_x^2/2m_x + \hbar^2 k_y^2/2m_y + (U_I + U_{II})/2 \pm \sqrt{(U_I - U_{II})^2/4 + \Delta^2}$, where $m_x$ and $m_y$ are the effective masses along $x$ and $y$ directions, respectively, and thus, $\hbar^2 k_x^2/2m_x + \hbar^2 k_y^2/2m_y$ is the kinetic energy term of $H_{mono}$. From Eq. (3.2), it was assumed $U_I = -U_{II} = U$ for the bias voltage, leading to the following energy difference, corresponding to the energy gap, $|E_+ - E_-| = 2\sqrt{U^2 + \Delta^2}$. By this simply effective mass picture, one can easily observe that the energy square-root scales with the bias gate $U$, similarly to the observed tendency of the confined states in Region II in Figure 25(a). On the other hand, such simplified modeling does not capture the negative slope of the square-root tendency of the biased BL BP energy gap, which is described properly by Eq. (A.1a) for electron states.

(III) $E_c(\Gamma, U) \leq E \leq E_v(\Gamma, U)$ and $U > U_c$: As discussed concerning Figure 22, after the gap closing point, there is a band inversion with two crossing points in the Brillouin zone. For larger $U$ magnitudes, one of these crossing points between the valence and conduction bands lifts its degeneracy [see blue dotted curves in Figure 22(a)]. This leads to the emergence of several crossings and anti-crossings in the energy spectrum of the BL BP QD in Region III of Figure 25(a).

(IV) $-0.94 \leq E \leq E_v(\Gamma, U)$ for $U \leq U_c$ and $-0.94 \leq E \leq E_c(\Gamma, U)$ for $U > U_c$: States in Region IV in Figure 25(a) are analogous to those of Region II, but now hole states scale similarly as $E_v(\Gamma, U)$ given by Eq. (A.1b).

Similarly to the well-behaved states in Regions II and IV, in which the energy states exhibit a square-root tendency, the energy gap of the BL phosphorene QD system also presents a $\propto \sqrt{U^2 + \text{constant}}$–like trend, as observed in Figure 25(b). To verify that, we compare the calculated energy gap obtained from the tight-binding BL BP QD data $E_g(U) = E_{e_1}(U) - E_{h_1}(U)$ (blue symbols) with the energetic difference between the lowest two energies ($E_c$ and $E_v$) of the infinite BL BP subjected to different bias potential $U$ computed by means of the tight-binding approach (green curve), as in Figure 22(b), also by analytical expressions for $E_c(\Gamma, U)$ and $E_v(\Gamma, U)$ given in the Appendix in Eq. (A.3) (orange curve), and by a fitting curve (black curve), given by $E_g(U) \propto 1.8399 - 1.1346\sqrt{0.7520U^2 + 0.5997^2}$ (in eV). All curves in Figure 25(b), whether they come from the analytical or fit expression, give a similar behavior as that of the tight-binding calculated BL BP QD data, confirming the nature of its square-root bias-dependent energy gap. Due to the different approaches adopted here to compare with the BL BP QD data, slightly different energy gaps for the unbiased case were obtained, as discussed in the Appendix and as highlighted in the inset of Figure 25(b).

Let us now compare the spatial distribution of the probability densities of the states energetically located in the well-behaved square-root energy region [Region II] and the energetically complex Region III of Figure 25(a), in order to differentiate the confinement pattern when $U > U_C$ or $U < U_C$. The yellow shaded region of the energy spectrum of Figure 25(a) is magnified in Figure 26(a) close to the $U_C$ point, showing twelve states marked with red symbols. States $1$ and $2$ in Figure 26 correspond to the state $e_4$ in Figure 24, whereas the state $3$ in Figure 26 corresponds to the state $e_5$ in Figure 24, demonstrating that, indeed, such states in Region II are confined states, being thus located inside the QD region and with a well-behaved nodal pattern.

Although one can not find an uniform trend for the energies of states in Region III as a function of $U$, all states labeled from $4$ to $12$ are confined states, as presented in Figure 26(b), and as one should be expected, since they have energy in the $-0.94$ eV $\lessapprox E \lessapprox 0.24$ eV range for cases in which one takes non-zero bias to define the electrostatic BL BP QD. Moreover, we can observe, in Figure 25(a) and in the zoom of the energy spectrum in Figure 26(a) concerning Regions II and III, that there is a set of energy states in Region II with a decreasing energy trend as a function of $U$ that enter into Region III and exhibit a clear well-defined nodal behavior with their probability densities preferentially localized along the higher effective mass direction ($y$ direction), for instance states $1$ and $8$ in Figure 26. However, there is a set of energy states that, when entering Region III, exhibit an oscillatory behavior. As examples, one observes the spatial distribution of the probability density of the state $3$, which evolves to higher $U$ values for states $4$ and $5$, as well as state $6$, which evolves to state $7$. Note that there is a tendency for states that originate in Region II from those states with probability distributions located along the $x$ direction, *i.e.* aligned along the lower effective mass direction, to oscillate upon entering Region III. From the set of states $\{3, 4, \text{ and } 5\}$, $\{6 \text{ and } 7\}$, and $\{9, 10, 11, \text{ and } 12\}$, it is clear that such oscillating states present their probability density distributions less strongly localized along preferential directions, such as only $x$ or $y$ directions, but rather, they are more delocalized states with probability distribution more spread out in the QD. This results from the complex band alignment of the BL BP QDs electrostatically formed for bias amplitudes greater than $U_C$.

### *3.3.2 Magnetic field effects on the BL BP QD*

An important physical aspect to be explored is the system's response to external magnetic fields. In this context and in addition to the bibliographic survey done in the introduction (Sec. 3.1) concerning BP quantum confinement systems, we point out Refs. [143, 148, 160, 157, 151, 158] that have investigated the effects of the magnetic field on the energy spectrum of the phosphorene-based QD system. For instance, Zhang *et al.*[143] studied the magneto-optical properties of rectangular, hexagonal, and triangular monolayer

Figure 27 – Energy levels of a BL phosphorene QD as a function of magnetic flux $\Phi_R/\Phi_0$ through the QD (in units of the elemental quantum flux $\Phi_0$ and with $\Phi_R = \pi R^2 B$), taking the bias amplitude of (a) $U = U_C = 1.737$ eV and (b) $U = 3.0$ eV $> U_C$ in the region $r < R$ that defines the electrostatic QD, as sketched in Figures 21(b) and 21(c). It was assumed a dot radius of $R = 4$ nm. (c) Energy spectrum zoomed in on the panel (b) shown in the yellow shaded region, emphasizing the oscillatory states. (d) The probability densities for the states marked by red symbols 1 in panel (a) for the quantum Hall state at $\Phi_R/\Phi_0 \approx 47.4$ and $E_1 \approx 0.208$ eV, and (d) 2, 3, and 4 in panel (c) for the oscillatory states at $\Phi/\Phi_0 \approx 48.6$ and energies $E_2 \approx -0.314$ eV, $E_3 \approx -0.284$ eV, and $E_4 \approx -0.271$ eV, respectively. Low and high intensities for the probability densities are denoted by white and dark blue colors, respectively. The large gray area corresponds to the BL BP sample. The black circles in (d) denote the QD contour at $r = R$.

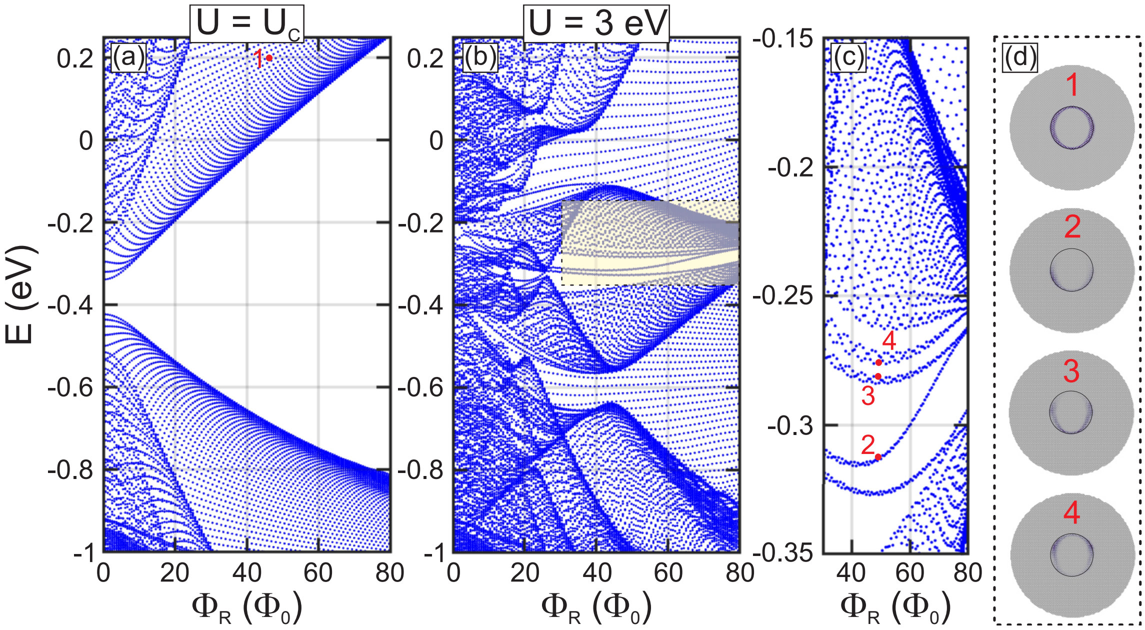

Source: Prepared by the author.

phosphorene QDs and demonstrated that their magnetic levels exhibit a Hofstadter-butterfly spectrum and approach the Landau levels of monolayer BP sheet as the magnetic field amplitude increases. The magnetic-field dependencies on the biased energy spectrum of rectangular monolayer phosphorene QDs were also investigated by Li *et al.*[148], theoretically observing that the edge and bulk states have different responses to the electric and magnetic fields, leading to distinct electric- and magnetic-field dependencies on their energy spectra, with the bulk states being more affected by the magnetic field while the edge states are more influenced by the electric field. Li *et al.* also extended their investigations in a similar study in Ref. [157] for the BL BP rectangular QD case. Similar to the work of Li *et al.*[157], Zare *et al.*[158] also investigated, using the tight-binding approach, the electronic and magneto-optical properties of rectangular BL phosphorene QDs in the presence of perpendicular electric and magnetic fields. They demonstrated that their magneto-energy spectra exhibit Aharonov–Bohm oscillations, with the period and the amplitude of the oscillation decreasing with the size of the QDs. Wang *et al.*[160] also compared the electronic properties of rectangular monolayer phosphorene QDs and quantum rings including the coulomb interaction using the Hubbard method, showing the spin-up and spin-down responses on the magnetic spectra of such quantum confinement BP systems when B-field is applied. B. Szafran [151] studied the confined states in a parabolic single-band effective-mass modeling in monolayer phosphorene, including the effects of the external magnetic field and the electron-electron interaction. None of them explored the magnetic field effect on the BL phosphorene QDs electrostatically defined as proposed here.

In this regard, we show in Figs. 27(a) and 27(b) the energy levels of $4$ nm BL BP QD as a function of the magnetic flux $\Phi_R/\Phi_0$ for two different bias potential energies applied in the circularly symmetric $r < R$ region: (a) $U = U_C = 1.737$ eV and (b) $U = 3$ eV. $\Phi_R = \pi R^2 B$ is the magnetic flux through the QD and $\Phi_0$ is the quantum magnetic flux. A similar energy spectrum to Figure 27(a) under an applied $B$ field was also obtained for cut-out rectangular BL BP QDs in Ref. [157], except that (i) here no edge state is present, since the BL BP QDs here are electrostatically defined, and (ii) the gapped energy spectra has a lower energy gap here even for $B = 0$ (compare Figure 27(a) of the current work with Figure 6(a) of Ref. [157]). Although Refs. [143, 148, 160, 157, 151, 158] studied the effects of the magnetic field on the energy spectrum of BP-based QDs, none of them presented how the spatial distribution of the probability densities associated with quantum hall states. For instance, Wang *et al.*[160] and Li *et al.*[157] showed the probability densities of the electronic states associated with the first Landau level, presenting, therefore, a spatial distribution with a center peak in the rectangular cut-out defined BP QD in monolayer and in BL cases, respectively. Concerning that, one can see state $1$ in Figure 27(d) that the quantum Hall states – the group of states with decreasing energy approaching the first Landau level – exhibit a ring-like spatial distribution, being preferentially located close to the circular boundary of the non-zero electrostatic potential at $r \approx R$.

By increasing the bias potential energy to $U = 3$ eV $> U_C$, a more complex energy spectrum is obtained, as shown in Figure 27(b). In the bulk BL BP case, as discussed at the beginning of Sec. 3.3 and shown in Figure 22(a), for $U > U_C$, one has an inverted band gap at the $\vec{\Gamma}$–point and a Dirac-like semimetal phase for the biased BL BP. As observed in Figure 25(a) and 26(a), for $U > U_C$, some energy levels, in the energetic region in which one has confined states, present an oscillatory behavior as a function of the bias $U$. In the cut-out BL BP QD case (see Figures 6(b) and 6(c) in Ref. [157]), the application of the perpendicular electric field results in the breaking of the edge state's subbands into four subgroups of states that merge into the biased bulk spectrum the higher is the applied bias voltage, whereas one has the clear existence of two groups of biased bulk Landau levels with distinctive electronic distributions over the two layers. Here, the energy spectrum is energetically more complex around the Fermi level than in Li's work under a non-zero bias. Moreover, here, Figure 27(b) also shows oscillations on the low-energy electronic states around $E \approx -0.3$ eV as a function of the magnetic field, as emphasized in the magnified spectrum in Figure 27(c) of the yellow shaded region of Figure 27(b). To understand the nature of such oscillatory states, we depict in Figure 27(d) the probability densities of the states 2, 3, and 4 at $\Phi_R/\Phi_0 \approx 48.6$, marked by red symbols in Figure 27(c). By analyzing their probability densities that exhibit delocalized distributions in the QD area close to the potential's interfacial contour, one notices that these energetic oscillations of these groups of two energy states seems to be Aharonov-Bohm oscillations, although we are dealing with a QD structure rather than a quantum ring, which would be to the natural quantum confinement structure to host Aharonov-Bohm oscillations. Aharonov-Bohm oscillations were obtained by Zare *et al.* [158] for rectangular BL phosphorene QDs. Therefore, in summary, by comparing Figures 27(a) and 27(b), it can be seen that the application of the magnetic field presents quite distinct responses in the energy spectrum of the electrostatically defined BL BP QDs depending on whether they are formed by a bias value greater or less than the critical value $U_C$; however, in both cases, the energy states within the energetic range $E \in [-0.94\text{ eV}, 0.24\text{ eV}]$ are still confined states.

## 3.4 Conclusions

In summary, by exploring the electronic properties of the BL phosphorene system, we have demonstrated that patterned bias gates can be used to confine charge carriers into this. Essentially, the current investigation is based on the tunability of the BL BP bandgap under the presence of a perpendicular electric field, which, in turn, exhibits a gap closing as the electric field amplitude increases [132, 133, 134, 135, 136, 137]. Therefore, by assuming a circularly symmetric perpendicularly applied electrostatic field, we showed that BL phosphorene QDs can be realized. Unlike other 2D materials, such as BL graphene [138, 139], the charge carriers in BL BP are localized in the regions in which the bias voltage is non-zero. For this purpose, we employed a tight-binding approach [92, 93] and presented results for the low-energy levels and probability densities for these confinement systems as a function of different system parameters, such as QD radius and bias voltage. Moreover, we verified how a perpendicular magnetic field may affect the confined states and the role played by the anisotropy in the low-energy states.

From a practical point of view, it is more efficient to adjust the physical properties of quantum confinement 2D materials-based systems by the application of external fields than by lithographically cutting off geometries, since in the former, there is no need to control edge type. In this perspective, we believe that the current work demonstrates a feasible method for controlling charge confinement, paving the way for future investigations on quantum confinement devices based solely on the bias voltage applied in anisotropic 2D materials.

# 4 CONCLUSIONS AND PERSPECTIVES

This thesis presented a theoretical investigation of the electronic properties of monolayer and bilayer phosphorene, with particular emphasis on the formation and manipulation of quantum dots (QDs) induced by electrostatic potentials. The work combined different levels of modeling — tight-binding, continuum, and effective mass approximations — to provide both accuracy and analytical insight into the low-energy behavior of carriers in black phosphorus.

The main contributions can be summarized as follows:

- We demonstrated theoretically that bilayer phosphorene quantum dots can be realized solely through a position-dependent bias potential, without requiring physical etching of the material. This approach provides a flexible and reversible method to engineer confined states, in contrast to conventional fabrication routes.
- By analyzing the confined states within the tight-binding model, we quantified how the confinement energy scales with the dot radius. In particular, we obtained a power-law dependence of the gap, $E_g(R) \propto 1/R^{1.38}$, which captures the nontrivial influence of anisotropy and layer coupling on the electronic spectrum.
- We showed that an external perpendicular magnetic field significantly modifies the spectrum and wavefunction localization of carriers, reinforcing the tunability of these nanostructures by combining geometric and external controls.

Taken together, these results demonstrate that bilayer phosphorene provides a versatile platform for quantum confinement engineered by electrostatic means. The ability to manipulate the gap and localized states using gate potentials represents a key advantage over lithographic approaches, strengthening the case for phosphorene-based quantum devices.

As a natural extension of this work, we propose to investigate quantum rings in bilayer phosphorene under the same framework. In these topologically distinct nanostructures, the interplay of bias-induced confinement and external magnetic fields is expected to give rise to Aharonov–Bohm oscillations and other interference phenomena. The power-law scaling of the gap observed in QDs suggests that similar analytical insights may be extracted for rings, potentially revealing novel size-dependent behaviors. More broadly, the methodology developed here can be adapted to other anisotropic 2D materials, opening perspectives for comparative studies and device-oriented applications.

# BIBLIOGRAPHY

[1] NOVOSELOV, K. S. et al. Electric field effect in atomically thin carbon films. *Science*, v. 306, n. 5696, p. 666–669, 2004.

[2] MAYOROV, A. S. et al. Micrometer-scale ballistic transport in encapsulated graphene at room temperature. *Nano Letters*, v. 11, n. 6, p. 2396, 2011.

[3] BALANDIN, A. A. et al. Superior thermal conductivity of single-layer graphene. *Nano Letters*, v. 8, n. 3, p. 902, 2008.

[4] BAE, S. et al. Roll-to-roll production of 30-inch graphene films for transparent electrodes. *Nature Nanotechnology*, v. 5, n. 8, p. 574, 2010.

[5] BUNCH, J. S. et al. Impermeable atomic membranes from graphene sheets. *Nano Letters*, v. 8, n. 8, p. 2458, 2008.

[6] ZARBIN, A. J. G.; OLIVEIRA, M. M. Nanoestruturas de carbono (nanotubos, grafeno): Quo vadis. *Química Nova*, v. 36, n. 10, p. 1539, 2013.

[7] WATANABE, K.; TANIGUCHI, T.; KANDA, H. Direct-bandgap properties and evidence for ultraviolet lasing of hexagonal boron nitride single crystal. *Nature Materials*, v. 3, p. 404, 2004.

[8] XU, X. et al. Spin and pseudospins in layered transition metal dichalcogenides. *Nature Physics*, v. 10, p. 343, 2014.

[9] LI, L. et al. Black phosphorus field-effect transistors. *Nature Nanotechnology*, v. 9, p. 372, 2014.

[10] VARGAS-BERNAL, R. Graphene against other two-dimensional materials: a comparative study on the basis of electronic applications. In: NAYAK, P. K. (Ed.). *Two-Dimensional Materials: Synthesis, Characterization and Potential Applications*. [S.l.]: Intech, 2016. p. 167–189.

[11] BERNARDI, M. et al. Optical and electronic properties of two-dimensional layered materials. *Nanophotonics*, v. 6, n. 2, p. 479, 2017.

[12] MANZELI, S. et al. 2d transition metal dichalcogenides. *Nature Reviews Materials*, v. 2, p. 17033, 2017.

[13] GATENSBY, R. et al. Controlled synthesis of transition metal dichalcogenide thin films for electronic applications. *Applied Surface Science*, v. 297, p. 139, 2014.

[14] XIA, F. et al. Two-dimensional material nanophotonics. *Nature Photonics*, v. 8, p. 899, 2014.

[15] ZHAO, Y. et al. Recent advance in black phosphorus: Properties and applications. *Materials Chemistry and Physics*, v. 189, p. 215, 2017.

[16] TIAN, H. et al. Optoelectronic devices based on two-dimensional transition metal dichalcogenides. *Nano Research*, v. 9, p. 1543, 2016.

[17] BRIDGMAN, P. W. Two new modifications of phosphorus. *Journal of the American Chemical Society*, v. 36, p. 1344, 1914.

[18] ISLAND, J. O. et al. Deterministic transfer of two-dimensional materials by all-dry viscoelastic stamping. *2D Materials*, v. 2, p. 011002, 2015.

[19] JAIN, A.; MCGAUGHEY, A. J. H. Strongly anisotropic in-plane thermal transport in single-layer black phosphorene. *Scientific Reports*, v. 5, p. 8501, 2015.

[20] ZHU, Z.; TOMáNEK, D. Semiconducting layered blue phosphorus: a computational study. *Physical Review Letters*, v. 112, p. 176802, 2014.

[21] GUAN, J.; ZHU, Z.; TOMáNEK, D. Phase coexistence and metal-insulator transition in few-layer phosphorene: a computational study. *Physical Review Letters*, v. 113, p. 046804, 2014.

[22] WU, R. J. et al. Atomic and electronic structure of exfoliated black phosphorus. *Journal of Vacuum Science & Technology A: Vacuum, Surfaces, and Films*, v. 33, n. 6, p. 060604, 2015.

[23] LIU, H. et al. Phosphorene: An unexplored 2d semiconductor with a high hole mobility. *ACS Nano*, v. 8, p. 4033, 2014.

[24] CASTELLANOS-GOMEZ, A. Black phosphorus: Narrow gap, wide applications. *Journal of Physical Chemistry Letters*, v. 6, p. 4280, 2015.

[25] KHANDELWAL, A. et al. Phosphorene–the two-dimensional black phosphorous: Properties, synthesis and applications. *Materials Science and Engineering: B*, v. 221, p. 17, 2017.

[26] QIAO, J. et al. High-mobility transport anisotropy and linear dichroism in few-layer black phosphorus. *Nature Communications*, v. 5, p. 4475, 2014.

[27] RUDENKO, A. N.; KATSNELSON, M. I. Quasiparticle band structure and tight-binding model for single and bilayer black phosphorus. *Physical Review B*, v. 89, p. 201408, 2014.

[28] ELLIS, J. K.; LUCERO, M. J.; SCUSERIA, G. E. The indirect to direct band gap transition in multilayered mos2 as predicted by screened hybrid density functional theory. *Applied Physics Letters*, v. 99, p. 261908, 2011.

[29] LIU, H. et al. Semiconducting black phosphorus: synthesis, transport properties and electronic applications. *Chemical Society Reviews*, v. 44, p. 2732, 2015.

[30] KOENIG, S. P. et al. Electric field effect in ultrathin black phosphorus. *Applied Physics Letters*, v. 104, p. 103106, 2014.

[31] XIA, F.; WANG, H.; JIA, Y. Rediscovering black phosphorus as an anisotropic layered material for optoelectronics and electronics. *Nature Communications*, v. 5, p. 4458, 2014.

[32] JING, Y. et al. Small molecules make big differences: molecular doping effects on electronic and optical properties of phosphorene. *Nanotechnology*, v. 26, p. 095201, 2015.

[33] TRAN, V. et al. Layer-controlled band gap and anisotropic excitons in few-layer black phosphorus. *Physical Review B*, v. 89, p. 235319, 2014.

[34] LOW, T. et al. Tunable optical properties of multilayer black phosphorus thin films. *Physical Review B*, v. 90, p. 075434, 2014.

[35] ZHANG, S. et al. Extraordinary photoluminescence and strong temperature/angle-dependent raman responses in few-layer phosphorene. *ACS Nano*, v. 8, p. 9590, 2014.

[36] FAVRON, A. et al. Photooxidation and quantum confinement effects in exfoliated black phosphorus. *Nature Materials*, v. 14, p. 826, 2015.

[37] CAI, Y.; ZHANG, G.; ZHANG, Y. W. Electronic properties of phosphorene/graphene and phosphorene/hexagonal boron nitride heterostructures. *Journal of Physical Chemistry C*, v. 119, p. 13929, 2015.

[38] DOGANOV, R. A. et al. Transport properties of pristine few-layer black phosphorus by van der waals passivation in an inert atmosphere. *Nature Communications*, v. 6, p. 6647, 2015.

[39] NOVOSELOV, K. S. et al. A roadmap for graphene. *Nature*, v. 490, p. 192, 2012.

[40] GOSWAMI, A.; GAWANDE, M. B. Phosphorene: current status, challenges and opportunities. *Frontiers of Chemical Science and Engineering*, v. 13, p. 296, 2019.

[41] NOORDEN, R. V. Production: Beyond sticky tape. *Nature*, v. 483, p. 32, 2012.

[42] NICOLOSI, V. et al. Liquid exfoliation of layered materials. *Science*, v. 340, p. 1226419, 2013.

[43] COLEMAN, J. N. et al. Two-dimensional nanosheets produced by liquid exfoliation of layered materials. *Science*, v. 331, p. 568, 2011.

[44] XU, F. et al. Scalable shear-exfoliation of high-quality phosphorene nanoflakes with reliable electrochemical cycleability in nano batteries. *2D Materials*, v. 3, p. 025005, 2016.

[45] HANLON, D.; BACKES, C. et al. Liquid exfoliation of solvent-stabilized few-layer black phosphorus for applications beyond electronics. *Nature Communications*, v. 6, p. 8563, 2015.

[46] LU, W. et al. Plasma-assisted fabrication of monolayer phosphorene and its raman characterization. *Nano Research*, v. 7, p. 853, 2014.

[47] TOUR, J. M. Top-down versus bottom-up fabrication of graphene-based electronics. *Chemistry of Materials*, v. 26, p. 163, 2013.

[48] KUMAR, V. K. et al. A predictive approach to cvd of crystalline layers of tmds: the case of mos2. *Nanoscale*, v. 7, n. 17, p. 7802, 2015.

[49] SONG, L. et al. Large scale growth and characterization of atomic hexagonal boron nitride layers. *Nano Letters*, v. 10, n. 8, p. 3209, 2010.

[50] AKINWANDE, D.; PETRONE, N.; HONE, J. Two-dimensional flexible nanoelectronics. *Nature Communications*, v. 5, p. 5678, 2014.

[51] KOPF, M. et al. Access and in situ growth of phosphorene-precursor black phosphorus. *Journal of Crystal Growth*, v. 405, p. 6, 2014.

[52] LANGE, S.; SCHMIDT, P.; NILGES, T. Sn3p7 @black phosphorus: An easy access to black phosphorus. *Inorganic Chemistry*, v. 46, p. 4028, 2007.

[53] NILGES, T.; KERSTING, M.; PFEIFER, T. A fast low-pressure transport route to large black phosphorus single crystals. *Journal of Solid State Chemistry*, v. 181, p. 1707, 2008.

[54] GAO, J.; ZHANG, G.; ZHANG, Y. W. The critical role of substrate in stabilizing phosphorene nanoflake: A theoretical exploration. *Journal of the American Chemical Society*, v. 138, p. 4763, 2016.

[55] ZHU, J.; XIAO, G.; ZUO, X. Two-dimensional black phosphorus: An emerging anode material for lithium-ion batteries. *Nano-Micro Letters*, v. 12, 2020.

[56] REZENDE, S. M. *Materiais e Dispositivos Eletrônicos*. [S.l.]: Editora Livraria da Física, 2004.

[57] ASHCROFT, N. W.; MERMIN, N. D. *Solid State Physics*. London, New York: Holt, Rinehart and Winston, 1976.

[58] MARTIN, R. M. *Electronic Structure: Basic Theory and Practical Methods*. Cambridge, UK: Cambridge University Press, 2004.

[59] DRESSELHAUS, G.; DRESSELHAUS, M. S.; SAITO, R. *Physical Properties of Carbon Nanotubes*. [S.l.]: World Scientific, 1998.

[60] BERA, D. et al. Quantum dots and their multimodal applications: a review. *Materials*, v. 3, p. 2260, 2010.

[61] DRBOHLAVOVA, J. et al. Quantum dots—characterization, preparation and usage in biological systems. *International Journal of Molecular Sciences*, v. 10, p. 656, 2019.

[62] KEBEDE, M. A.; IMAE, T. Low-dimensional nanomaterials. In: *Advanced Supramolecular Nanoarchitectonics*. [S.l.]: William Andrew Publishing, 2019. p. 3–16.

[63] ASHOORI, R. C. Electrons in artificial atoms. *Nature*, v. 379, p. 413, 1996.

[64] ALIVISATOS, A. P. Semiconductor clusters, nanocrystals, and quantum dots. *Science*, v. 271, p. 933, 1996.

[65] HEINZEL, T.; ZOZOULENKO, I. *Mesoscopic electronics in solid state nanostructures*. 3. ed. Weinheim: Wiley-VCH, 2003.

[66] BRUS, L. E. Electron–electron and electron-hole interactions in small semiconductor crystallites: The size dependence of the lowest excited electronic state. *The Journal of Chemical Physics*, v. 80, p. 4403, 1984.

[67] FERANCOVA, A.; LABUDA, J. Dna biosensors based on nanostructured materials. In: EFTEKHARI, A. (Ed.). *Nanostructured Materials in Electrochemistry*. Weinheim, Germany: Wiley-VCH, 2008. p. 409.

[68] KRAL, V. et al. Nanomedicine - current status and perspectives: A big potential or just a catchword? *Chem. Listy*, v. 100, p. 4, 2006.

[69] PONOMARENKO, L. A. et al. Chaotic dirac billiard in graphene quantum dots. *Science*, v. 320, 2008.

[70] GOPALAKRISHNAN, D.; DAMIEN, D.; SHAIJUMON, M. M. $Mos_2$ quantum dot-interspersed exfoliated $mos_2$ nanosheets. *ACS Nano*, v. 8, p. 5297, 2014.

[71] ZHANG, X. et al. Black phosphorus quantum dots. *Angewandte Chemie International Edition*, v. 54, p. 3653, 2015.

[72] WANG, X. et al. Quantum dots derived from two-dimensional materials and their applications for catalysis and energy. *Chemical Society Reviews*, v. 45, p. 2239, 2016.

[73] WANG, L. et al. Gram-scale synthesis of single-crystalline graphene quantum dots with superior optical properties. *Nature Communications*, v. 5, p. 5357, 2014.

[74] GE, J. et al. A graphene quantum dot photodynamic therapy agent with high singlet oxygen generation. *Nature Communications*, v. 5, p. 4596, 2014.

[75] KONSTANTATOS, G. et al. Hybrid graphene-quantum dot phototransistors with ultrahigh gain. *Nature Nanotechnology*, v. 7, p. 363, 2012.

[76] SOFER, Z. et al. Few-layer black phosphorus nanoparticles. *Chemistry Communicattions*, v. 52, p. 1563, 2016.

[77] ZHU, C. et al. Ultrafast preparation of black phosphorus quantum dots for efficient humidity sensing. *Chemistry A European Journal*, v. 22, p. 7357, 2016.

[78] SUN, Z. et al. Ultrasmall black phosphorus quantum dots: synthesis and use as photothermal agents. *Angewandte chemie international edition*, v. 54, p. 11526, 2015.

[79] XU, Y. et al. Advanced optical matererials. *Advanced Optical Matererials*, v. 4, p. 1223, 2016.

[80] ANJU, S. et al. Black phosphorous quantum dots. In: *Black Phosphorus*. Cham: Springer, 2020. p. 73–100.

[81] NIU, X. et al. Anomalous size dependence of optical properties in black phosphorus quantum dots. *The Journal of Physical Chemistry Letters*, v. 7, p. 370, 2016.

[82] ABDELSALAM, H. et al. Multilayer phosphorene quantum dots in an electric field: Energy levels and optical absorption. *Journal of applied physics*, v. 124, p. 124303, 2018.

[83] AHARONOV, Y.; BOHM, D. Significance of electromagnetic potentials in the quantum theory. *Physical Review*, v. 115, p. 485, 1959.

[84] AHARONOV, Y.; CASHER, A. Topological quantum effects for neutral particles. *Physical Review Letters*, v. 53, p. 319, 1984.

[85] FUHRER, A. et al. Energy spectra of quantum rings. *Nature London*, v. 413, p. 822, 2001.

[86] BAYER, M. et al. Hidden symmetries in the energy levels of excitonic artificial atoms. *Nature*, v. 405, p. 923, 2000.

[87] BAYER, M. et al. Optical detection of the aharonov-bohm effect on a charged particle in a nanoscale quantum ring. *Physical Review Letters*, v. 90, p. 186801, 2003.

[88] KURODA, T. et al. Excitonic transitions in semiconductor concentric quantum double rings. *Physica E*, v. 32, p. 46, 2006.

[89] RUSSO, S. et al. Observation of aharonov-bohm conductance oscillations in a graphene ring. *Physical Review B*, v. 77, p. 085413, 2008.

[90] COSTA, D. R. da et al. Geometry and edge effects on the energy levels of graphene quantum rings: A comparison between tight-binding and simplified dirac models. *Physical Review B*, v. 89, p. 075418, 2014.

[91] ZHANG, R. et al. Aharonov-bohm effect in monolayer phosphorene nanorings. *Physical Review B*, v. 95, p. 125418, 2017.

[92] RUDENKO, A. N.; YUAN, S.; KATSNELSON, M. I. Toward a realistic description of multilayer black phosphorus: From gw approximation to large-scale tight-binding simulations. *Physical Review B*, v. 92, p. 085419, 2015.

[93] SOUSA, D. J. P. de et al. Multilayered black phosphorus: From a tight-binding to a continuum description. *Physical Review B*, v. 96, p. 155427, 2017.

[94] SHI, H.; MOU, Y.; RUI-QIANG, W. Double band-inversions of bilayer phosphorene under strain and their effects on optical absorption. *Chinese Physics B*, v. 27, p. 047303, 2018.

[95] JR., J. M. P.; KATSNELSON, M. I. Landau levels of single-layer and bilayer phosphorene. *Physical Review B*, v. 92, p. 075437, 2015.

[96] IHN, T. *Semiconductor Nanostructures: Quantum states and electronic transport*. [S.l.]: OUP Oxford, 2009.

[97] HARRISON, P.; VALAVANIS, A. *Quantum wells, wires and dots: theoretical and computational physics of semiconductor nanostructures*. [S.l.]: John Wiley & Sons, 2016.

[98] CHAKRABORTY, T. *Quantum Dots: A survey of the properties of artificial atoms*. [S.l.]: Elsevier, 1999.

[99] JACAK, L.; HAWRYLAK, P.; WOJS, A. *Quantum dots*. [S.l.]: Springer Science & Business Media, 2013.

[100] REIMANN, S. M.; MANNINEN, M. Electronic structure of quantum dots. *Reviews of Modern Physics*, APS, v. 74, n. 4, p. 1283, 2002.

[101] ENSSLIN, K. Quantum physics in quantum dots. In: *Les Houches*. [S.l.]: Elsevier, 2005. v. 81, p. 585–586.

[102] ZARENIA, M. et al. Electrostatically confined quantum rings in bilayer graphene. *Nano Letters*, v. 9, n. 12, p. 4088, 2009.

[103] JR., J. M. P.; VASILOPOULOS, P.; PEETERS, F. M. Tunable quantum dots in bilayer graphene. *Nano Letters*, v. 7, n. 4, p. 946, 2007.

[104] LEE, J. et al. Imaging electrostatically confined dirac fermions in graphene quantum dots. *Nature Physics*, Nature Publishing Group, v. 12, n. 11, p. 1032–1036, 2016.

[105] JR, J. V. et al. Visualization and control of single-electron charging in bilayer graphene quantum dots. *Nano letters*, ACS Publications, v. 18, n. 8, p. 5104–5110, 2018.

[106] GUTIÉRREZ, C. et al. Klein tunnelling and electron trapping in nanometre-scale graphene quantum dots. *Nature Physics*, Nature Publishing Group, v. 12, n. 11, p. 1069–1075, 2016.

[107] MIRZAKHANI, M. et al. Energy levels of hybrid monolayer-bilayer graphene quantum dots. *Physical Review B*, APS, v. 93, n. 16, p. 165410, 2016.

[108] COSTA, D. R. da et al. Energy levels of bilayer graphene quantum dots. *Physical Review B*, APS, v. 92, n. 11, p. 115437, 2015.

[109] COSTA, D. R. da et al. Magnetic field dependence of energy levels in biased bilayer graphene quantum dots. *Physical Review B*, APS, v. 93, n. 8, p. 085401, 2016.

[110] COSTA, D. R. da et al. Hexagonal-shaped monolayer-bilayer quantum disks in graphene: A tight-binding approach. *Physical Review B*, APS, v. 94, n. 3, p. 035415, 2016.

[111] NASCIMENTO, J. S. et al. Magnetic properties of bilayer graphene quantum dots in the presence of uniaxial strain. *Physical Review B*, APS, v. 96, n. 11, p. 115428, 2017.

[112] LAVOR, I. R. et al. Magnetic field induced vortices in graphene quantum dots. *Journal of Physics: Condensed Matter*, IOP Publishing, v. 32, n. 15, p. 155501, 2020.

[113] ARAÚJO, F. R. V. et al. Modulation of persistent current in graphene quantum rings. *Journal of Physics: Condensed Matter*, IOP Publishing, v. 34, n. 12, p. 125503, 2022.

[114] MIRZAKHANI, M.; COSTA, D. R. da; PEETERS, F. M. Isolated and hybrid bilayer graphene quantum rings. *Physical Review B*, APS, v. 105, n. 11, p. 115430, 2022.

[115] MIRZAKHANI, M. et al. Energy levels of abc-stacked trilayer graphene quantum dots with infinite-mass boundary conditions. *Physical Review B*, APS, v. 94, n. 16, p. 165423, 2016.

[116] GUPTA, A.; SAKTHIVEL, T.; SEAL, S. Recent development in 2d materials beyond graphene. *Progress in Materials Science*, Elsevier, v. 73, p. 44–126, 2015.

[117] MAS-BALLESTE, R. et al. 2d materials: to graphene and beyond. *Nanoscale*, Royal Society of Chemistry, v. 3, n. 1, p. 20–30, 2011.

[118] MANNIX, A. J. et al. Synthesis and chemistry of elemental 2d materials. *Nature Reviews Chemistry*, Nature Publishing Group, v. 1, n. 2, p. 1–14, 2017.

[119] CHAVES, A. et al. Bandgap engineering of two-dimensional semiconductor materials. *npj 2D Materials and Applications*, Nature Publishing Group, v. 4, n. 1, p. 1–21, 2020.

[120] MORITA, A. Semiconducting black phosphorus. *Applied Physics A*, v. 39, p. 227, 1986.

[121] HE, J. et al. Exceptional and anisotropic transport properties of photocarriers in black phosphorus. *ACS nano*, ACS Publications, v. 9, n. 6, p. 6436–6442, 2015.

[122] LONG, G. et al. Achieving ultrahigh carrier mobility in two-dimensional hole gas of black phosphorus. *Nano Letters*, ACS Publications, v. 16, n. 12, p. 7768–7773, 2016.

[123] LING, X. et al. The renaissance of black phosphorus. *Proceedings of the National Academy of Sciences*, National Acad Sciences, v. 112, n. 15, p. 4523–4530, 2015.

[124] GUI, R. et al. Black phosphorus quantum dots: synthesis, properties, functionalized modification and applications. *Chemical Society Reviews*, v. 47, p. 6795, 2018.

[125] KOU, L.; CHEN, C.; SMITH, S. C. Phosphorene: fabrication, properties, and applications. *The Journal of Physical Chemistry Letters*, ACS Publications, v. 6, n. 14, p. 2794–2805, 2015.

[126] UMRAO, S. et al. Synthesis and characterization of phosphorene: A novel 2d material. *Nanomaterials: Biomedical, Environmental, and Engineering Applications*, John Wiley & Sons, Inc. Hoboken, NJ, USA, p. 61–92, 2018.

[127] CHEN, P. et al. The rising star of 2d black phosphorus beyond graphene: synthesis, properties and electronic applications. *2D Materials*, IOP Publishing, v. 5, n. 1, p. 014002, 2017.

[128] CASTELLANOS-GOMEZ, A. et al. Isolation and characterization of few-layer black phosphorus. *2D Materials*, IOP Publishing, v. 1, n. 2, p. 025001, 2014.

[129] DAS, S. et al. Tunable transport gap in phosphorene. *Nano Letters*, v. 14, p. 5733, 2014.

[130] RODIN, A. S.; CARVALHO, A.; NETO, A. H. C. Strain-induced gap modification in black phosphorus. *Physical review letters*, APS, v. 112, n. 17, p. 176801, 2014.

[131] ZHANG, G. et al. Infrared fingerprints of few-layer black phosphorus. *Nature Communications*, Nature Publishing Group UK London, v. 8, n. 1, p. 14071, 2017.

[132] KIM, J. et al. Observation of tunable band gap and anisotropic dirac semimetal state in black phosphorus. *Science*, American Association for the Advancement of Science, v. 349, n. 6249, p. 723–726, 2015.

[133] KIM, J. et al. Two-dimensional dirac fermions protected by space-time inversion symmetry in black phosphorus. *Physical Review Letters*, APS, v. 119, n. 22, p. 226801, 2017.

[134] DOLUI, K.; QUEK, S. Y. Quantum-confinement and structural anisotropy result in electrically-tunable dirac cone in few-layer black phosphorous. *Scientific Reports*, Nature Publishing Group UK London, v. 5, n. 1, p. 11699, 2015.

[135] YUAN, S. et al. Quantum hall effect and semiconductor-to-semimetal transition in biased black phosphorus. *Physical Review B*, APS, v. 93, n. 24, p. 245433, 2016.

[136] BAIK, S. S. et al. Emergence of two-dimensional massless dirac fermions, chiral pseudospins, and berry’s phase in potassium doped few-layer black phosphorus. *Nano letters*, ACS Publications, v. 15, n. 12, p. 7788–7793, 2015.

[137] LIU, Q. et al. Switching a normal insulator into a topological insulator via electric field with application to phosphorene. *Nano letters*, ACS Publications, v. 15, n. 2, p. 1222–1228, 2015.

[138] ZHANG, Y. et al. Direct observation of a widely tunable bandgap in bilayer graphene. *Nature*, Nature Publishing Group UK London, v. 459, n. 7248, p. 820–823, 2009.

[139] OHTA, T. et al. Controlling the electronic structure of bilayer graphene. *Science*, American Association for the Advancement of Science, v. 313, n. 5789, p. 951–954, 2006.

[140] QIAO, J. et al. Gram-scale preparation of black phosphorus nanosheets via shock-induced phase transformation. *Journal of Materials Chemistry C*, Royal Society of Chemistry, v. 10, n. 27, p. 10017–10026, 2022.

[141] QIAO, J. et al. Formation of black phosphorus quantum dots via shock-induced phase transformation. *Applied Physics Letters*, AIP Publishing LLC, v. 120, n. 14, p. 141902, 2022.

[142] TANG, X. et al. Fluorination-enhanced ambient stability and electronic tolerance of black phosphorus quantum dots. *Advanced Science*, v. 5, n. 9, p. 1800420, 2018.

[143] ZHANG, R. et al. Electronic and magneto-optical properties of monolayer phosphorene quantum dots. *2D Materials*, v. 2, p. 045012, 2015.

[144] LINO, M. A. et al. Charging energy spectrum of black phosphorus quantum dots. *Journal of Applied Physics*, v. 50, p. 305103, 2017.

[145] SOUSA, J. S. de et al. Substrate effects on the exciton fine structure of black phosphorus quantum dots. *Physical Review B*, v. 96, p. 035122, 2017.

[146] MELO, H. A. et al. Conditions for the occurrence of coulomb blockade in phosphorene quantum dots at room temperature. *Physical Review B*, APS, v. 98, n. 11, p. 115438, 2018.

[147] SAROKA, V. A. et al. Electro-optical properties of phosphorene quantum dots. *Physical Review B*, v. 96, p. 085436, 2017.

[148] LI, L. L. et al. Electric and magnetic-field dependence of the electronic and optical properties of phosphorene quantum dots. *Nanotechnology*, v. 28, p. 085702, 2017.

[149] LEI, W. et al. Recent progress on black phosphorus quantum dots for full-spectrum solar-to-chemical energy conversion. *Nano Today*, Elsevier, v. 39, p. 101183, 2021.

[150] LIU, X. et al. 2d phosphorene nanosheets, quantum dots, nanoribbons: Synthesis and biomedical applications. *Biomaterials Science*, Royal Society of Chemistry, v. 9, n. 8, p. 2768–2803, 2021.

[151] SZAFRAN, B. Electrostatic quantum dot confinement in phosphorene. *Physical Review B*, APS, v. 101, n. 23, p. 235313, 2020.

[152] ABDELSALAM, H.; SAROKA, V. A.; YOUNIS, W. O. Phosphorene quantum dot electronic properties and gas sensing. *Physica E: Low-dimensional Systems and Nanostructures*, Elsevier, v. 107, p. 105–109, 2019.

[153] JIANG, Z. T.; LIANG, F. X.; ZHANG, X. D. A comparative study on the edge states in phosphorene quantum dots and rings. *Physics Letters A*, v. 381, p. 373, 2017.

[154] LI, L. L. et al. Aharonov-bohm oscillations in phosphorene quantum rings. *Physical Review B*, v. 95, p. 205426, 2017.

[155] THAKUR, T.; SZAFRAN, B. Aharonov-bohm oscillations in phosphorene quantum rings: Mass anisotropy compensation by confinement potential. *Physical Review B*, APS, v. 105, n. 16, p. 165309, 2022.

[156] SOUSA, G. O. de et al. Unusual quantum confined stark effect and aharonov-bohm oscillations in semiconductor quantum rings with anisotropic effective masses. *Physical Review B*, v. 95, p. 205414, 2017.

[157] LI, L. L. et al. Electronic properties of bilayer phosphorene quantum dots in the presence of perpendicular electric and magnetic fields. *Physical Review B*, v. 96, p. 155425, 2017.

[158] ZARE, M.; HAGHDOUST, S. Magneto-optical properties of bilayer phosphorene quantum dots. *Physical Chemistry Chemical Physics*, Royal Society of Chemistry, v. 23, n. 32, p. 17645–17655, 2021.

[159] JIANG, Z. T. et al. Energy spectrums of bilayer triangular phosphorene quantum dots and antidots. *AIP Advances*, AIP Publishing LLC, v. 7, n. 4, p. 045122, 2017.

[160] WANG, Z.; LI, X.; WU, Z. Electronic and optical properties of the edge states in phosphorene quantum rings. *Applied Surface Science*, Elsevier, v. 541, p. 148317, 2021.

[161] ZHANG, R. et al. Fano resonances in bilayer phosphorene nanoring. *Nanotechnology*, IOP Publishing, v. 29, n. 21, p. 215202, 2018.

[162] LIANG, F. et al. Electronic properties and optical absorption of multi-layer phosphorene quantum rings. *AIP Advances*, AIP Publishing LLC, v. 12, n. 4, p. 045303, 2022.

[163] ÇAKIR, D.; SEVIK, C.; PEETERS, F. M. Significant effect of stacking on the electronic and optical properties of few-layer black phosphorus. *Physical Review B*, APS, v. 92, n. 16, p. 165406, 2015.

[164] GE, Z. et al. Visualization and manipulation of bilayer graphene quantum dots with broken rotational symmetry and nontrivial topology. *Nano letters*, ACS Publications, v. 20, n. 12, p. 8682–8688, 2020.

[165] DENG, N. et al. Black phosphorus junctions and their electrical and optoelectronic applications. *Journal of Semiconductors*, IOP Publishing, v. 42, n. 8, p. 081001, 2021.

[166] PEIERLS, R. Zur theorie des diamagnetismus von leitungselektronen. *Zeitschrift für Physik*, Springer, v. 80, n. 11-12, p. 763–791, 1933.

[167] LUTTINGER, J. M. The effect of a magnetic field on electrons in a periodic potential. *Physical Review*, APS, v. 84, n. 4, p. 814, 1951.

[168] COSTA, D. R. da et al. Analytical study of the energy levels in bilayer graphene quantum dots. *Carbon*, Elsevier, v. 78, p. 392–400, 2014.

[169] ZARENIA, M. et al. Simplified model for the energy levels of quantum rings in single layer and bilayer graphene. *Physical Review B*, v. 81, p. 045431, 2010.

[170] RUDENKO, A. N.; KATSNELSON, M. I. Anisotropic effects in two-dimensional materials. *2D Materials*, IOP Publishing, v. 11, n. 4, p. 042002, 2024.

# APPENDIX A - ANALYTICAL EXPRESSION FOR THE ENERGY GAP OF THE BIAS BL BP

The analytical expressions for the conduction ($E_c$) and valence ($E_v$) energy states, shown in Fig. 22(b) and in green dashed curves in Fig. 25(a), are obtained by diagonalizing the biased BL BP tight-binding Hamiltonian, as derived in Refs. [95, 93], given by

$$E_c = t_{AA} + t_{AD} + t_{AB} + t_{AC} - \sqrt{\left(\frac{t_{AC'}}{2}\right)^2 + \left(\frac{U}{2}\right)^2}, \tag{A.1a}$$

$$E_v = t_{AA} + t_{AD} - t_{AB} - t_{AC} + \sqrt{\left(\frac{t_{AC'}}{2}\right)^2 + \left(\frac{U}{2}\right)^2}, \tag{A.1b}$$

in which the $t_{\beta\beta'}$ terms (with $\beta_i, \beta_i' \equiv \{A_i, B_i, C_i, D_i\}$) are associated with all contributions involving the coupling energies between equivalent sites $\beta_i$ and $\beta'$; for instance, $t_{AB}$ accounts for all energetic connections between $A-B$ and $C-D$ sites, whereas $t_{AA}$ accounts for intralayer energetic connections between next neighbors $A-A$, $B-B$, $C-C$ and $D-D$ sites (see Refs. [95, 93] for more details). At the $\vec{\Gamma}$–point, $t_{\beta\beta'}$ are given in terms of the hopping energies (Table 4) by

$$t_{AA}(\Gamma) = 2\left(t_3 + t_7 + 2t_{10}\right), \tag{A.2a}$$

$$t_{AB}(\Gamma) = 2\left(t_1 + t_4 + t_8\right), \tag{A.2b}$$

$$t_{AC}(\Gamma) = t_2 + t_6 + 2t_9, \tag{A.2c}$$

$$t_{AD}(\Gamma) = 4t_5, \tag{A.2d}$$

$$t_{AC'}(\Gamma) = 2\left(t_1^{\perp} + t_4^{\perp}\right). \tag{A.2e}$$

Thus, the absolute value of the energy gap for the biased BL BP system is then given by

$$\begin{aligned} E_g^{\text{bl}}(\Gamma, U) &= |E_c - E_v| \\ &= 2\left| t_{AB}(\Gamma) + t_{AC}(\Gamma) - \sqrt{\left(\frac{t_{AC'}}{2}\right)^2 + \left(\frac{U}{2}\right)^2} \right| \\ &= \left| E_g^{\text{mono}}(\Gamma) - \sqrt{\left(\frac{t_{AC'}}{2}\right)^2 + \left(\frac{U}{2}\right)^2} \right|, \end{aligned} \tag{A.3}$$

being written in terms of the monolayer BP energy gap, $E_g^{\text{mono}}(\Gamma) = 2\,|t_{AB}(\Gamma) + t_{AC}(\Gamma)|$. [93] For the unbiased case, one gets

$$\begin{aligned} E_g^{\text{bl}}(\Gamma, 0) &= 2\,|t_{AB}(\Gamma) + t_{AC}(\Gamma) - t_{AC'}(\Gamma)/2| \\ &= \left|E_g^{\text{mono}}(\Gamma) - t_{AC'}(\Gamma)/2\right|. \end{aligned} \tag{A.4}$$

According to Ref. [93], $E_g^{\text{bl}}(\Gamma, 0)$ at zero bias is $\approx 1.126$ eV ($\approx 1.6$ eV) within the ten-hopping intralayer and five-hopping interlayer tight-binding (continuum) model (see Table 4). This corresponds approximately to the region delimited by the two dashed red lines in Fig. 25(a) and approximately the first data point in Fig. 25(b) of the fit curve (black curve) for the continuum model case, and green and orange curves for the tight-binding model case.